

1

<sup>2</sup>A SEARCH FOR LONG-LIVED, CHARGED, SUPERSYMMETRIC PARTICLES  
<sup>3</sup>USING IONIZATION WITH THE ATLAS DETECTOR

4

BRADLEY AXEN

5

September 2016 – Version 0.36

6



<sup>8</sup> Bradley Axen: *A Search for Long-Lived, Charged, Supersymmetric Particles using*  
<sup>9</sup> *Ionization with the ATLAS Detector*, Subtitle, © September 2016

10

Usually a quotation.

11

Dedicated to.



<sub>12</sub> ABSTRACT

---

<sub>13</sub> How to write a good abstract:

<sub>14</sub> <https://plg.uwaterloo.ca/~migod/research/beck00PSLA.html>



<sub>15</sub> PUBLICATIONS

---

<sub>16</sub> Some ideas and figures have appeared previously in the following publications:

<sub>17</sub>

<sub>18</sub> Put your publications from the thesis here. The packages `multibib` or `bibtopic`  
<sub>19</sub> etc. can be used to handle multiple different bibliographies in your document.



---

<sup>21</sup> ACKNOWLEDGEMENTS

<sup>22</sup> Put your acknowledgements here.

<sup>23</sup>

<sup>24</sup> And potentially a second round.

<sup>25</sup>



26 CONTENTS

---

27	I	INTRODUCTION	1
28	1	INTRODUCTION	3
29	II	THEORETICAL CONTEXT	5
30	2	STANDARD MODEL	7
31	2.1	Particles . . . . .	7
32	2.2	Interactions . . . . .	8
33	2.3	Limitations . . . . .	8
34	3	SUPERSYMMETRY	9
35	3.1	Motivation . . . . .	9
36	3.2	Structure . . . . .	9
37	3.3	Phenomenology . . . . .	9
38	4	LONG-LIVED PARTICLES	11
39	4.1	Mechanisms . . . . .	11
40	4.1.1	Examples in Supersymmetry . . . . .	11
41	4.2	Phenomenology . . . . .	11
42	4.2.1	Disimilarities to Prompt Decays . . . . .	11
43	4.2.2	Characteristic Signatures . . . . .	11
44	III	EXPERIMENTAL STRUCTURE AND RECONSTRUCTION	13
45	5	THE LARGE HADRON COLLIDER	15
46	5.1	Injection Chain . . . . .	15
47	5.2	Design and Parameters . . . . .	15
48	5.3	Luminosity . . . . .	15
49	6	THE ATLAS DETECTOR	17
50	6.1	Coordinate System . . . . .	17
51	6.2	Magnetic Field . . . . .	17
52	6.3	Inner Detector . . . . .	17
53	6.3.1	Pixel Detector . . . . .	17
54	6.3.2	Semiconductor Tracker . . . . .	17
55	6.3.3	Transition Radiation Tracker . . . . .	17
56	6.4	Calorimetry . . . . .	17
57	6.4.1	Electromagnetic Calorimeters . . . . .	17
58	6.4.2	Hadronic Calorimeters . . . . .	17
59	6.4.3	Forward Calorimeters . . . . .	17
60	6.5	Muon Spectrometer . . . . .	17
61	6.6	Trigger . . . . .	17
62	6.6.1	Trigger Scheme . . . . .	17
63	6.6.2	Missing Transverse Energy Triggers . . . . .	17
64	7	EVENT RECONSTRUCTION	19
65	7.1	Tracks and Vertices . . . . .	19

66	7.1.1	Track Reconstruction . . . . .	19
67	7.1.2	Vertex Reconstruction . . . . .	19
68	7.2	Jets . . . . .	19
69	7.2.1	Topological Clustering . . . . .	19
70	7.2.2	Jet Energy Scale . . . . .	19
71	7.2.3	Jet Energy Scale Uncertainties . . . . .	19
72	7.2.4	Jet Energy Resolution . . . . .	19
73	7.3	Electrons . . . . .	19
74	7.3.1	Electron Identification . . . . .	19
75	7.4	Muons . . . . .	19
76	7.4.1	Muon Identification . . . . .	19
77	7.5	Missing Transverse Energy . . . . .	19
78	<b>IV</b>	<b>CALORIMETER RESPONSE</b>	21
79	8	RESPONSE MEASUREMENT WITH SINGLE HADRONS	23
80	8.1	Dataset and Simulation . . . . .	24
81	8.1.1	Data Samples . . . . .	24
82	8.1.2	Simulated Samples . . . . .	24
83	8.1.3	Event Selection . . . . .	24
84	8.2	Inclusive Hadron Response . . . . .	25
85	8.2.1	E/p Distribution . . . . .	25
86	8.2.2	Zero Fraction . . . . .	26
87	8.2.3	Neutral Background Subtraction . . . . .	27
88	8.2.4	Corrected Response . . . . .	29
89	8.2.5	Additional Studies . . . . .	31
90	8.3	Identified Particle Response . . . . .	34
91	8.3.1	Decay Reconstruction . . . . .	34
92	8.3.2	Identified Response . . . . .	35
93	8.3.3	Additional Species in Simulation . . . . .	37
94	8.4	Summary . . . . .	38
95	9	JET ENERGY RESPONSE AND UNCERTAINTY	41
96	9.1	Motivation . . . . .	41
97	9.2	Uncertainty Estimate . . . . .	41
98	9.3	Summary . . . . .	44
99	<b>V</b>	<b>SEARCH FOR LONG-LIVED PARTICLES</b>	47
100	10	LONG-LIVED PARTICLES IN ATLAS	49
101	10.1	Event Topology . . . . .	49
102	10.1.1	Detector Interactions . . . . .	50
103	10.1.2	Lifetime Dependence . . . . .	51
104	10.2	Simulation . . . . .	54
105	11	EVENT SELECTION	57
106	11.1	Trigger . . . . .	58
107	11.2	Kinematics and Isolation . . . . .	59
108	11.3	Particle Species Rejection . . . . .	63
109	11.4	Ionization . . . . .	66
110	11.4.1	Mass Estimation . . . . .	67

111	11.5 Efficiency . . . . .	68
112	12 BACKGROUND ESTIMATION	71
113	12.1 Background Sources . . . . .	71
114	12.2 Prediction Method . . . . .	72
115	12.3 Validation . . . . .	73
116	12.3.1 Closure in Simulation . . . . .	73
117	12.3.2 Validation Region in Data . . . . .	74
118	13 SYSTEMATIC UNCERTAINTIES AND RESULTS	77
119	13.1 Systematic Uncertainties . . . . .	77
120	13.1.1 Background Estimate . . . . .	77
121	13.1.2 Signal Yield . . . . .	78
122	13.2 Final Yields . . . . .	83
123	13.3 Cross Sectional Limits . . . . .	83
124	13.4 Mass Limits . . . . .	83
125	13.5 Context for Long-Lived Searches . . . . .	83
126	<b>VI CONCLUSIONS</b>	85
127	14 SUMMARY AND OUTLOOK	87
128	14.1 Summary . . . . .	87
129	14.2 Outlook . . . . .	87
130	<b>VII APPENDIX</b>	89
131	A INELASTIC CROSS SECTION	91
132	B APPENDIX TEST	93
133	B.1 Appendix Section Test . . . . .	93
134	B.1.1 Appendix Subection Test . . . . .	93
135	B.2 A Table and Listing . . . . .	93
136	B.3 Some Formulas . . . . .	94
137	BIBLIOGRAPHY	97

138 LIST OF FIGURES

---

139	Figure 1	The particle content of the Standard Model (SM). . . . .	8
140	Figure 2	An illustration (a) of the $E/p$ variable used throughout this paper. The red energy deposits come from the charged particle targeted for measurement, while the blue energy deposits are from nearby neutral particles and must be subtracted. The same diagram (b) for the neutral-background selection, described in Section 8.2.3.	26
141			
142			
143			
144			
145			
146	Figure 3	The $E/p$ distribution and ratio of simulation to data for isolated tracks with (a) $ \eta  < 0.6$ and $1.2 < p/\text{GeV} < 1.8$ and (b) $ \eta  < 0.6$ and $2.2 < p/\text{GeV} < 2.8$ . . . . .	26
147			
148			
149	Figure 4	The fraction of tracks as a function (a, b) of momentum, (c, d) of interaction lengths with $E \leq 0$ for tracks with positive (on the left) and negative (on the right) charge. . . . .	28
150			
151			
152			
153	Figure 5	$\langle E/p \rangle_{\text{BG}}$ as a function of the track momentum for tracks with (a) $ \eta  < 0.6$ , (b) $0.6 <  \eta  < 1.1$ , and as a function of the track pseudorapidity for tracks with (c) $1.2 < p/\text{GeV} < 1.8$ , (d) $1.8 < p/\text{GeV} < 2.2$ . . . . .	29
154			
155			
156			
157	Figure 6	$\langle E/p \rangle_{\text{COR}}$ as a function of track momentum, for tracks with (a) $ \eta  < 0.6$ , (b) $0.6 <  \eta  < 1.1$ , (c) $1.8 <  \eta  < 1.9$ , and (d) $1.9 <  \eta  < 2.3$ . . . . .	30
158			
159			
160	Figure 7	$\langle E/p \rangle_{\text{COR}}$ calculated using LCW-calibrated topological clusters as a function of track momentum for tracks with (a) zero or more associated topological clusters or (b) one or more associated topological clusters. . . . .	31
161			
162			
163			
164	Figure 8	Comparison of the $\langle E/p \rangle_{\text{COR}}$ for tracks with (a) less than and (b) greater than 20 hits in the TRT. . . . .	32
165			
166	Figure 9	Comparison of the $\langle E/p \rangle_{\text{COR}}$ for (a) positive and (b) negative tracks as a function of track momentum for tracks with $ \eta  < 0.6$ . . . . .	32
167			
168			
169	Figure 10	Comparison of the $E/p$ distributions for (a) positive and (b) negative tracks with $0.8 < p/\text{GeV} < 1.2$ and $ \eta  < 0.6$ , in simulation with the FTFP_BERT and QGSP_BERT physics lists. . . . .	33
170			
171			
172			
173	Figure 11	Comparison of the response of the hadronic calorimeter as a function of track momentum (a) at the EM-scale and (b) after the LCW calibration. . . . .	33
174			
175			
176	Figure 12	Comparison of the response of the EM calorimeter as a function of track momentum (a) at the EM-scale and (b) with the LCW calibration. . . . .	34
177			
178			

179	Figure 13	The reconstructed mass peaks of (a) $K_S^0$ , (b) $\Lambda$ , and (c) $\bar{\Lambda}$ candidates. . . . .	35
180			
181	Figure 14	The $E/p$ distribution for isolated (a) $\pi^+$ , (b) $\pi^-$ , (c) proton, and (d) anti-proton tracks. . . . .	36
182			
183	Figure 15	The fraction of tracks with $E \leq 0$ for identified (a) $\pi^+$ and $\pi^-$ , and (b) proton and anti-proton tracks . . . . .	36
184			
185	Figure 16	The difference in $\langle E/p \rangle$ between (a) $\pi^+$ and $\pi^-$ (b) $p$ and $\pi^+$ , and (c) $\bar{p}$ and $\pi^-$ . . . . .	37
186			
187	Figure 17	$\langle E/p \rangle_{\text{COR}}$ as a function of track momentum for (a) $\pi^+$ tracks and (b) $\pi^-$ tracks. . . . .	38
188			
189	Figure 18	The ratio of the calorimeter response to single parti- cles of various species to the calorimeter response to $\pi^+$ with the physics list FTFP_BERT. . . . .	38
190			
191	Figure 19	The spectra of true particles inside anti- $k_t$ , $R = 0.4$ jets with (a) $90 < p_T/\text{GeV} < 100$ , (b) $400 < p_T/\text{GeV} <$ $500$ , and (c) $1800 < p_T/\text{GeV} < 2300$ . . . . .	42
192			
193	Figure 20	The jet energy scale ( <a>JES</a> ) uncertainty contributions, as well as the total <a>JES</a> uncertainty, as a function of jet $p_T$ for (a) $ \eta  < 0.6$ and (b) $0.6 <  \eta  < 1.1$ . . . . .	44
194			
195	Figure 21	The <a>JES</a> correlations as a function of jet $p_T$ and $ \eta $ for jets in the central region of the detector. . . . .	45
196			
197	Figure 22	A schematic diagram of an R-Hadron event with a life- time around 0.01 ns. The diagram includes one charged R-Hadron (solid blue), one neutral R-Hadron (dashed blue), Lightest Supersymmetric Particles ( <a>LSPs</a> ) (dashed green) and charged hadrons (solid orange). The pixel detector, calorimeters, and muon system are illustrated but not to scale. . . . .	51
198			
199	Figure 23	A schematic diagram of an R-Hadron event with a life- time around 4 ns. The diagram includes one charged R-Hadron (solid blue), one neutral R-Hadron (dashed blue), <a>LSPs</a> (dashed green) and a charged hadron (solid orange). The pixel detector, calorimeters, and muon system are illustrated but not to scale. . . . .	52
200			
201	Figure 24	A schematic diagram of an R-Hadron event with a life- time around 5 ns. The diagram includes one charged R-Hadron (solid blue), one neutral R-Hadron (dashed blue), <a>LSPs</a> (dashed green) and charged hadrons (solid orange). The pixel detector, calorimeters, and muon system are illustrated but not to scale. . . . .	53
202			
203	Figure 25	A schematic diagram of an R-Hadron event with a life- time around 20 ns. The diagram includes one charged R-Hadron (solid blue), one neutral R-Hadron (dashed blue), <a>LSPs</a> (dashed green) and charged hadrons (solid orange). The pixel detector, calorimeters, and muon system are illustrated but not to scale. . . . .	53
204			
205			
206			
207			
208			
209			
210			
211			
212			
213			
214			
215			
216			
217			
218			
219			
220			
221			
222			
223			
224			

225	Figure 26	A schematic diagram of an R-Hadron event with a life-time around 20 ns. The diagram includes one charged R-Hadron (solid blue) and one neutral R-Hadron (dashed blue). The pixel detector, calorimeters, and muon system are illustrated but not to scale. . . . .	54
226			
227			
228			
229			
230	Figure 27	The distribution of (a) $E_T^{\text{miss}}$ and (b) Calorimeter $E_T^{\text{miss}}$ for simulated signal events before the trigger requirement. . . . .	58
231			
232			
233	Figure 28	The distribution of $E_T^{\text{miss}}$ for data and simulated signal events, after the trigger requirement. . . . .	60
234			
235	Figure 29	The trigger efficiency for the HLT_xe70 trigger requirement as a function of (a) $E_T^{\text{miss}}$ and (b) Calorimeter $E_T^{\text{miss}}$ for simulated signal events. . . . .	61
236			
237			
238	Figure 30	The dependence of $dE/dx$ on $N_{\text{split}}$ in data after basic track hit requirements have been applied. . . . .	62
239			
240	Figure 31	The distribution of $dE/dx$ with various selections applied in data and simulated signal events. . . . .	62
241			
242	Figure 32	The distribution of track momentum for data and simulated signal events, after previous selection requirements have been applied. . . . .	63
243			
244			
245	Figure 33	The distribution of $M_T$ for data and simulated signal events, after previous selection requirements have been applied. . . . .	64
246			
247			
248	Figure 34	The distribution of summed tracked momentum within a cone of $\Delta R < 0.25$ around the candidate track for data and simulated signal events, after previous selection requirements have been applied. . . . .	65
249			
250			
251			
252	Figure 35	The normalized, two-dimensional distribution of $E/p$ and $f_{\text{EM}}$ for simulated (a) $Z \rightarrow ee$ , (b) $Z \rightarrow \tau\tau$ , (c) 1200 GeV Stable R-Hadron events, and (d) 1200 GeV, 10 ns R-Hadron events. . . . .	66
253			
254			
255			
256	Figure 36	Two-dimensional distribution of $dE/dx$ versus charge signed momentum ( $qp$ ) for minimum-bias tracks. The fitted distributions of the most probable values for pions, kaons and protons are superimposed. . . . .	67
257			
258			
259			
260	Figure 37	The distribution of mass estimated using $dE/dx$ for simulated stable R-Hadrons with masses between 1000 and 1600 GeV. . . . .	68
261			
262			
263	Figure 38	The acceptance $\times$ efficiency as a function of R-Hadron (a) mass and (b) lifetime. (a) shows all of the combinations of mass and lifetime considered in this search, and (b) highlights the lifetime dependence for 1000 GeV and 1600 GeV R-Hadrons. . . . .	70
264			
265			
266			
267			

268	Figure 39	The distribution of (a) $dE/dx$ and (b) momentum for tracks in data and simulated signal after requiring the event level selection and the track selection on $p_T$ , hits, and $N_{\text{split}}$ . Each sub-figure shows the normalized distributions for tracks classified as hadrons, electrons, and muons in data and R-Hadrons in the simulated signal. . . . .	72
275	Figure 40	The distribution of $M_{dE/dx}$ (a) before and (b) after the ionization requirement for tracks in simulated W boson decays and for the randomly generated background estimate. . . . .	74
279	Figure 41	The distribution of $M_{dE/dx}$ (a) before and (b) after the ionization requirement for tracks in the validation region and for the randomly generated background estimate. . . . .	75
283	Figure 42	The trigger efficiency for the HLT_xe70 trigger requirement as a function of Calorimeter $E_T^{\text{miss}}$ for simulated data events with a W boson selection. Simulated signal events and simulated W boson events are also included. . . . .	80
288	Figure 43	The efficiency of the muon veto for R-hadrons of two different masses, as a function of $\frac{1}{\beta}$ for simulated R-Hadron tracks. . . . .	82
291	Figure 44	The average reconstructed MDT $\beta$ distribution for $Z \rightarrow \mu\mu$ events in which one of the muons is reconstructed as a slow muon, for both data and simulation. A gaussian fit is superimposed. . . . .	83

295 LIST OF TABLES

307 LISTINGS

---

<small>308</small> Listing 1	A floating example ( <code>listings</code> manual)	94
------------------------------	--	----

309 ACRONYMS

---

- 310 SM Standard Model  
311 SUSY Supersymmetry  
312 LSP Lightest Supersymmetric Particle  
313 LHC Large Hadron Collider  
314 ATLAS A Toroidal LHC ApparatuS  
315 ToT time over threshold  
316 LCW local cluster weighted  
317 MIP minimally ionizing particle  
318 EPJC European Physical Journal C  
319 JES jet energy scale  
320 LLP Long-Lived Particle  
321 CR Control Region  
322 NLO next-to-leading order  
323 NLL next-to-leading logarithmic  
324 PDF parton distribution function  
325 ISR initial state radiation  
326 RMS root mean square  
327 IBL Insertible B-Layer  
328 CP Combined Performance

329

## PART I

330

### INTRODUCTION

331

You can put some informational part preamble text here.



# 1

332

## 333 INTRODUCTION

---



334

## PART II

335

### THEORETICAL CONTEXT

336

You can put some informational part preamble text here.



# 2

337

## 338 STANDARD MODEL

---

339 The SM of particle physics seeks to explain the symmetries and interactions of  
340 all currently discovered fundamental particles. It has been tested by several genera-  
341 tions of experiments and has been remarkably successful, no significant de-  
342 viations have been found. The SM provides predictions in particle physics for  
343 interactions up to the Planck scale ( $10^{15}$ - $10^{19}$  GeV).

344 The theory itself is a quantum field theory grown from an underlying  $SU(3) \times$   
345  $SU(2) \times U(1)$  that requires the particle content and quantum numbers consist-  
346 ent with experimental observations (see Section 2.1). Each postulated symme-  
347 try is accompanied by an interaction between particles through gauge invari-  
348 ance. These interactions are referred to as the Strong, Weak, and Electromag-  
349 netic forces, which are discussed in Section 2.2.

350 Although this model has been very predictive, the theory is incomplete; for  
351 example, it is not able to describe gravity or astronomically observed dark matter.  
352 These limitations are discussed in more detail in Section 2.3.

## 353 21 PARTICLES

354 The most familiar matter in the universe is made up of protons, neutrons, and  
355 electrons. Protons and neutrons are composite particles, however, and are made  
356 up in turn by particles called quarks. Quarks carry both electric charge and color  
357 charge, and are bound in color-neutral combinations called baryons. The elec-  
358 tron is an example of a lepton, and carries only electric charge. Another type  
359 of particle, the neutrino, does not form atomic structures in the same way that  
360 quarks and leptons do because it carries no color or electric charge. Collectively,  
361 these types of particles are known as fermions, the group of particles with half-  
362 integer spin.

363 There are three generations of fermions, although familiar matter is formed  
364 predominantly by the first generation. The generations are identical except for  
365 their masses, which increase in each generation by convention. In addition, each  
366 of these particles is accompanied by an antiparticle, with opposite-sign quantum  
367 numbers but the same mass.

368 The fermions comprise what is typically considered matter, but there are  
369 additional particles that are mediators of interactions between those fermions.  
370 These mediators are known as the gauge bosons, gauge in that their existence  
371 is required by gauge invariance (discussed further in Section 2.2) and bosons in  
372 that they have integer spin. The boson which mediates the electromagnetic force  
373 is the photon, the first boson to be discovered; it has no electric charge, no mass,  
374 and a spin of 1. There are three spin-1 mediators of the weak force, the two  
375 W bosons and the Z boson. The W bosons have electric charge of  $\pm 1$  and a  
376 mass of  $80.385 \pm 0.015$  GeV, while the Z boson is neutral and has a mass of

377 91.1876  $\pm$  0.0021 GeV. The strong force is mediated by eight particles called  
 378 gluons, which are massless and electrically neutral but do carry color charge.

379 The final particle present in the SM is the Higgs boson, which was recently  
 380 observed for the first time by experiments at CERN in 2012. It is electrically  
 381 neutral, has a mass of 125.7  $\pm$  0.4 GeV, and is the only spin-0 particle yet to be  
 382 observed. The Higgs boson is the gauge boson associated with the mechanism  
 383 that gives a mass to the W and Z bosons.

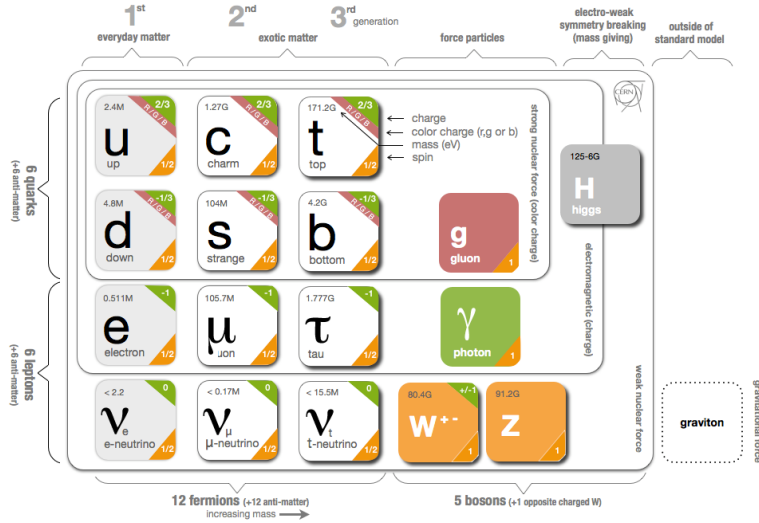


Figure 1: The particle content of the SM.

384 Together these particles form the entire content of the SM, and are summa-  
 385 rized in Figure 1. These are the particles that constitute the observable universe  
 386 and all the so-far-observed interactions within it.

## 387 2.2 INTERACTIONS

388 The interactions predicted and described by the SM are fundamentally tied to the  
 389 particles within it, both in that they describe the way those particles can influence  
 390 each other and also in that the existence of the interactions requires the existence  
 391 of some particles (the gauge bosons).

## 392 2.3 LIMITATIONS

# 3

393

394 SUPERSYMMETRY

---

395 3.1 MOTIVATION

396 3.2 STRUCTURE

397 3.3 PHENOMENOLOGY



# 4

398

399 LONG-LIVED PARTICLES

---

400 4.1 MECHANISMS

401 4.1.1 EXAMPLES IN SUPERSYMMETRY

402 4.2 PHENOMENOLOGY

403 4.2.1 DISIMILARITIES TO PROMPT DECAYS

404 4.2.2 CHARACTERISTIC SIGNATURES



405

### PART III

406

## EXPERIMENTAL STRUCTURE AND RECONSTRUCTION

407

You can put some informational part preamble text here.



# 5

408

409 THE LARGE HADRON COLLIDER

---

410 5.1 INJECTION CHAIN

411 5.2 DESIGN AND PARAMETERS

412 5.3 LUMINOSITY



# 6

413

## 414 THE ATLAS DETECTOR

---

### 415 6.1 COORDINATE SYSTEM

### 416 6.2 MAGNETIC FIELD

### 417 6.3 INNER DETECTOR

#### 418 6.3.1 PIXEL DETECTOR

#### 419 6.3.2 SEMICONDUCTOR TRACKER

#### 420 6.3.3 TRANSITION RADIATION TRACKER

### 421 6.4 CALORIMETRY

#### 422 6.4.1 ELECTROMAGNETIC CALORIMETERS

#### 423 6.4.2 HADRONIC CALORIMETERS

#### 424 6.4.3 FORWARD CALORIMETERS

### 425 6.5 MUON SPECTROMETER

### 426 6.6 TRIGGER

#### 427 6.6.1 TRIGGER SCHEME

#### 428 6.6.2 MISSING TRANSVERSE ENERGY TRIGGERS



# 7

429

## 430 EVENT RECONSTRUCTION

---

431 The ATLAS experiment combines measurements in the subdetectors to form a  
432 cohesive picture of each physics event.

## 433 7.1 TRACKS AND VERTICES

### 434 7.1.1 TRACK RECONSTRUCTION

#### 435 7.1.1.1 NEURAL NETWORK

#### 436 7.1.1.2 PIXEL DE/DX

### 437 7.1.2 VERTEX RECONSTRUCTION

## 438 7.2 JETS

### 439 7.2.1 TOPOLOGICAL CLUSTERING

### 440 7.2.2 JET ENERGY SCALE

### 441 7.2.3 JET ENERGY SCALE UNCERTAINTIES

### 442 7.2.4 JET ENERGY RESOLUTION

## 443 7.3 ELECTRONS

### 444 7.3.1 ELECTRON IDENTIFICATION

## 445 7.4 MUONS

### 446 7.4.1 MUON IDENTIFICATION

## 447 7.5 MISSING TRANSVERSE ENERGY



448

## PART IV

449

### CALORIMETER RESPONSE

450

You can put some informational part preamble text here.



# 8

451

## 452 RESPONSE MEASUREMENT WITH SINGLE HADRONS

---

453 As discussed in Section 7.2, colored particles produced in collisions hadronize  
454 into jets of multiple hadrons. One approach to understanding jet energy mea-  
455 surements in the ATLAS calorimeters is to evaluate the calorimeter response to  
456 those individual hadrons; measurements of individual hadrons can be used to  
457 build up an understanding of the jets that they form. The redundancy of the  
458 momentum provided by the tracking system and the energy provided by the  
459 calorimeter provides an opportunity to study calorimeter response using real  
460 collisions, as described further in Section 8.2.

461 Calorimeter response includes a number of physical effects that can be ex-  
462 tracted to provide insight into many aspects of jet modeling. First, many charged  
463 hadrons interact with the material of the detector prior to reaching the calorime-  
464 ters and thus do not deposit any energy. Comparing this effect in data and simu-  
465 lation is a powerful tool in validating the interactions of particles with the mate-  
466 rial of the detector and the model of the detector geometry in simulation, see Sec-  
467 tion 8.2.2. The particles which do reach the calorimeter deposit their energy into  
468 several adjacent cells, which are then clustered together. The energy of the clus-  
469 ter is then the total energy deposited by that particle. Comparing the response of  
470 hadrons in data to that of simulated hadrons provides a direct evaluation of the  
471 showering of hadronic particles and the energy deposited by particles in matter  
(Section 8.2.4).

472 The above studies all use an inclusive selection of charged particles, which are  
473 comprised predominantly of pions, kaons, and (anti)protons. It is also possible to  
474 measure the response to various identified particle types separately to evaluate  
475 the simulated interactions of each particle, particularly at low energies where  
476 differences between species are very relevant. Pions and (anti)protons can be  
477 identified through decays of long-lived particles, in particular  $\Lambda$ ,  $\bar{\Lambda}$ , and  $K_S^0$ , and  
478 then used to measure response as described above. This is discussed in detail in  
479 Section 8.3.

480 The results in this chapter use data collected at 7 and 8 TeV collected in 2010  
481 and 2012, respectively. Both are included as the calorimeter was repaired and  
482 recalibrated between those two data-taking periods. Both sets of data are com-  
483 pared to an updated simulation that includes new physics models provided by  
484 Geant4 [1] and improvements in the detector description [2, 3]. The present  
485 results are published in European Physical Journal C (EPJC) [4] and can be com-  
486 pared to a similar measurement performed in 2009 and 2010 [5], which used the  
487 previous version of the simulation framework [6].

## 489 8.1 DATASET AND SIMULATION

## 490 8.1.1 DATA SAMPLES

491 The two datasets used in this chapter are taken from dedicated low-pileup runs  
 492 where the fraction of events with multiple interactions was negligible. These  
 493 datasets are used rather than those containing full-pileup events to facilitate mea-  
 494 surement of isolated hadrons. The 2012 dataset at  $\sqrt{s} = 8$  TeV contains 8 mil-  
 495 lion events and corresponds to an integrated luminosity of  $0.1 \text{ nb}^{-1}$ . The 2010  
 496 dataset at  $\sqrt{s} = 7$  TeV contains 3 million events and corresponds to an inte-  
 497 grated luminosity of  $3.2 \text{ nb}^{-1}$ . The latter dataset was also used for the 2010 re-  
 498 sults [5], but it has since been reanalyzed with an updated reconstruction includ-  
 499 ing the final, best understanding of the detector description for the material and  
 500 alignment from Run 1.

## 501 8.1.2 SIMULATED SAMPLES

502 The two datasets above are compared to simulated single-, double-, and non-  
 503 diffractive events generated with Pythia8 [7] using the A2 configuration of  
 504 hadronization [8] and the MSTW 2008 parton-distribution function set [9, 10].  
 505 The admixture of the single-, double-, and non-diffractive events uses the default  
 506 relative contributions from Pythia8. The conditions and energies for the two  
 507 simulations are chosen so that they match those of the corresponding dataset.

508 To evaluate the interaction of hadrons with detector material, the simulation  
 509 uses two different collections of hadronic physics models, called physics lists, in  
 510 Geant4 9.4 [11]. The first, QGSP\_BERT, combines the Bertini intra-nuclear  
 511 cascade [12–14] below 9.9 GeV, a parametrized proton inelastic model from 9.5  
 512 to 25 GeV [15], and a quark-gluon string model above 12 GeV [16–20]. The  
 513 second, FTFP\_BERT, combines the Bertini intra-nuclear cascade [12–14] below  
 514 5 GeV and the Fritiof model [21–24] above 4 GeV. In either list, Geant4 en-  
 515 forces a smooth transition between models where multiple models overlap.

## 516 8.1.3 EVENT SELECTION

517 The event selection for this study is minimal, as the only requirement is selecting  
 518 good-quality events with an isolated track. Such events are triggered by requir-  
 519 ing at least two hits in the minimum-bias trigger scintillators. After trigger, each  
 520 event is required to have exactly one reconstructed vertex, and that vertex is re-  
 521 quired to have four or more associated tracks.

522 The particles which are selected for the response measurements are first iden-  
 523 tified as tracks in the inner detector. The tracks are required to have at least 500  
 524 MeV of transverse momentum. To ensure a reliable momentum measurement,  
 525 these tracks are required to have at least one hit in the pixel detector, six hits in  
 526 the SCT, and small longitudinal and transverse impact parameters with respect  
 527 to the primary vertex [5]. For the majority of the measurements in this chapter,  
 528 the track is additionally required to have 20 hits in the TRT, which significantly

529 reduces the contribution from tracks which undergo nuclear interactions. This  
 530 requirement and its effect is discussed in more detail in Section 8.2.5. In addition,  
 531 tracks are rejected if there is any other reconstructed track which extrapolates  
 532 to the calorimeter within a cone of  $\Delta R = \sqrt{(\Delta\phi)^2 + (\Delta\eta)^2} < 0.4$ . This require-  
 533 ment guarantees that the contamination of energy from nearby charged particles  
 534 is negligible [5].

## 535 8.2 INCLUSIVE HADRON RESPONSE

536 The calorimeter response is more precisely defined as the ratio of the measured  
 537 calorimeter energy to the true energy carried by the particle, although this true  
 538 energy is unknown. For charged particles, however, the inner detector provides  
 539 a very precise measurement of momentum (with uncertainty less than 1%) that  
 540 can be used as a proxy for true energy. The ratio of the energy deposited by  
 541 the charged particle in the calorimeter,  $E$ , to its momentum measured in the  
 542 inner detector  $p$ , forms the calorimeter response measure called  $E/p$ . Though  
 543 the distribution of  $E/p$  contains a number of physical features, this study focuses  
 544 on the trends in two aggregated quantities:  $\langle E/p \rangle$ , the average of  $E/p$  for the  
 545 selected tracks, and the zero fraction, the fraction of tracks with no associated  
 546 energy in the calorimeter for those tracks.

547 The calorimeter energy assigned to a track is defined using clusters. The clus-  
 548 ters are formed using a 4–2–0 algorithm [25] that begins with seeds requiring  
 549 at least 4 times the average calorimeter cell noise. The neighboring cells with  
 550 at least twice that noise threshold are then added to the cluster, and all bound-  
 551 ing cells are then added with no requirement. This algorithm minimizes noise  
 552 contributions through its seeding process, and including the bounding cells im-  
 553 proves the energy resolution [26]. The clusters are associated to a given track  
 554 if they fall within a cone of  $\Delta R = 0.2$  of the extrapolated position of the track,  
 555 which includes about 90% of the energy on average [5]. This construction is il-  
 556 lustrated in Figure 2.

### 557 8.2.1 E/P DISTRIBUTION

558 The  $E/p$  distributions measured in both data and simulation are shown in Fig-  
 559 ure 3 for two example bins of track momentum and for tracks in the central  
 560 region of the detector. These distributions show several important features of  
 561 the  $E/p$  observable. The large content in the bin at  $E = 0$  comes from tracks that  
 562 have no associated cluster, which occurs due to interactions with detector mate-  
 563 rial prior to reaching the calorimeter or the energy deposit being insufficiently  
 564 large to generate a seed, and are discussed in Section 8.2.2. The small negative  
 565 tail also comes from tracks that do not deposit any energy in the calorimeter but  
 566 are randomly associated to a cluster with an energy below the noise threshold.  
 567 The long positive tail above 1.0 comes from the contribution of neutral parti-  
 568 cles. Nearby neutral particles deposit (sometimes large) additional energy in the  
 569 calorimeter but do not produce tracks in the inner detector, so they cannot be  
 570 rejected by the track isolation requirement. Additionally the peak and mean of

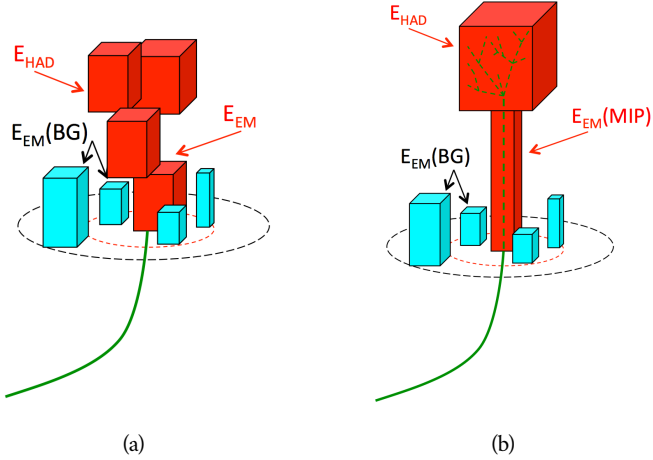


Figure 2: An illustration (a) of the  $E/p$  variable used throughout this paper. The red energy deposits come from the charged particle targeted for measurement, while the blue energy deposits are from nearby neutral particles and must be subtracted. The same diagram (b) for the neutral-background selection, described in Section 8.2.3.

the distribution falls below 1.0 because of the loss of energy not found within the cone as well as the non-compensation of the calorimeter.

573 The data and simulation share the same features, but the high and low tails  
574 are significantly different. The simulated events tend to overestimate the con-  
575 tribution of neutral particles to the long tail, an effect which can be isolated and  
576 removed as discussed in Section 8.2.3. Additionally, the simulated clusters have  
577 less noise on average, although this is a small effect on the overall response.

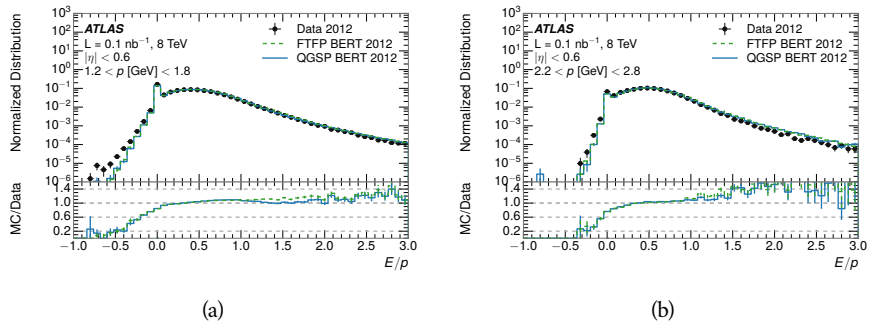


Figure 3: The  $E/p$  distribution and ratio of simulation to data for isolated tracks with (a)  $|\eta| < 0.6$  and  $1.2 < p/\text{GeV} < 1.8$  and (b)  $|\eta| < 0.6$  and  $2.2 < p/\text{GeV} < 2.8$ .

578 8.2.2 ZERO FRACTION

579 The fraction of particles with no associated clusters, or similarly those with  $E \leq$   
580 0, reflects the modeling of both the detector geometry and hadronic interactions.  
581 The zero fraction is expected to rise as the amount of material a particle traverses

increases, while it is expected to decrease as the particle energy increases. This dependence can be seen in Figure 4, where the zero fraction in data and simulation is shown as a function of momentum and the amount of material measured in interaction lengths. The trends are similar between 2010 and 2012 and for positively and negatively charged particles. The zero fraction decreases with energy as expected. The absolute discrepancy in zero fraction decreases with momentum from 5% to less than 1%, but this becomes more pronounced in the ratio as the zero fraction shrinks quickly with increasing momentum. There is a small constant difference between the data and simulation in both interaction models that becomes more pronounced. The amount of material in the detector increases with  $\eta$ , which is used to obtain results for interaction lengths ranging between 0.1 and 0.65  $\lambda$ . As the data and simulation have significant disagreement in the zero fraction over a number of interaction lengths, the difference must be primarily from the modeling of hadronic interactions with detector material and not just the detector geometry. Although two different hadronic interaction models are shown in the figure, they have very similar discrepancies to data because both use the same description (the BERT model) at low momentum.

### 8.2.3 NEUTRAL BACKGROUND SUBTRACTION

The isolation requirement on hadrons is only effective in removing an energy contribution from nearby charged particles. Nearby neutral particles, predominantly photons from  $\pi^0$  decays, also add their energy to the calorimeter clusters, but mostly in the electromagnetic calorimeter. It is possible to measure this contribution, on average, using late-showering hadrons that minimally ionize in the electromagnetic calorimeter. Such particles are selected by requiring that they deposit less than 1.1 GeV in the EM calorimeter within a cone of  $\Delta R < 0.1$  around the track. To ensure that these particles are well measured, they are additionally required to deposit between 40% and 90% of their energy in the hadronic calorimeter within the same cone.

These particles provide a clean sample to measure the nearby neutral background because they do not deposit energy in the area immediately surrounding them in the EM calorimeter, as shown in Figure 2. So, the energy deposits in the region  $0.1 < \Delta R < 0.2$  can be attributed to neutral particles alone. To estimate the contribution to the whole cone considered for the response measurement, that energy is scaled by a geometric factor of 4/3. This quantity,  $\langle E/p \rangle_{\text{BG}}$ , measured in aggregate over a number of particles, gives the contribution to  $\langle E/p \rangle$  from neutral particles in the EM calorimeter. Similar techniques were used in the individual layers of the hadronic calorimeters to show that the background from neutrals is negligible in those layers [5].

The distribution of this background estimate is shown in Figure 5 for data and simulation with the two different physics lists. The contribution from neutral particles falls from 0.1 at low momentum to around 0.03 for particles above 7 GeV. Although the simulation captures the overall trend, it significantly overestimates the neutral contribution for tracks with momentum between 2 and 8 GeV. This effect was also seen in the tails of the  $E/p$  distributions in Figure 3.

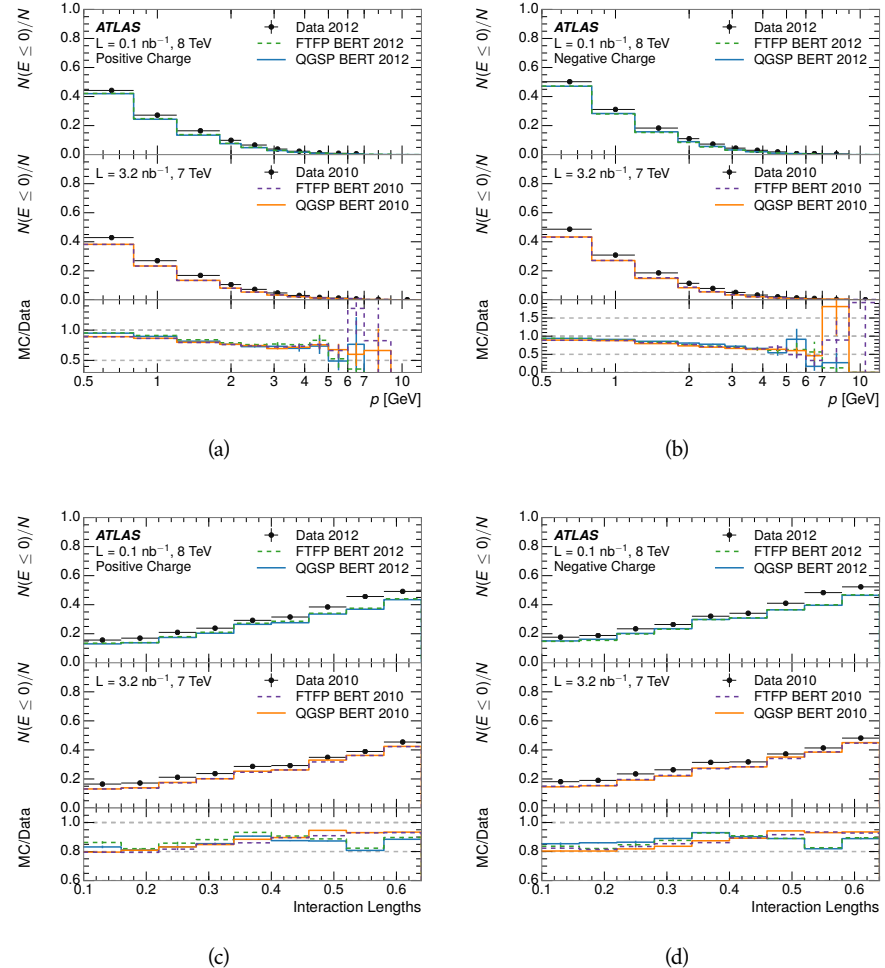


Figure 4: The fraction of tracks as a function (a, b) of momentum, (c, d) of interaction lengths with  $E \leq 0$  for tracks with positive (on the left) and negative (on the right) charge.

626 This difference is likely due to modeling of coherent neutral particle radiation  
 627 in Pythia8 that overestimates the production of  $\pi^0$  near the production of the  
 628 charged particles. The discrepancy does not depend on  $\eta$  and thus is unlikely to  
 629 be a mismodeling of the detector. This difference can be subtracted to form a  
 630 corrected average  $E/p$ , as in Section 8.2.4.

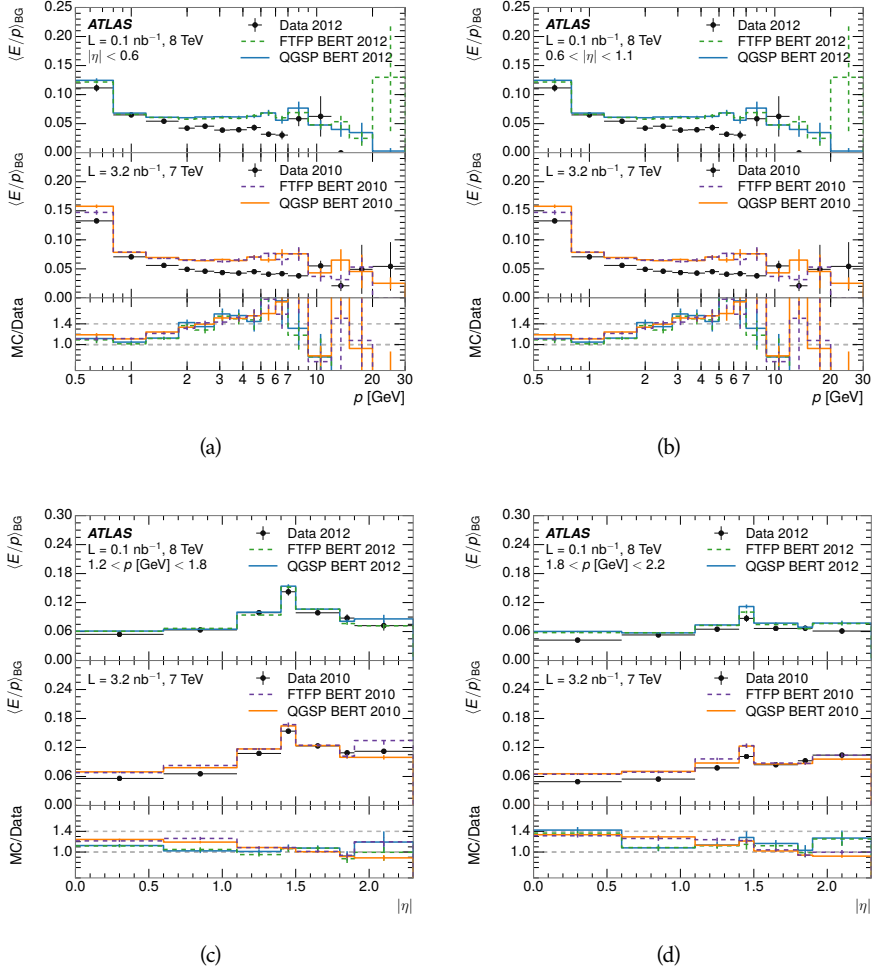


Figure 5:  $\langle E/p \rangle_{\text{BG}}$  as a function of the track momentum for tracks with (a)  $|\eta| < 0.6$ , (b)  $0.6 < |\eta| < 1.1$ , and as a function of the track pseudorapidity for tracks with (c)  $1.2 < p/\text{GeV} < 1.8$ , (d)  $1.8 < p/\text{GeV} < 2.2$ .

#### 631 8.2.4 CORRECTED RESPONSE

632 Figure 6 shows  $\langle E/p \rangle_{\text{COR}}$  as a function of momentum for several bins of pseudo-  
 633 rapidity. This corrected  $\langle E/p \rangle_{\text{COR}} \equiv \langle E/p \rangle - \langle E/p \rangle_{\text{BG}}$  measures the average  
 634 calorimeter response without the contamination of neutral particles. It is the  
 635 most direct measurement of calorimeter response in that it is the energy mea-  
 636 sured for fully isolated hadrons. The correction is performed separately in data  
 637 and simulation, so that the mismodeling of the neutral background in simulation  
 638 is removed from the comparison of response. The simulation overestimates the

639 response at low momentum by about 5%, an effect that can be mostly attributed  
 640 to the underestimation of the zero fraction mentioned previously. For  $|\eta| < 0.6$ ,  
 641 the data-simulation agreement has a larger discrepancy by about 5% for 2010  
 642 than 2012, although this is not reproduced in at higher pseudorapidity.

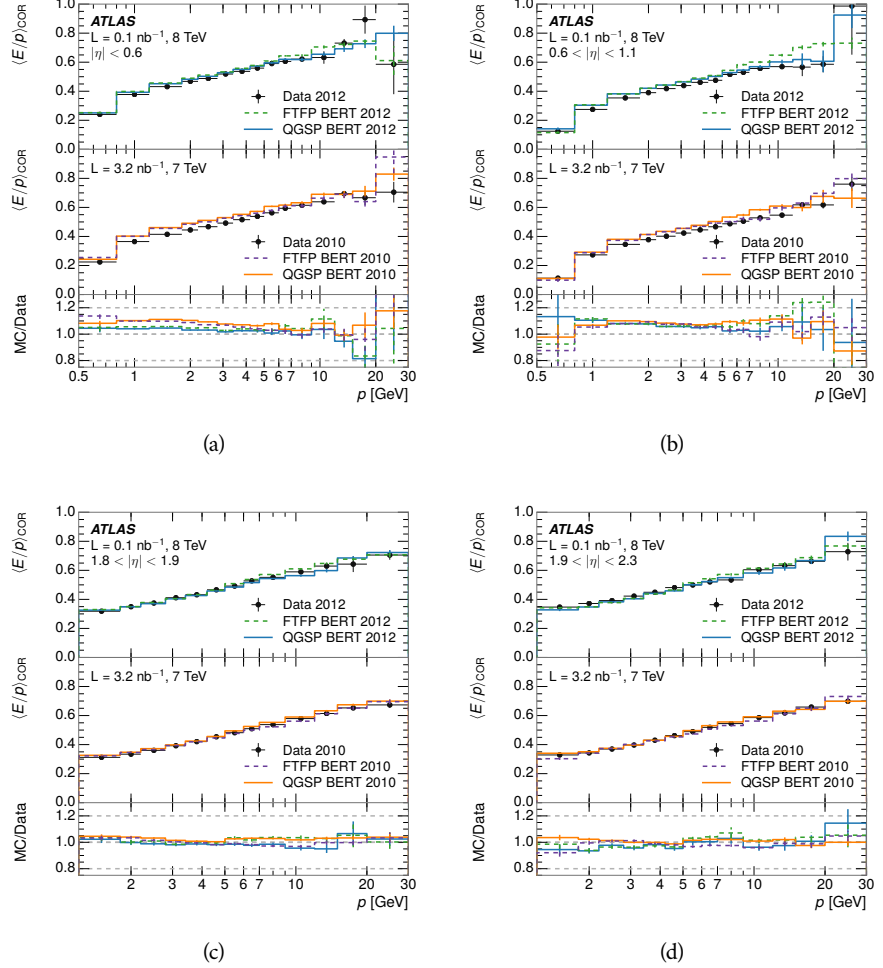


Figure 6:  $\langle E/p \rangle_{\text{COR}}$  as a function of track momentum, for tracks with (a)  $|\eta| < 0.6$ , (b)  $0.6 < |\eta| < 1.1$ , (c)  $1.8 < |\eta| < 1.9$ , and (d)  $1.9 < |\eta| < 2.3$ .

643 The response measurement above used topological clustering at the EM scale,  
 644 that is clusters were formed to measure energy but no corrections were applied  
 645 to correct for expected effects like energy lost outside of the cluster or in unin-  
 646 strumented material. It is also interesting to measure  $\langle E/p \rangle_{\text{COR}}$  using local clus-  
 647 ter weighted ([LCW](#)) energies, which accounts for those effects by calibrating the  
 648 energy based on the properties of the cluster such as energy density and depth in  
 649 the calorimeter. Figure 7 shows these distributions for tracks with zero or more  
 650 clusters and separately for tracks with one or more clusters. The calibration  
 651 moves the mean value of  $\langle E/p \rangle_{\text{COR}}$  significantly closer to 1.0 as desired. The  
 652 agreement between data and simulation improves noticeably when at least one  
 653 cluster is required, as this removes the contribution from the mismodeling of  
 654 the zero fraction. The good agreement in that case again demonstrates that the

difference in  $\langle E/p \rangle_{\text{COR}}$  between data and simulation is caused predominantly by the difference in zero fraction.

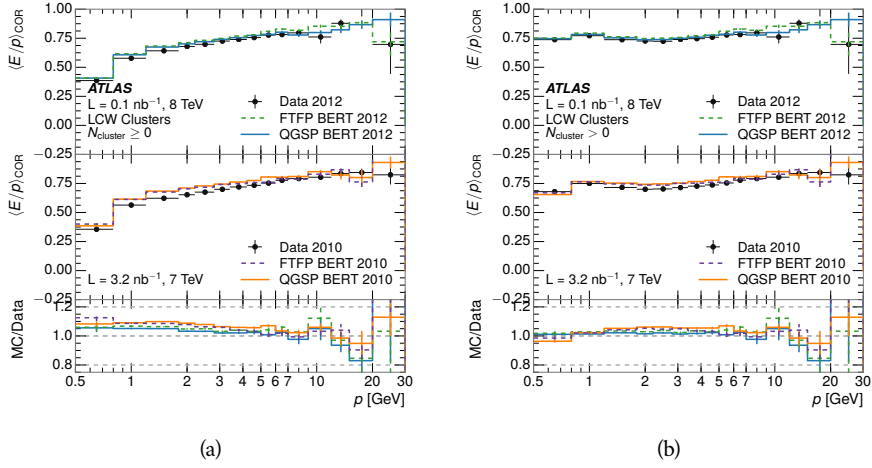


Figure 7:  $\langle E/p \rangle_{\text{COR}}$  calculated using LCW-calibrated topological clusters as a function of track momentum for tracks with (a) zero or more associated topological clusters or (b) one or more associated topological clusters.

### 8.2.5 ADDITIONAL STUDIES

As has been seen in several measurements in previous sections, the simulation does not correctly model the chance of a low momentum hadron to reach the calorimeter. Because of the consistent discrepancy across pseudorapidity and interaction lengths, this can be best explained by incomplete understanding of hadronic interactions with the detector [4]. For example, a hadron that scatters off of a nucleus in the inner detector can be deflected through a significant angle and not reach the expected location in the calorimeter. In addition, these interactions can produce secondary particles that are difficult to model.

The requirement used throughout the previous sections on the number of hits in the TRT reduces these effects by preferentially selecting tracks that do not undergo nuclear interactions. It is interesting to check how well the simulation models tracks with low numbers of TRT hits, which selects tracks that are more likely to have undergone a hadronic interaction. Figure 8 compares the distributions with  $N_{\text{TRT}} < 20$  to  $N_{\text{TRT}} > 20$  for real and simulated particles. As expected, the tracks with fewer hits are poorly modeled in the simulation as  $\langle E/p \rangle_{\text{COR}}$  differs by as much as 25% at low momentum.

Another interesting aspect of the simulation is the description of antiprotons at low momentum, where QGSP\_BERT and FTFP\_BERT have significant differences. This can be seen to have an effect in the inclusive response measurement when separated into positive and negative charge. The  $\langle E/p \rangle_{\text{COR}}$  distributions for positive and negative particles are shown in Figure 9, where a small difference between QGSP\_BERT and FTFP\_BERT can be seen in the distribution for negative tracks. This is demonstrated more clearly in Figure 10, which shows

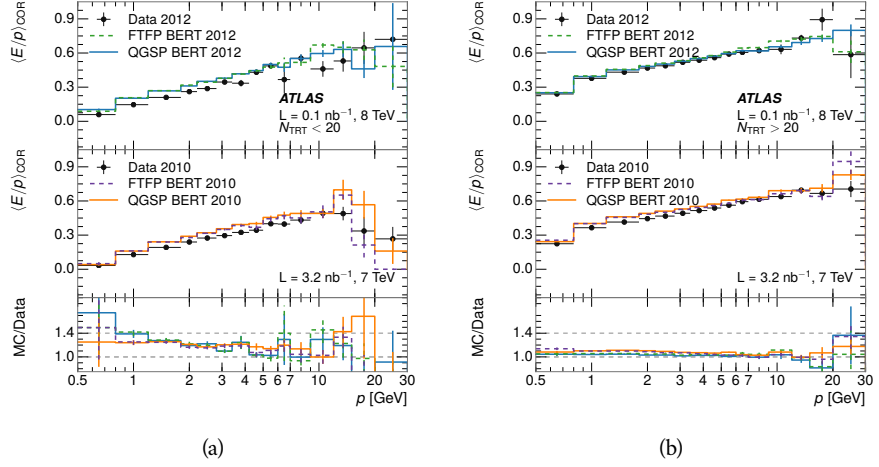


Figure 8: Comparison of the  $\langle E/p \rangle_{\text{COR}}$  for tracks with (a) less than and (b) greater than 20 hits in the TRT.

the  $E/p$  distribution in the two simulations separated by charge. There is a clear difference around  $E/p > 1.0$ , which can be explained by the additional energy deposited by the annihilation of the antiproton in the calorimeter that is modeled well only in FTFP\_BERT. This is also explored with data using identified antiprotons in Section 8.3.

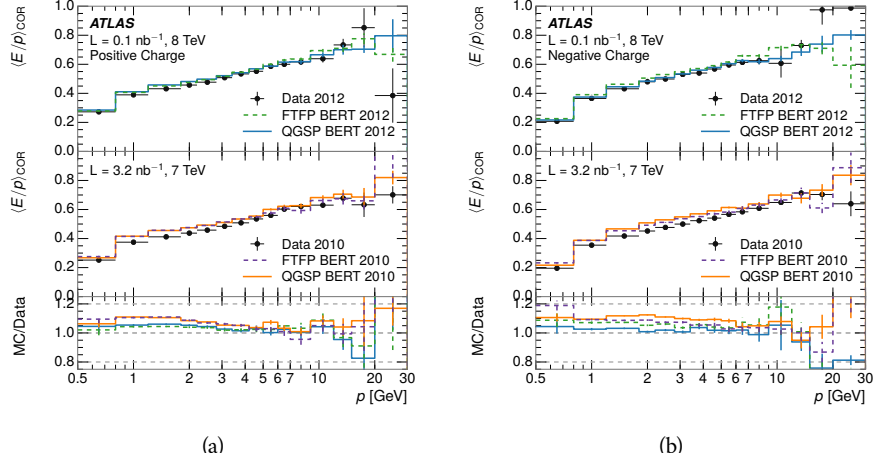


Figure 9: Comparison of the  $\langle E/p \rangle_{\text{COR}}$  for (a) positive and (b) negative tracks as a function of track momentum for tracks with  $|\eta| < 0.6$ .

The  $\langle E/p \rangle$  results in previous sections have considered the electromagnetic and hadronic calorimeters together as a single energy measurement, to emphasize the total energy deposited for a given particle. However, the deposits in each calorimeter are available separately and  $\langle E/p \rangle$  can be constructed for each layer. As the layers are composed of different materials and are modeled separately in the detector geometry, confirmation that the simulation matches the data well

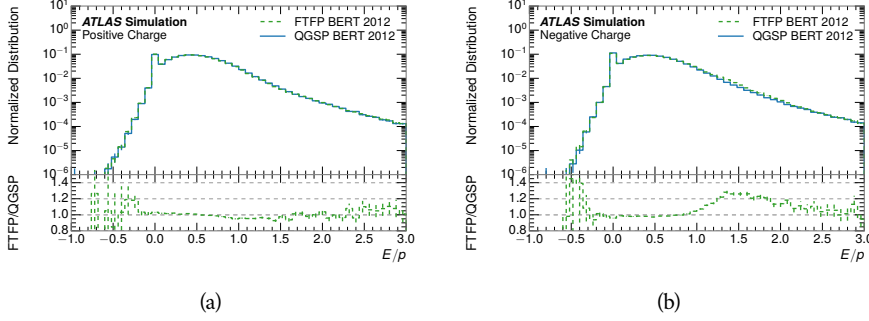


Figure 10: Comparison of the  $E/p$  distributions for (a) positive and (b) negative tracks with  $0.8 < p/\text{GeV} < 1.2$  and  $|\eta| < 0.6$ , in simulation with the FTFP\_BERT and QGSP\_BERT physics lists.

in each layer adds confidence in both the description of hadronic interactions with the two different materials and also the geometric description of each.

The technique discussed in Section 8.2.3 for selecting minimally ionizing particle (MIP)s in the electromagnetic calorimeter is also useful in studying deposits in the hadronic calorimeter. Those MIPs deposit almost all of their energy exclusively in the hadronic calorimeter. Figure 11 shows  $\langle E/p \rangle_{\text{RAW}}^{\text{Had}}$ , where RAW indicates that no correction has been applied for neutral backgrounds and Had indicates that only clusters for the hadronic calorimeter are included. The RAW and COR versions of  $\langle E/p \rangle$  in this case are the same, as the neutral background is negligible in that calorimeter layer. The distributions are shown both for the original EM scale calibration and after LCW calibration. The data and simulation agree very well in this comparison, except in the lowest momentum bin which has 5% discrepancy that has already been seen in similar measurements.

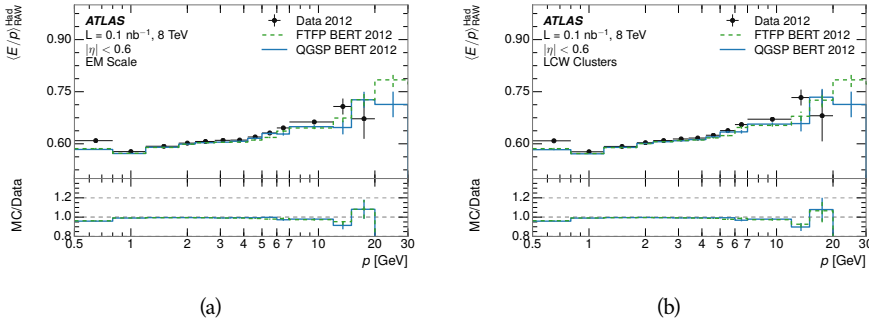


Figure 11: Comparison of the response of the hadronic calorimeter as a function of track momentum (a) at the EM-scale and (b) after the LCW calibration.

A similar comparison can be made in the electromagnetic calorimeter by selecting particles which have no associated energy in the hadronic calorimeter. These results are measured in terms of  $\langle E/p \rangle_{\text{COR}}^{\text{EM}}$ , where EM designates that only clusters in the electromagnetic calorimeter are included and COR designates that the neutral background is subtracted as the neutral background is present in this case. Figure 12 shows the analogous comparisons to Figure 11 in

711 the electromagnetic calorimeter. In this case the disagreement between data and  
 712 simulation is more pronounced, with discrepancies as high as 5% over a larger  
 713 range of momenta. This level of discrepancy indicates that the description of  
 714 the electromagnetic calorimeter is actually the dominant source of discrepancy  
 715 in the combined distributions in Section 8.2.4.

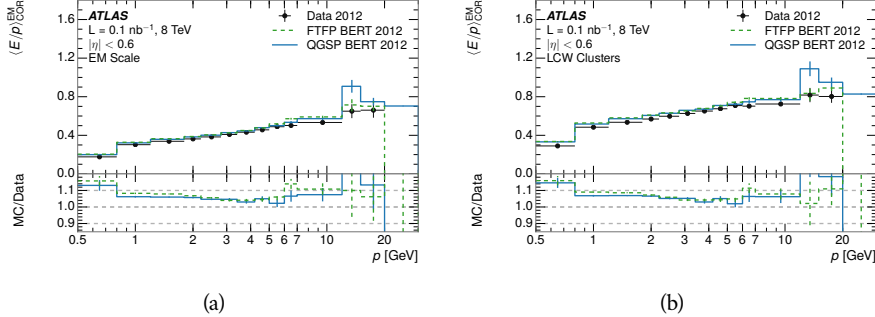


Figure 12: Comparison of the response of the EM calorimeter as a function of track momentum (a) at the EM-scale and (b) with the LCW calibration.

716 **NOTE: There are more studies that I skipped for brevity that could be in-**  
 717 **cluded if interesting.  $E/p$  at different cluster threshold settings,  $E/p$  with**  
 718 **pileup,  $E/p$  with cells. I also left out a lot of eta bins that appear in the**  
 719 **paper so that this section didn't turn into 20 pages of plots.**

### 720 8.3 IDENTIFIED PARTICLE RESPONSE

721 The inclusive response measurement for hadrons can be augmented by measur-  
 722 ing the response for specific particle species. The simulation models each parti-  
 723 cle type separately, and understanding the properties of each is important in con-  
 724 straining the uncertainty on jets. In order to select and measure specific hadrons,  
 725 this section relies on the displaced decays of long-lived particles. Such decays  
 726 can be identified by reconstructing secondary vertices with a requirement on  
 727 mass. In particular,  $\Lambda$ ,  $\bar{\Lambda}$ , and  $K_S^0$  can be used to select a pure sample of protons,  
 728 antiprotons, and pions, respectively.

#### 729 8.3.1 DECAY RECONSTRUCTION

730 The measurement of response for identified particles uses the same selection as  
 731 for inclusive particles (Section 8.1.3) with a few additions. Each event used is  
 732 required to have at least one secondary vertex, and the tracks are required to  
 733 match to that vertex rather than the primary vertex. Pions are selected from  
 734 decays of  $K_S^0 \rightarrow \pi^+ \pi^-$ , which is the dominant decay for  $K_S^0$  to charged particles.  
 735 Protons are selected from decays of  $\Lambda \rightarrow \pi^- p$  and antiprotons from  $\bar{\Lambda} \rightarrow \pi^+ \bar{p}$ ,  
 736 which are similarly the dominant decays of  $\Lambda$  and  $\bar{\Lambda}$  to charged particles. The  
 737 species of parent hadron in these decays is determined by reconstructing the  
 738 mass of the tracks associated to the secondary vertex. The sign of the higher

739 momentum decay particle can distinguish between  $\Lambda$  and  $\bar{\Lambda}$ , which of course  
 740 have the same mass, as the proton or antiproton is kinematically favored to have  
 741 higher momentum. Examples of the reconstructed masses used to select these  
 742 decays are shown in Figure 13.

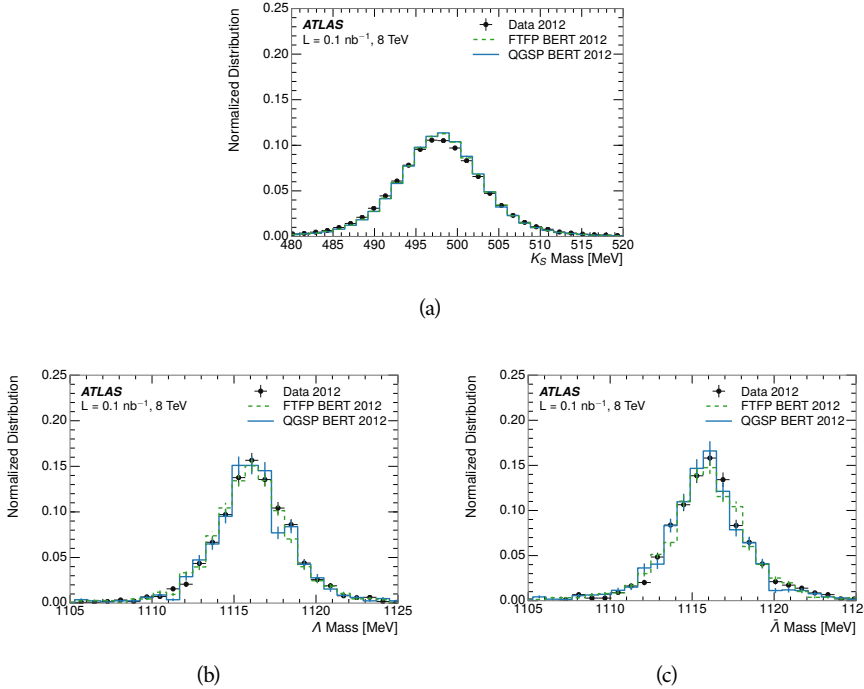


Figure 13: The reconstructed mass peaks of (a)  $K_S^0$ , (b)  $\Lambda$ , and (c)  $\bar{\Lambda}$  candidates.

743 The dominant backgrounds for the identified particle decays are nuclear in-  
 744 teractions and combinatoric sources. These are suppressed by the kinematic re-  
 745 quirements on the tracks as well as an additional veto which removes candidates  
 746 that are consistent with both a  $\Lambda$  or  $\bar{\Lambda}$  and a  $K_S^0$  hypothesis, which is possible be-  
 747 cause of the different assumptions on particle mass in each case [5]. After these  
 748 requirements, the backgrounds are found to be negligible compared to the sta-  
 749 tistical errors on these measurements.

### 750 8.3.2 IDENTIFIED RESPONSE

751 With these techniques the  $E/p$  distributions are extracted in data and simulation  
 752 for each particle species and shown in Figure 14. These distributions are shown  
 753 for a particular bin of  $E_a$  ( $2.2 < E_a/\text{GeV} < 2.8$ ), rather than  $p$ .  $E_a$  is the energy  
 754 available to be deposited in the calorimeter: for pions  $E_a = \sqrt{p^2 + m^2}$ , for pro-  
 755 tons  $E_a = \sqrt{p^2 + m^2} - m$ , and for antiprotons  $E_a = \sqrt{p^2 + m^2} + m$ . The features  
 756 of the  $E/p$  distributions are similar to the inclusive case. There is a small nega-  
 757 tive tail from noise and a large fraction of tracks with zero energy from particles  
 758 which do not reach the calorimeter. The long positive tail is noticeably more  
 759 pronounced for antiprotons because of the additional energy generated by the  
 760 annihilation in addition to the neutral background.

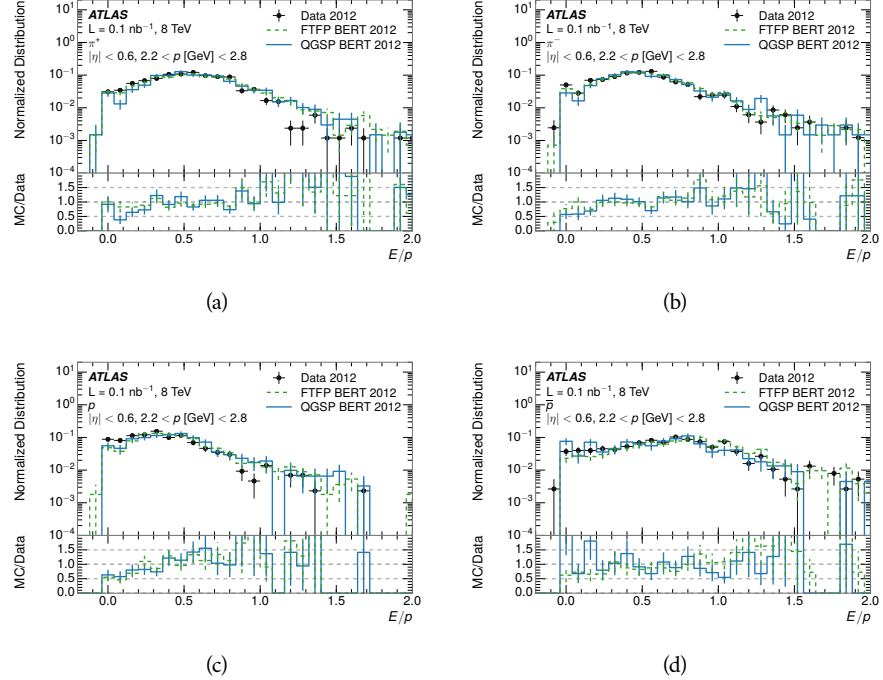


Figure 14: The  $E/p$  distribution for isolated (a)  $\pi^+$ , (b)  $\pi^-$ , (c) proton, and (d) anti-proton tracks.

The zero fraction is further explored in Figure 15 for pions and protons in data and simulation. The simulation consistently underestimates the zero fraction independent of particle species, which implies that this discrepancy is not caused by the model of a particular species but rather a feature common to all.

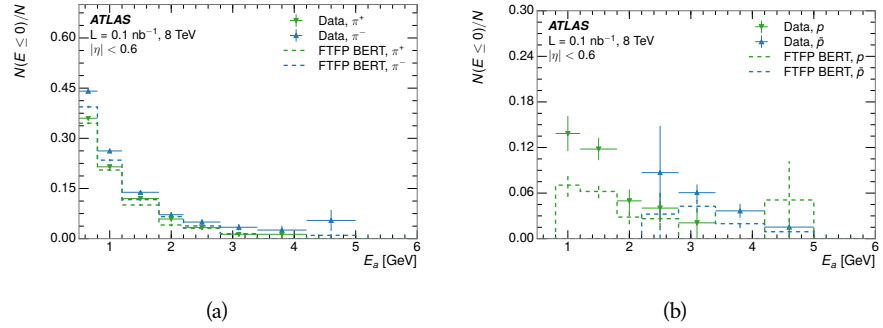


Figure 15: The fraction of tracks with  $E \leq 0$  for identified (a)  $\pi^+$  and  $\pi^-$ , and (b) proton and anti-proton tracks

It is also interesting to compare the response between the different particle species. One approach to do this is to measure the difference in  $\langle E/p \rangle$  between two types, which has the advantage of removing the neutral background. These differences are shown in various combinations in Figure 16. The response for  $\pi^+$  is greater on average than the response to  $\pi^-$  because of a charge-exchange effect which causes the production of additional neutral pions in the showers of

771  $\pi^+$  [27]. The response for  $\pi^+$  is also greater on average than the response to  $p$ ,  
 772 because a large fraction of the energy of  $\pi^+$  hadrons is converted to an electro-  
 773 magnetic shower [28, 29]. However, the  $\bar{p}$  response is significantly higher than  
 774 the response to  $\pi^-$  because of the annihilation of the antiproton. FTFP\_BERT  
 775 does a better job of modeling this effect than QGSP\_BERT because of their differ-  
 776 ent descriptions of  $\bar{p}$  interactions with material.

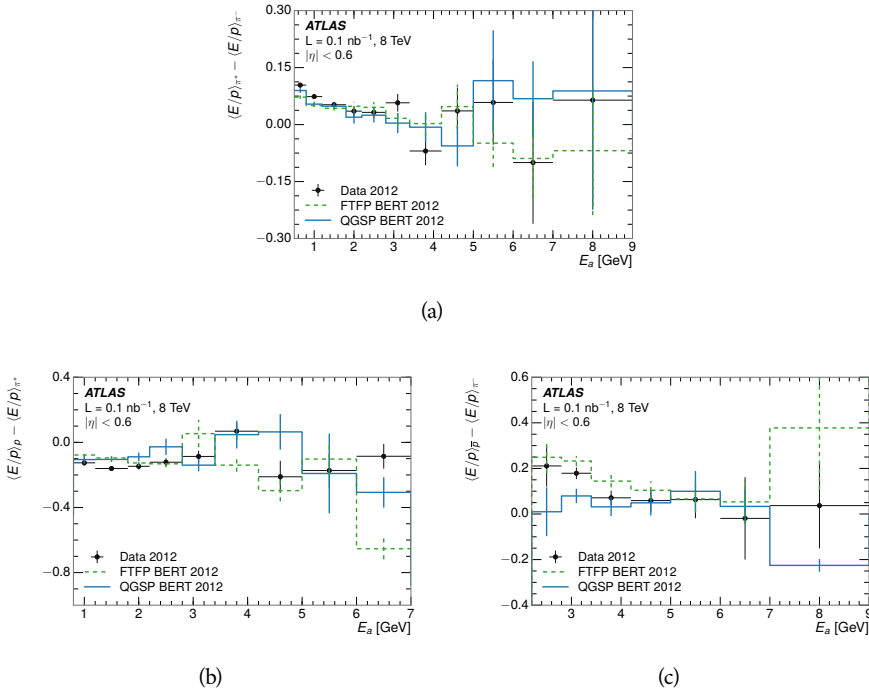


Figure 16: The difference in  $\langle E/p \rangle$  between (a)  $\pi^+$  and  $\pi^-$  (b)  $p$  and  $\pi^+$ , and (c)  $\bar{p}$  and  $\pi^-$ .

777 It is also possible to remove the neutral background from these response dis-  
 778 tributions using the same technique as in Section 8.2.3. The technique is largely  
 779 independent of the particle species and so can be directly applied to  $\langle E/p \rangle$  for  
 780 pions. The  $\langle E/p \rangle_{\text{COR}}$  distributions for pions are shown in Figure 17, which are  
 781 very similar to the inclusive results. The inclusive hadrons are comprised mostly  
 782 of pions, so this similarity is not surprising. It is also possible to see the small  
 783 differences between  $\pi^+$  and  $\pi^-$  response here, where  $\langle E/p \rangle_{\text{COR}}$  is higher on av-  
 784 erage for  $\pi^+$ . The agreement between data and simulation is significantly worse  
 785 for the  $\pi^-$  distributions than for the  $\pi^+$ , with a discrepancy greater than 10%  
 786 below 2-3 GeV.

### 787 8.3.3 ADDITIONAL SPECIES IN SIMULATION

788 The techniques above provide a method to measure the response separately for  
 789 only pions and protons. However the hadrons which forms jets include a num-  
 790 ber of additional species such as kaons and neutrons. The charged kaons are  
 791 an important component of the inclusive charged hadron distribution, which is  
 792 comprised of roughly 60-70% pions, 15-20% kaons, and 5-15% protons. These

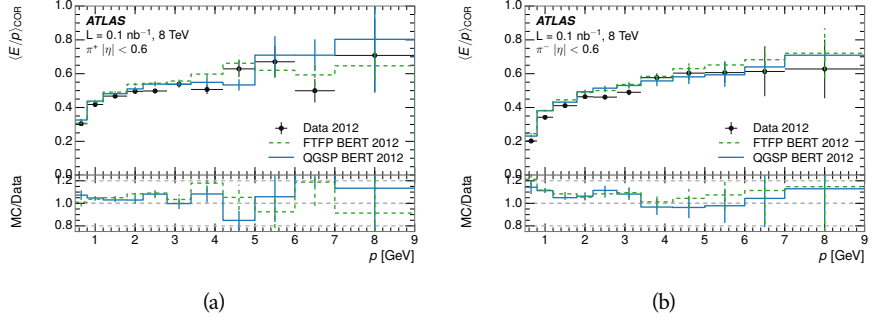


Figure 17:  $\langle E/p \rangle_{\text{COR}}$  as a function of track momentum for (a)  $\pi^+$  tracks and (b)  $\pi^-$  tracks.

are difficult to measure in data at the ATLAS detector, although a template subtraction technique has been proposed which may be effective with larger sample sizes [4]. The simulation of these particles includes noticeable differences in response at low energies, which are shown in Figure 18 for FTFP\_BERT. The significant differences in response between low energy protons and antiprotons are accounted for above in the definitions of  $E_a$ .

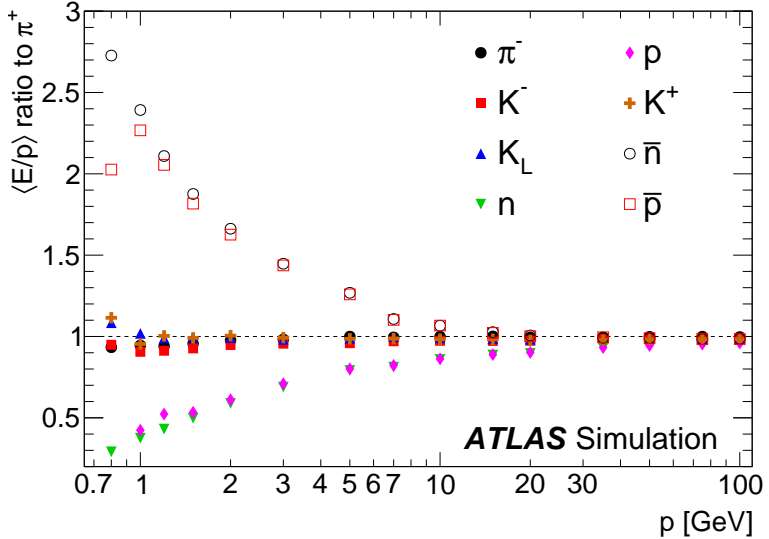


Figure 18: The ratio of the calorimeter response to single particles of various species to the calorimeter response to  $\pi^+$  with the physics list FTFP\_BERT.

#### 8.4 SUMMARY

These various measurements of calorimeter response shown above for data and simulation illuminate the accuracy of the simulation of hadronic interactions at the ATLAS detector. The results were done using 2010 and 2012 data at 7 and 8 TeV, but reflect the most current understanding of the detector alignment and geometry. A number of measurements focusing on a comparison between pro-

805 tons and antiprotons suggest that FTFP\_BERT models those interaction more  
806 accurately than QGSP\_BERT. These measurements, among others, were the moti-  
807 vation to switch the default Geant4 simulation from FTFP\_BERT to QGSP\_BERT  
808 for all ATLAS samples.

809 Even with these updates, there are a number of small, approximately 5%, dis-  
810 crepancies in response between the data and simulation at low energies. At  
811 higher energies the simulation of hadronic interactions is very consistent with  
812 data. Chapter 9 discusses how to use these observed differences to constrain the  
813 jet energy scale and its associated uncertainties.



814

## 815 JET ENERGY RESPONSE AND UNCERTAINTY

## 816 9.1 MOTIVATION

817 As jets form a major component of many physics analyses at ATLAS, it is cru-  
 818 cial to carefully calibrate the measurement of jet energies and to derive an un-  
 819 certainty on that measurement. These uncertainties have often been the dom-  
 820 inant systematic uncertainty in high-energy analyses at the Large Hadron Col-  
 821 lide (LHC). Dijet and multijet balance techniques provide a method to constrain  
 822 the JES and its uncertainty in data, and provide the default values used for ATLAS  
 823 jet measurements at most energies [30]. These techniques are limited by their re-  
 824 liance on measuring jets in data, so they are statistically limited in estimating  
 825 the jet energy scale at the highest jet energies. This chapter presents another  
 826 method for estimating the jet energy scale and its uncertainty which builds up a  
 827 jet from its components and thus can be naturally extended to high jet momen-  
 828 tum. Throughout this chapter the jets studied are simulated using Pythia8 with  
 829 the CT10 parton distribution set [31] and the AU2 tune [8], and corrections are  
 830 taken from the studies including data and simulation in Chapter 8.

831 As described in Section 7.2, jets are formed from topological clusters of energy  
 832 in the calorimeters using the anti- $k_t$  algorithm. These clusters originate from a  
 833 diverse spectrum of particles, in terms of both species and momentum, leading to  
 834 significantly varied jet properties and response between jets of similar produced  
 835 momentum. Figure 19 shows the simulated distribution of particles within jets  
 836 at a few examples energies. The  $E/p$  measurements provide a thorough under-  
 837 standing of the dominant particle content of jets, the charged hadrons.

## 838 9.2 UNCERTAINTY ESTIMATE

839 Simulated jets are not necessarily expected to correctly model the energy de-  
 840 posits in the calorimeters, because of the various discrepancies discussed in Chap-  
 841 ter 8. To evaluate a jet energy response, the simulated jet energies are compared  
 842 to a corrected jet built up at the particle level. Each cluster in a jet is associated  
 843 to the truth particle which deposited it, and the energy in that cluster is then  
 844 corrected for a number of effects based on measurements in data. The primary  
 845 corrections come from the single hadron response measurements in addition  
 846 to response measured using the combined test beam which covers higher mo-  
 847 mentum particles [32]. These corrections include both a shift ( $\Delta$ ), in order to  
 848 make the simulation match the average response in data, and an uncertainty ( $\sigma$ )  
 849 associated with the ability to constrain the difference between data and simula-  
 850 tion. Some of the dominant sources of uncertainty are itemized in Table 1 with  
 851 typical values, and the full list considered is described in detail in the associated

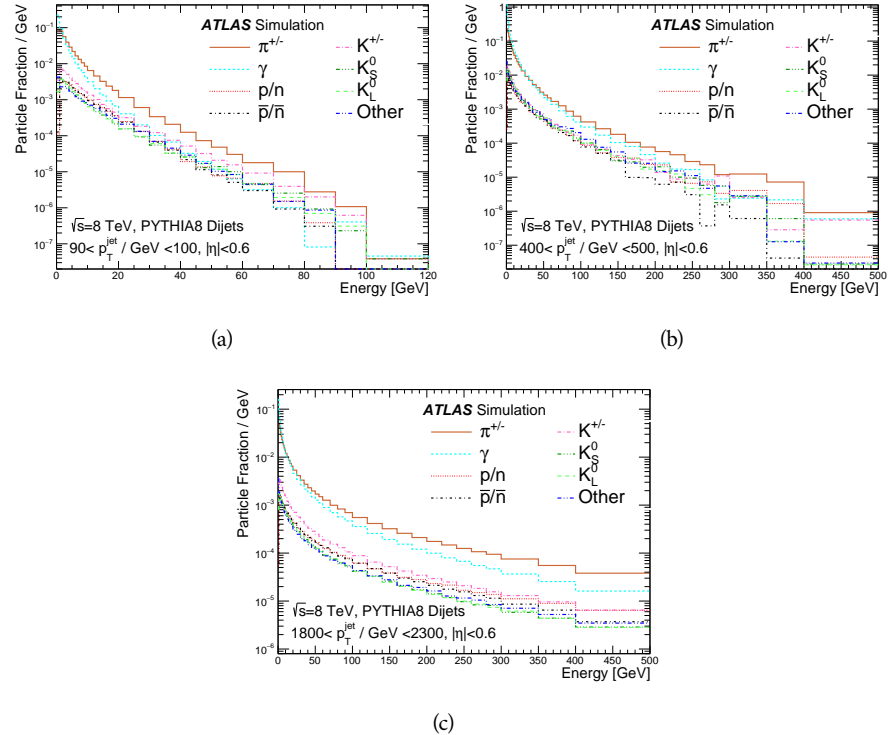


Figure 19: The spectra of true particles inside anti- $k_t$ ,  $R = 0.4$  jets with (a)  $90 < p_T/\text{GeV} < 100$ , (b)  $400 < p_T/\text{GeV} < 500$ , and (c)  $1800 < p_T/\text{GeV} < 2300$ .

paper [4]. These uncertainties cover differences between the data and simulation in the modeling of calorimeter response to a given particle. No uncertainties are added for the difference between particle composition of jets in data and simulation.

From these terms, the jet energy scale and uncertainty is built up from individual energy deposits in simulation. Each uncertainty term is treated independently, and are taken to be gaussian distributed. The resulting scale and uncertainty is shown in Figure 20, where the mean response is measured relative to the calibrated energy reported by simulation. The dominant uncertainties come from the statistical uncertainties on the  $E/p$  measurements at lower energies and the additional uncertainty for out of range measurements at higher energies. The total uncertainty from this method at intermediate jet energies is comparable to other simulation-based methods [33] and is about twice as large as in-situ methods using data [30]. This method is the only one which provides an estimation above 1.8 TeV, however, and so is still a crucial technique in analyses that search for very energetic jets.

These techniques can also be used to measure the correlation between bins of average reconstructed jet momentum across a range of  $p_T$  and  $|\eta|$ , where correlations are expected because of a similarity in particle composition at similar energies. Figure 21 shows these correlations, where the uncertainties on jets in neighboring bins are typically between 30% and 60% correlated. The uncertainty on all jets becomes significantly correlated at high energies and larger pseudora-

Abbrev.	Description	$\Delta$ (%)	$\sigma$ (%)
In situ $E/p$	The comparison of $\langle E/p \rangle_{\text{COR}}$ as described in Chapter 8 with statistical uncertainties from 500 MeV to 20 GeV.	0-3	1-5
CTB	The main $\langle E/p \rangle$ comparison uncertainties, binned in $p$ and $ \eta $ , as derived from the combined test beam results, from 20 to 350 GeV [32].	0-3	1-5
$E/p$ Zero Fraction	The difference in the zero-fraction between data and MC simulation from 500 MeV to 20 GeV.	5-25	1-5
$E/p$ Threshold	The uncertainty in the EM calorimeter response from the potential mismodeling of threshold effects in topological clustering.	0	0-10
Neutral	The uncertainty in the calorimeter response to neutral hadrons based on studies of physics model variations.	0	5-10
$K_L$	An additional uncertainty in the response to neutral $K_L$ in the calorimeter based on studies of physics model variations.	0	20
$E/p$ Misalignment	The uncertainty in the $p$ measurement from misalignment of the ID.	0	1
Hadrons, $p > 350$ GeV	A flat uncertainty for all particles above the energy range or outside the longitudinal range probed with the combined test beam.	0	10

Table 1: The dominant sources of corrections and systematic uncertainties in the [JES](#) estimation technique, including typical values for the correcting shift ( $\Delta$ ) and the associated uncertainty ( $\sigma$ ).

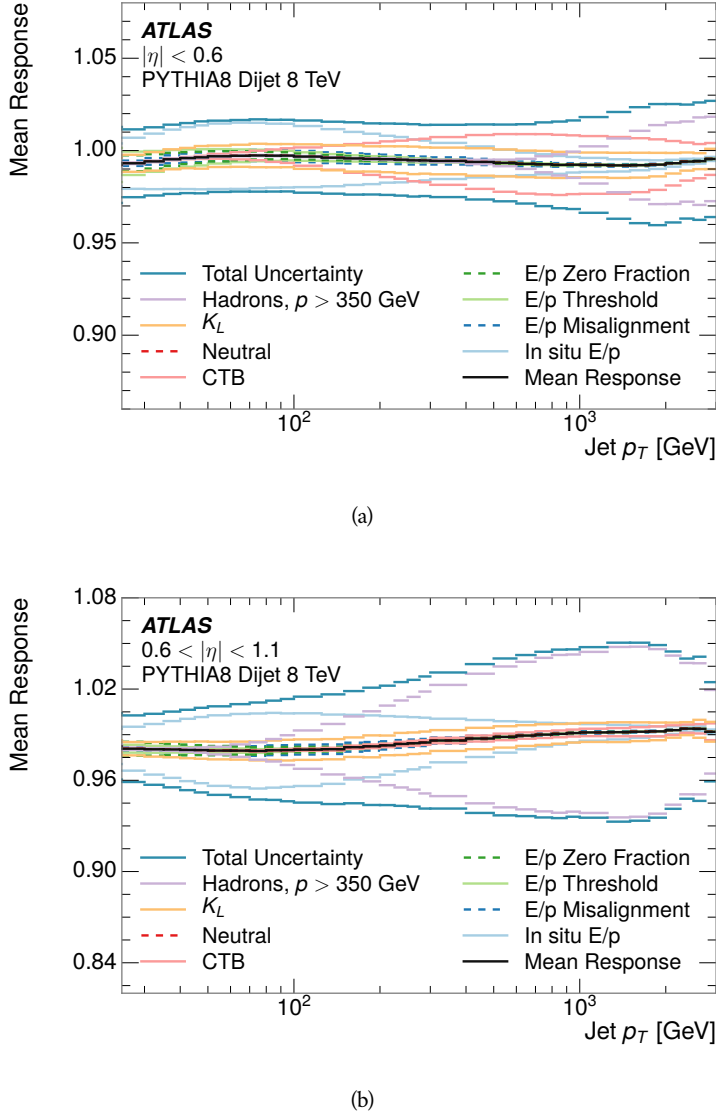


Figure 20: The [JES](#) uncertainty contributions, as well as the total [JES](#) uncertainty, as a function of jet  $p_T$  for (a)  $|\eta| < 0.6$  and (b)  $0.6 < |\eta| < 1.1$ .

874      pidities, when the uncertainty becomes dominated by the single term reflecting  
 875      out of range particles.

### 876      9.3 SUMMARY

877      The technique described above provides a jet energy scale and uncertainty by  
 878      building up jet corrections from the energy deposits of constituent particles. The  
 879       $E/p$  measurements are crucial in providing corrections for the majority of parti-  
 880      cles in the jets. The uncertainty derived this way is between 2 and 5% and is about  
 881      twice as large at corresponding momentum than jet balance methods. However  
 882      this is the only uncertainty available for very energetic jets using 2012 data and  
 883      simulation, and repeating this method with Run 2 data and simulation will be

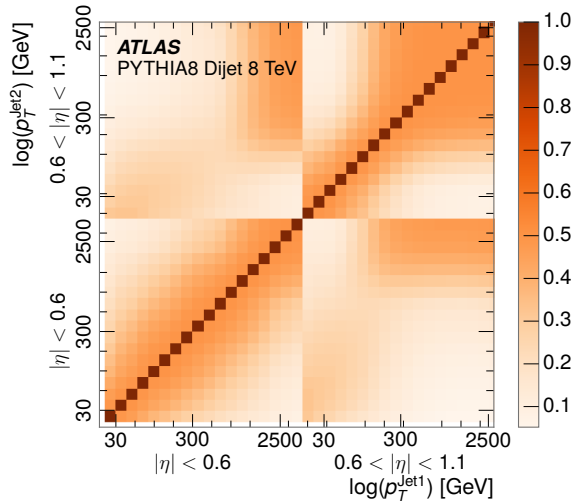


Figure 21: The JES correlations as a function of jet  $p_T$  and  $|\eta|$  for jets in the central region of the detector.

884 important in providing an uncertainty for the most energetic jets in 13 TeV col-  
 885 lisions.



886

## PART V

887

### SEARCH FOR LONG-LIVED PARTICLES

888

You can put some informational part preamble text here.



890 LONG-LIVED PARTICLES IN ATLAS

---

891 As discussed in Section 2.3, various limitations in the SM suggest a need for new  
 892 particles at the TeV scale. A wide range of extensions to the Standard Model  
 893 predict that these new particles can have lifetimes greater than approximately  
 894 one-hundredth of a nanosecond. These include theories with universal extra-  
 895 dimensions [34, 35], with new fermions [36], and with leptoquarks [37]. Many  
 896 Supersymmetry (SUSY) theories also produce these Long-Lived Particles (LLPs),  
 897 in both R-Parity violating [38–40] and R-Parity conserving [41–44] formula-  
 898 tions. Split supersymmetry [45, 46], for example, predicts long-lived gluinos  
 899 with  $O(\text{TeV})$  masses. This search focuses specifically on the SUSY case, but many  
 900 of the results are generic to any model with LLPs.

901 Long-lived gluinos or squarks carry color-charge and will thus hadronize into  
 902 color neutral bound states called R-Hadrons. These are composit particles like  
 903 the usual hadrons but with one supersymmetric constituent, for example  $\tilde{g}q\bar{q}$   
 904 and  $\tilde{q}\bar{q}$ . Through this hadronization process, the neutral gluino can acquire a  
 905 charge. Gluino pair production,  $pp \rightarrow \tilde{g}\tilde{g}$  has the largest cross sectional increase  
 906 with the increase in energy to 13 TeV, and so this search focuses on gluino R-  
 907 Hadrons. Planned future updates will extend the case to explicitly include squark  
 908 and chargino models, but the method covers any long-lived, charged, massive  
 909 particle.

## 910 10.1 EVENT TOPOLOGY

911 The majority of SUSY models predict that gluinos will be produced in pairs at  
 912 the LHC, through processes like  $pp \rightarrow q\bar{q} \rightarrow \tilde{g}\tilde{g}$  and  $pp \rightarrow gg \rightarrow \tilde{g}\tilde{g}$ , where the  
 913 gluon mode dominates for the collision energy and gluino masses considered  
 914 for this search. During their production, the long-lived gluinos hadronize into  
 915 color singlet bound states including  $\tilde{g}q\bar{q}$ ,  $\tilde{g}qqq$ , and even  $\tilde{g}g$  [47]. The probability  
 916 to form the gluon-only bound states is a free parameter usually taken to be 0.1,  
 917 while the meson states are favored among the R-Hadrons [48]. The charged and  
 918 neutral states are approximately equally likely for mesons, so the R-Hadrons will  
 919 be charged roughly 50% of the time.

920 These channels produce R-Hadrons with large  $p_T$ , comparable to their mass,  
 921 so that they typically propagate with  $0.2 < \beta < 0.9$  [48]. The fragmentation that  
 922 produces that hadrons is very hard, so the jet structure around the R-Hadron  
 923 is minimal, with less than 5 GeV of summed particle momentum expected in a  
 924 cone of  $\Delta R < 0.25$  around the R-Hadron [48]. After hadronization, depending  
 925 on the gluino lifetime, the R-Hadrons then decay into hadrons and a LSP [47].

926 In summary, the expected event for pair-produced long-lived gluinos is very  
 927 simple: two isolated, high-momentum R-Hadrons that propagate through the  
 928 detector before decaying into jets. The observable features of such events depend

929 strongly on the interaction of the R-Hadron with the material of the detector and  
 930 also its lifetime. Section 10.1.1 describes the interactions of R-Hadrons which  
 931 reach the various detector elements in A Toroidal LHC ApparatuS ([ATLAS](#)) and  
 932 Section 10.1.2 provides a summary of the observable event descriptions for R-  
 933 Hadrons of various lifetimes.

934 10.1.1 DETECTOR INTERACTIONS

935 After approximately 0.2 ns, the R-Hadron reaches the pixel detector. If charged,  
 936 it deposits energy into the material through repeated single collisions that result  
 937 in ionization of the silicon substrate [49]. Because of its comparatively low  $\beta$ ,  
 938 the ionization energy can be significantly greater than expected for [SM](#) particles  
 939 because the most-probable energy loss grows significantly as  $\beta$  decreases [49].  
 940 This large ionization can be measured through the time over threshold ([ToT](#)) read  
 941 out from the pixel detector as described in Section 7.1.1.2. Large ionization in  
 942 the inner detector is one of the major characteristic features of [LLPs](#).

943 Throughout the next few nanoseconds, the R-Hadron propagates through the  
 944 remainder of the inner detector. A charged R-Hadron will provide hits in each  
 945 of these systems as would any other charged particle, and can be reconstructed  
 946 as a track. The track reconstruction provides a measurement of its trajectory  
 947 and thus its momentum as described in Section 7.1. The large momentum is  
 948 another characteristic feature of massive particles produced at the [LHC](#). **Note: At**  
 949 **this point I am failing to mention that the TRT provides a possible  $dE/dx$**   
 950 **measurement, because no one uses it as far as I know.**

951 As of roughly 20 ns, the R-Hadron enters the calorimeter where it interacts  
 952 hadronically with the material. Because of its large mass and momentum, the  
 953 R-Hadron does not typically stop in the calorimeter, but rather deposits a small  
 954 fraction of its energy through repeated interactions with nucleons. The proba-  
 955 bility of interaction between the gluino itself and a nucleon is low because the  
 956 cross section drops off with the inverse square of its mass, so the interactions are  
 957 primarily governed by the light constituents [50]. Each of these interactions can  
 958 potentially change that quark content and thus change the sign of the R-Hadron,  
 959 so that the charge at exit is typically uncorrelated with the charge at entry [48].  
 960 The total energy deposited in the calorimeters during the propagation is small  
 961 compared to the kinetic energy of the R-Hadron, around 20-40 GeV, so that  
 962  $E/p$  is typically less than 0.1 [48].

963 Then, 30 ns after the collision, it reaches the muon system, where it again  
 964 ionizes in the material if charged and can be reconstructed as a muon track. Be-  
 965 cause of the charge-flipping interactions in the calorimeter, this track may have  
 966 the opposite sign of the track reconstructed in the inner detector, or there may  
 967 be a track present when there was none in the inner detector and vice-versa. The  
 968 propagation time at the typically lower  $\beta$  results in a significant delay compared  
 969 to muons, and that delay can be assessed in terms of a time-of-flight measure-  
 970 ment. Because of the probability of charge-flip and late arrival, there is a signif-  
 971 icant chance that an R-Hadron which was produced with a charge will not be

972 identified as a muon. The long time-of-flight is another characteristic feature of  
 973 R-Hadrons which are reconstructed as muons.

974 10.1.2 LIFETIME DEPENDENCE

975 The above description assumed a lifetime long enough for the R-Hadron to exit  
 976 the detector, which through this search is referred to as “stable”, even though  
 977 the particle may decay after exiting the detector. There are several unique sig-  
 978 natures at shorter lifetimes where the R-Hadron decays in various parts of the  
 979 inner detector; these lifetimes are referred to as “metastable”.

980 The shortest case where the R-Hadron is considered metastable is for life-  
 981 times around 0.01 ns, where the particle decays before reaching any of the de-  
 982 tector elements. Although the R-Hadrons are produced opposite each other in  
 983 the transverse plane, each R-Hadron decays to a jet and an [LSP](#). The [LSPs](#) are not  
 984 measured, so the produced jets can be significantly imbalanced in the transverse  
 985 plane which results in large missing energy. That missing energy can be used  
 986 to trigger candidate events, and provides the most efficient trigger option for  
 987 shorter lifetimes. Additionally, the precision of the tracking system allows the  
 988 displaced vertex of the R-Hadron decay to be reconstructed from the charged  
 989 particles in the jet. The distance of that vertex from the interaction point can  
 990 be used to distinguish R-Hadron decays from other processes. Figure 22 shows  
 991 a schematic diagram of an example R-Hadron event with such a lifetime. The  
 992 diagram is not to scale, but instead illustrates the detector interactions in the  
 993 pixel detector, calorimeters, and muon system. It includes a representation of  
 994 the charged R-Hadron and the neutral R-Hadron, as well as the [LSPs](#) and jets  
 995 (shown as charged hadrons) produced in the decay. Neutral hadrons may also  
 996 be produced in the decay but are not depicted. Previous searches on [ATLAS](#) have  
 997 used the displaced vertex to target [LLP](#) decays [51].

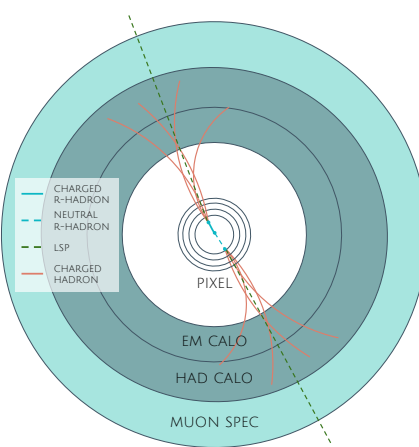


Figure 22: A schematic diagram of an R-Hadron event with a lifetime around 0.01 ns.  
 The diagram includes one charged R-Hadron (solid blue), one neutral R-  
 Hadron (dashed blue), [LSPs](#) (dashed green) and charged hadrons (solid orange).  
 The pixel detector, calorimeters, and muon system are illustrated but not to  
 scale.

998     The next distinguishable case occurs at lifetimes greater than 0.1 ns, where  
 999    the R-Hadron forms a partial track in the inner detector. If the decay products  
 1000   are sufficiently soft, they may not be reconstructed, and this forms a unique sig-  
 1001   nature of a disappearing track. An example of such an event is illustrated in  
 1002   Figure 23, which shows the short track in the inner detector and the undetected  
 1003   soft charged hadron and LSP that are produced. A dedicated search on ATLAS used  
 1004   the disappearing track signature to search for LLP in Run 1 [52]. **zNote: might**  
 1005   **not be worth mentioning the disappearing track here since it is actually a**  
 1006   **chargino search, the soft pion is pretty unique to charginos.**

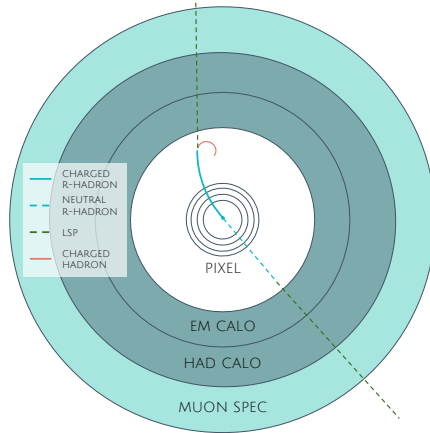


Figure 23: A schematic diagram of an R-Hadron event with a lifetime around 4 ns. The diagram includes one charged R-Hadron (solid blue), one neutral R-Hadron (dashed blue), LSPs (dashed green) and a charged hadron (solid orange). The pixel detector, calorimeters, and muon system are illustrated but not to scale.

1007    If the decay products are not soft, the R-Hadron daughters form jets, resulting  
 1008   in an event-level signature of up to two high-momentum tracks, jets, and signif-  
 1009   icant missing energy. The missing energy has the same origin as in the case of  
 1010   0.01 ns lifetimes, from the decay to unmeasured particles, and again can be large.  
 1011   The high-momentum tracks will also have the characteristically high-ionization  
 1012   of massive, long-lived particles in the inner detector. Figure 24 illustrates an ex-  
 1013   ample event with one charged R-Hadron which decays after approximately 10 ns,  
 1014   and shows how the jets from the decay can still be reconstructed in the calorime-  
 1015   ter. Several previous searches on ATLAS from Run 1 have used this signature to  
 1016   search for R-Hadrons [53, 54], including a dedicated search for metastable parti-  
 1017   cles [55].

1018    If the lifetime is longer than several nanoseconds, in the range of 15-30 ns,  
 1019   the R-Hadron decay can occur in or after the calorimeters, but prior to reaching  
 1020   the muon system. This case is similar to the above, although the jets may not be  
 1021   reconstructed, and is covered by many of the same search strategies. The events  
 1022   still often have large missing energy, although it is generated through different  
 1023   mechanisms. The R-Hadrons do not deposit much energy in the calorimeters, so  
 1024   a neutral R-Hadron will not enter into the missing energy calculation. A charged  
 1025   R-Hadron opposite a neutral R-Hadron will thus generate significant missing en-  
 1026   ergy, and close to 50% of pair-produced R-Hadron events fall into this category.

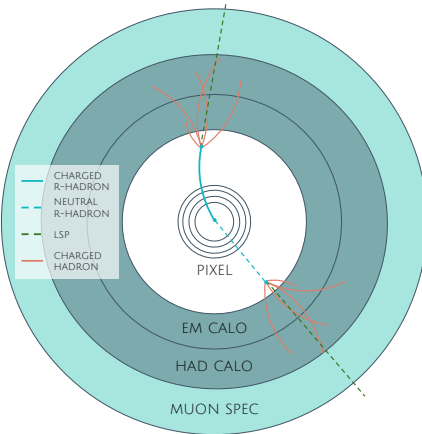


Figure 24: A schematic diagram of an R-Hadron event with a lifetime around 5 ns. The diagram includes one charged R-Hadron (solid blue), one neutral R-Hadron (dashed blue), LSPs (dashed green) and charged hadrons (solid orange). The pixel detector, calorimeters, and muon system are illustrated but not to scale.

1027 If both R-Hadrons are neutral then the missing energy will be low because nei-  
 1028 ther is detected. Two charged R-Hadrons will also result in low missing energy  
 1029 because both are reconstructed as tracks and will balance each other in the trans-  
 1030 verse plane. A small fraction of the time, one of the charged R-Hadron tracks may  
 1031 fail quality requirements and thus be excluded from the missing energy calcula-  
 1032 tion and again result in significant missing energy. Figure 25 illustrates another  
 1033 example event with one charged R-Hadron which decays after approximately 20  
 1034 ns, and shows how the jets from the decay might not be reconstructed.

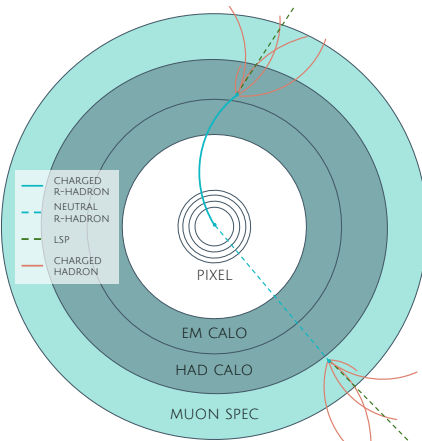


Figure 25: A schematic diagram of an R-Hadron event with a lifetime around 20 ns. The diagram includes one charged R-Hadron (solid blue), one neutral R-Hadron (dashed blue), LSPs (dashed green) and charged hadrons (solid orange). The pixel detector, calorimeters, and muon system are illustrated but not to scale.

1035 The longest lifetimes, the stable case, has all of the features of the 30-50 ns case  
 1036 but with the addition of muon tracks for any R-Hadrons that exit the calorimeter  
 1037 with a charge. That muon track can provide additional information from time-  
 1038 of-flight measurements to help identify LLPs. An example of the event topology

1039 for one charged and one neutral stable R-Hadron is shown in Figure 26. Some  
 1040 searches on [ATLAS](#) have included this information to improve the search reach  
 1041 for stable particles [54, 56].

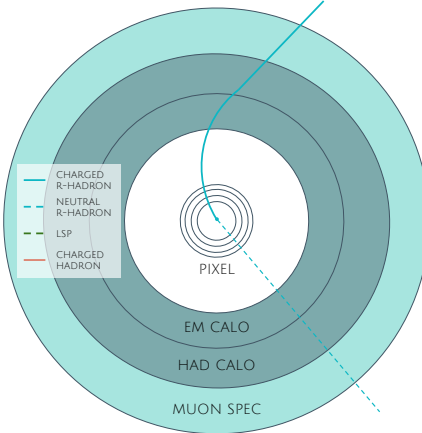


Figure 26: A schematic diagram of an R-Hadron event with a lifetime around 20 ns. The diagram includes one charged R-Hadron (solid blue) and one neutral R-Hadron (dashed blue). The pixel detector, calorimeters, and muon system are illustrated but not to scale.

## 1042 10.2 SIMULATION

1043 All of the event topologies discussed above are explored by simulations of R-  
 1044 Hadron events in the [ATLAS](#) detector. A large number of such samples are gen-  
 1045 erated to determine signal efficiencies, to measure expected yields, and to esti-  
 1046 mate uncertainties. The primary interaction, pair production of gluinos with  
 1047 masses between 400 and 3000 GeV, is simulated using [Pythia 6.4.27](#) [57]  
 1048 with the AUET2B [58] set of tuned parameters for the underlying event and  
 1049 the CTEQ6L1 [31] parton distribution function (PDF) set. The simulated inter-  
 1050 actions include a modeling of pileup by adding secondary, minimum bias in-  
 1051 teractions from both the same (in-time pileup) and nearby (out-of-time pileup)  
 1052 bunch crossings. This event generation is then augmented with a dedicated  
 1053 hadronization routine to hadronize the long-lived gluinos into final states with  
 1054 R-Hadrons [59], with the probability to form a gluon-gluino bound set at 10% [60].

1055 The cross sections used for these processes are calculated at next-to-leading  
 1056 order (NLO) in the strong coupling constant with a resummation of soft-gluon  
 1057 emmission at next-to-leading logarithmic (NLL) [61–65]. The nominal predic-  
 1058 tions and the uncertainties for each mass point are taken from an envelope of  
 1059 cross-section predictions using different PDF sets and factorization and renor-  
 1060 malization scales [66].

1061 The R-Hadrons then undergo a full detector simulation [], where the interac-  
 1062 tions of the R-Hadrons with the material of the detector are described by dedi-  
 1063 cated [Geant4](#) [1] routines. These routines model the interactions described in  
 1064 Section 10.1.1, including the ionizing interactions in the silicon modules of the  
 1065 inner detector and the R-Hadron-nucleon interactions in the calorimeters [67],

1066 [68]. The specific routine chosen to describe the interactions of the R-Hadrons  
 1067 with nucleons, the “generic model”, uses a pragmatic approach where the scatter-  
 1068 ing cross section is taken to be a constant 12 mb per light quark. In this model  
 1069 the gluino itself does not interact at all except through its role as a reservoir of  
 1070 kinetic energy.

1071 The lifetimes of these R-Hadrons are then simulated at several working points,  
 1072  $\tau = 0.1, 1.0, 3.0, 10, 30, 50$  and detector stable, where the particle is required to  
 1073 decay after propagating for a time compatible with its lifetime. Only one decay  
 1074 mode is simulated for these samples,  $\tilde{g} \rightarrow q\bar{q}\tilde{\chi}_1^0$  with the neutralino mass set to  
 1075 100 GeV, which is chosen because it has the highest sensitivity among all of the  
 1076 modes studied in previous searches [55]. Heavier neutralinos have similar results  
 1077 but generate less missing energy which reduces the efficiency of triggering.

1078 All of the simulated events are then reconstructed using the same software  
 1079 used for collision data. The fully reconstructed events are then reweighted to  
 1080 match the distribution of initial state radiation in an alternative sample of events,  
 1081 generated with MG5\_aMC@NLO [69], which has a more accurate description of ra-  
 1082 diate effects than Pythia6. This reweighting provides a more accurate descrip-  
 1083 tion of the momentum of the gluino-gluino system and is important in modeling  
 1084 the efficiency of triggering and offline event selection.



1085

1086 EVENT SELECTION

---

1087 The [LLPs](#) targeted by this search differ in their interactions with the detector from  
 1088 [SM](#) particles primarily because of their large mass. When produced at the ener-  
 1089 gies available at the [LHC](#), that large mass results in a low  $\beta$  (typically  $0.2 < \beta <$   
 1090 0.9). Such slow-moving particles heavily ionize in detector material. Each layer  
 1091 of the pixel detector provides a measurement of that ionization, through [ToT](#), as  
 1092 discussed in Section 6.3.1. The ionization in the pixel detector, quantified in  
 1093 terms of  $dE/dx$ , provides the major focus for this search technique, along with  
 1094 the momentum measured in the entire inner detector. It is effective both for its  
 1095 discriminating power and its use in reconstructing a particle’s mass, and it can  
 1096 be used for a wide range of masses and lifetimes as discussed in Section 10.1.2.  
 1097 However  $dE/dx$  needs to be augmented with a few additional selection require-  
 1098 ments to provide a mechanism for triggering and to further reduce backgrounds.

1099 Ionization itself is not currently accessible for triggering, so this search in-  
 1100 stead relies on  $E_T^{\text{miss}}$  to trigger signal events. Although triggering on  $E_T^{\text{miss}}$  can  
 1101 be inefficient,  $E_T^{\text{miss}}$  is often large for many production mechanisms of [LLPs](#), as  
 1102 discussed in Section 10.1.

1103 The use of ionization to reject [SM](#) backgrounds relies on well-measured, high-  
 1104 momentum tracks, so some basic requirements on quality and kinematics are  
 1105 placed on the tracks considered in this search. These quality requirements have  
 1106 been significantly enhanced in Run 2 by a newly introduced tracking variable  
 1107 that is very effective in removing highly-ionizing backgrounds caused by over-  
 1108 lapping tracks. A few additional requirements are placed on the tracks consid-  
 1109 ered for [LLP](#) candidates that increase background rejection by targeting specific  
 1110 types of [SM](#) particles. These techniques provide a significant analysis improve-  
 1111 ment over previous iterations of ionization-based searches on ATLAS by provid-  
 1112 ing additional background rejection with minimal loss in signal efficiency.

1113 The ionization measurement with the Pixel detector can be calibrated to pro-  
 1114 vide an estimator of  $\beta\gamma$ . That estimate, together with the momentum measure-  
 1115 ment provided by tracking, can be used to reconstruct a mass for each track  
 1116 which traverses the pixel detector. That mass variable will be peaked at the [LLP](#)  
 1117 mass for any signal, and provides an additional tool to search for an excess. In  
 1118 addition to an explicit requirement on ionization, this search constructs a mass-  
 1119 window for each targeted signal mass in order to evaluate any excess of events  
 1120 and to set limits.

1121 The strategy discussed here is optimized for lifetimes of  $O(1) - O(10)$  ns.  
 1122 Pixel ionization is especially useful in this regime as particles only need to prop-  
 1123 agate through the first seven layers of the inner detector, about 37 cm from the  
 1124 beam axis. The search is still competitive with other searches for [LLPs](#) at longer  
 1125 lifetimes, because the primary discriminating variables are still applicable even  
 1126 for particles that do not decay within the detector [56]. Although the majority of

1127 the requirements will be the same for all lifetimes, two signal regions are defined  
 1128 to optimize separately for intermediate and long lifetime particles.

## 1129 11.1 TRIGGER

1130 Triggering remains a significant difficulty in defining an event selection with  
 1131 high signal efficiency in a search for LLPs. There are no triggers available in  
 1132 the current ATLAS system that can fire directly from a high momentum track  
 1133 with large ionization (Section 6.6). Although in some configurations a charged  
 1134 LLP can fire muon triggers, this requirement introduces significant model depen-  
 1135 dence on both the allowed lifetimes and the interactions in the calorimeter [48],  
 1136 as discussed in Section 10.1.1.

1137 For a search targeting particles which may decay prior to reaching the muon  
 1138 system, the most efficient available trigger is based on missing energy [48]. As  
 1139 discussed in Section 10.1, signal events can produce significant  $E_T^{\text{miss}}$  by a few  
 1140 mechanisms. At the trigger level however, the missing energy is only calculated  
 1141 using the calorimeters (Section 6.6) where the R-Hadrons deposit little energy.  
 1142 So, at short lifetimes,  $E_T^{\text{miss}}$  measured in the calorimeter is generated by an im-  
 1143 balance between the jets and undetected LSPs produced in R-Hadron decays. At  
 1144 longer lifetimes, without the decay products, missing energy is only produced in  
 1145 the calorimeters when the R-Hadrons recoil against an initial state radiation (ISR)  
 1146 jet.

1147 These features are highlighted in Figure 27, which shows the  $E_T^{\text{miss}}$  distribu-  
 1148 tions for simulated short lifetime (3 ns) and stable R-Hadron events. The figure  
 1149 includes both the offline  $E_T^{\text{miss}}$ , the missing energy calculated with all available  
 1150 information, and Calorimeter  $E_T^{\text{miss}}$ , the missing energy calculated using only  
 1151 information available at the calorimeter which approximates the missing energy  
 1152 available at the trigger. The short lifetime sample has significantly greater  $E_T^{\text{miss}}$   
 1153 and Calorimeter  $E_T^{\text{miss}}$  than the stable sample as expected. For the stable sam-  
 1154 ple, a small fraction of events with very large  $E_T^{\text{miss}}$  (about 5%) migrate into the  
 1155 bin with very small Calorimeter  $E_T^{\text{miss}}$  because the  $E_T^{\text{miss}}$  produced by a charged  
 1156 R-Hadron track opposite a neutral R-Hadron track does not contribute any miss-  
 1157 ing energy in the calorimeters.

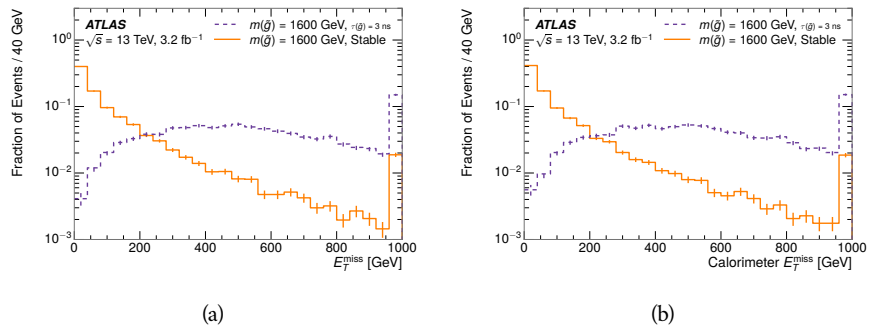


Figure 27: The distribution of (a)  $E_T^{\text{miss}}$  and (b) Calorimeter  $E_T^{\text{miss}}$  for simulated signal events before the trigger requirement.

1158 So, either case to some extent relies on kinematic degrees of freedom to pro-  
 1159 duce missing energy, as the pair-produced LLPs tend to balance each other in  
 1160 the transverse plain. That balance results in a relatively low efficiency for long-  
 1161 lifetime particles, roughly 40%, and efficiencies between 65% and 95% for shorter  
 1162 lifetimes depending on both the mass and the lifetime. For long lifetimes in par-  
 1163 ticular, the presence of ISR is important in providing an imbalance in the trans-  
 1164 verse plane, and is an important aspect of modeling the selection efficiency for  
 1165 R-Hadron events.

1166 The missing energy trigger with the lowest threshold available is chosen for  
 1167 this selection in order to maximize the trigger efficiency. During 2015 data col-  
 1168 lection this was the HLT\_xe70 trigger, which used a 50 GeV threshold on miss-  
 1169 ing energy at LVL1 and a 70 GeV threshold on missing energy at the HLT. These  
 1170 formation of the trigger decision for missing energy was discussed in more detail  
 1171 in Section 6.6.

## 1172 11.2 KINEMATICS AND ISOLATION

1173 After the trigger requirement, each event is required to have a primary vertex  
 1174 reconstructed from at least two well-measured tracks in the inner detector, each  
 1175 with  $p_T > 400$  MeV. If more than one such vertex exists, the primary vertex  
 1176 is taken to be the one with the largest summed track momentum for all tracks  
 1177 associated to that vertex. The offline reconstructed  $E_T^{\text{miss}}$  is required to be above  
 1178 130 GeV to additionally reject SM backgrounds. The transverse missing energy  
 1179 is calculated using fully reconstructed and calibrated offline objects, as described  
 1180 in Section 7.5. In particular the  $E_T^{\text{miss}}$  definition in this selection uses jets recon-  
 1181 structed with the anti- $k_t$  algorithm with radius  $R = 0.4$  from clusters of energy  
 1182 in the calorimeter (Section 7.2) and with  $p_T > 20$  GeV, as well as reconstructed  
 1183 muons, electrons, and tracks not identified as another object type.

1184 The  $E_T^{\text{miss}}$  distributions are shown for data and a few simulated signals in Fig-  
 1185 ure 28, after the trigger requirement. The cut placed at 130 GeV is 95% effi-  
 1186 cient for metastable and 90% efficient for stable particles, after the trigger re-  
 1187 quirement, because of the missing energy generating mechanisms discussed pre-  
 1188 viously. The distribution of data in this figure and subsequent figures in this sec-  
 1189 tion can be interpreted as the distribution of backgrounds, as any signal contam-  
 1190 ination would be negligible if present at these early stages of the selection (prior  
 1191 to the final requirement on ionization). The background falls rapidly with miss-  
 1192 ing energy, motivating the direct requirement on  $E_T^{\text{miss}}$  for the signal region. Al-  
 1193 though a tighter requirement than the specified value of 130 GeV would seem to  
 1194 increase the search potential from these early distributions, other requirements  
 1195 are more optimal when taken as a whole. The specific values for each require-  
 1196 ment in signal region were optimized considering the increase in discovery reach  
 1197 for tightening the requirement on each discriminating variable. **NOTE: If space**  
 1198 **and time permit, I will add a whole section about signal region optimiza-**  
 1199 **tion..**

1200 It is typically the practice for searches for new physics on ATLAS to place an  
 1201 offline requirement on the triggering variable that is sufficiently tight to guar-

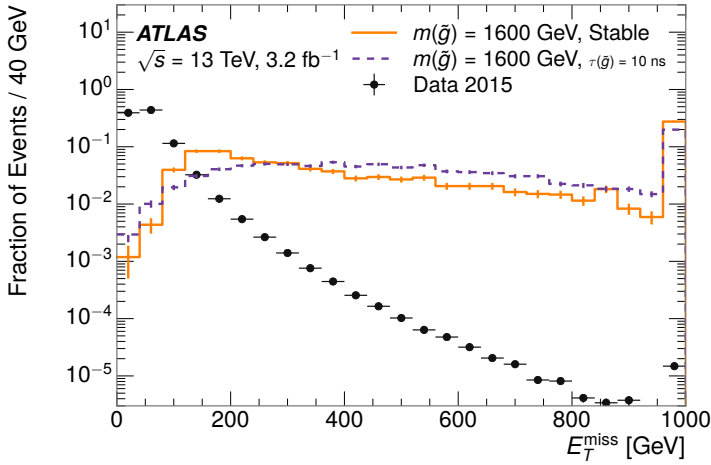


Figure 28: The distribution of  $E_T^{\text{miss}}$  for data and simulated signal events, after the trigger requirement.

ante that the event would pass the trigger. Such a tight requirement makes the uncertainty on the trigger efficiency of the simulation negligible, as modeling the regime where the trigger is only partially efficient can be difficult. In this analysis, however, because of the atypical interactions of R-Hadrons with the tracker and the calorimeter, the offline requirement on  $E_T^{\text{miss}}$  is not sufficient to guarantee a 100% trigger efficiency even at large values, as can be seen in Figure 29. This figure shows the efficiency for passing the HLT\_xe70 trigger as a function of the requirement on  $E_T^{\text{miss}}$ , which plateaus to roughly 85% even at large values. This plateau does not reach 100% because events which have large offline missing energy from a neutral R-Hadron produced opposite of a charged R-Hadron can have low missing energy in the calorimeters. The Calorimeter  $E_T^{\text{miss}}$ , on the other hand, does not have this effect and reaches 100% efficiency at large values because it is the quantity that directly corresponds to the trigger threshold. In both cases the efficiency of triggering is greater for the short lifetime sample because the late decays to hadrons and LSPs produce an imbalance in the calorimeters even though they may not be reconstructed offline as tracks or jets. For this reason, the requirement on  $E_T^{\text{miss}}$  is determined by optimizing the background rejection even though it corresponds to a value of trigger efficiency significantly below 1.0.

Potential signal events are then required to have at least one candidate LLP track. Although the LLPs are produced in pairs, many models do not consistently yield two charged particles. For example, in the R-Hadron model highlighted here, only 20% of events have two charged R-Hadrons while 47% of events have just one. A signal region requiring two charged candidates could be a powerful improvement in background rejection for a larger dataset, but it is not considered in this version of the analysis as it was found to be unnecessary to reject the majority of backgrounds.

For a track to be selected as a candidate, it must have  $p_T > 50 \text{ GeV}$  and pass basic quality requirements. The track must be associated to the primary vertex.

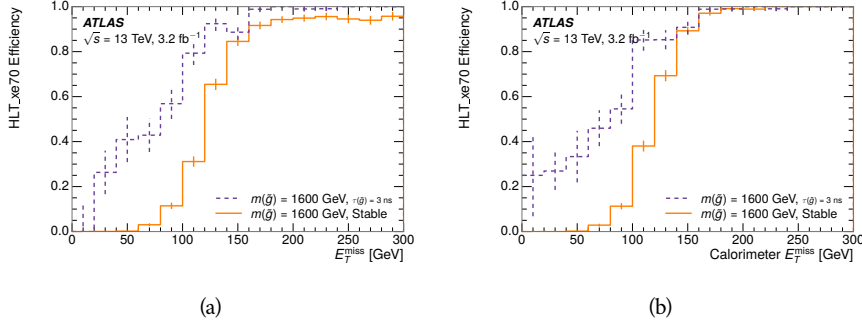


Figure 29: The trigger efficiency for the HLT\_xe70 trigger requirement as a function of (a)  $E_T^{\text{miss}}$  and (b) Calorimeter  $E_T^{\text{miss}}$  for simulated signal events.

It must also have at least seven clusters in the silicon layers in the inner detector to ensure an accurate measurement of momentum. Those clusters must include one in the innermost layer if the extrapolated track is expected to pass through that layer. And to ensure a reliable measurement of ionization, the track is required to have at least two clusters in the pixel detector that provide a measurement of  $dE/dx$ .

At this point in the selection, there is a significant high-ionization background from multiple tracks that significantly overlap in the inner detector. Previous version of this analysis have rejected these overlaps by an explicit overlap rejection between pairs of fully reconstructed tracks, typically by requiring no additional tracks within a cone around the candidate. This technique, however, fails to remove the background from tracks that overlap so precisely that the tracks cannot be separately resolved, which can be produced in very collimated photon conversions or decays of pions.

A new method, added in Run 2, identifies cluster shapes that are likely formed by multiple particles based on a neural network classification algorithm. The number of clusters that are classified this way in the pixel detector for a given track is called  $N_{\text{split}}$ . As the shape of clusters requires significantly less spatial separation to identify overlaps than it does to reconstruct two fully resolved tracks, this variable is more effective at rejecting backgrounds from overlaps. Figure 30 shows the dependence of ionization on  $N_{\text{split}}$ ; as  $N_{\text{split}}$  increases the most probable value of  $dE/dx$  grows significantly up to twice the expected value when  $N_{\text{split}} = 4$ .

This requirement is very successful in reducing the long positive tail of the  $dE/dx$  distributions, as can be seen in Figure 31. Comparing the distribution for “baseline tracks”, tracks with only the above requirements on clusters applied and before the requirement on  $N_{\text{split}}$ , to the distribution with  $N_{\text{split}} = 0$ , it is clear that the fraction of tracks with large  $dE/dx$  is reduced by several orders of magnitude. The tracks without split hits are very close to the  $dE/dx$  distribution of identified muons, which are extremely well isolated on average. Figure 31 also includes the distribution of  $dE/dx$  in an example signal simulation to demonstrate how effective  $dE/dx$  is as a discriminating variable with this isolation applied. The background falls rapidly for  $dE/dx > 1.8 \text{ MeVg}^{-1}\text{cm}^2$

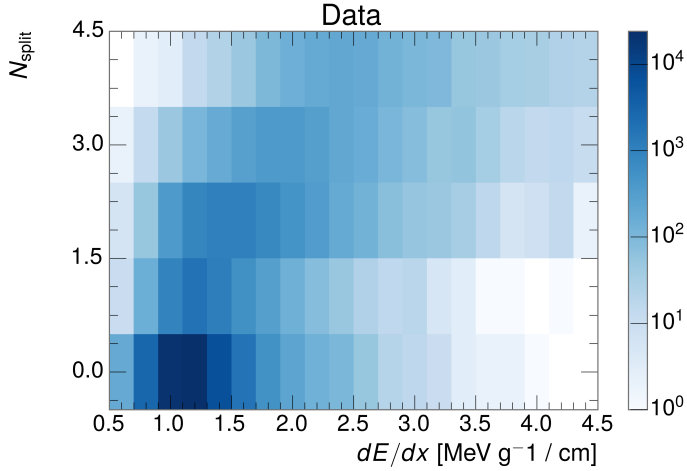


Figure 30: The dependence of  $dE/dx$  on  $N_{\text{split}}$  in data after basic track hit requirements have been applied.

1264 while the majority of the signal, approximately 90% depending on the mass, falls  
 1265 above that threshold. Over 90% of [LLP](#) tracks in simulated signal events pass the  
 1266  $N_{\text{split}}$ -based isolation requirement.

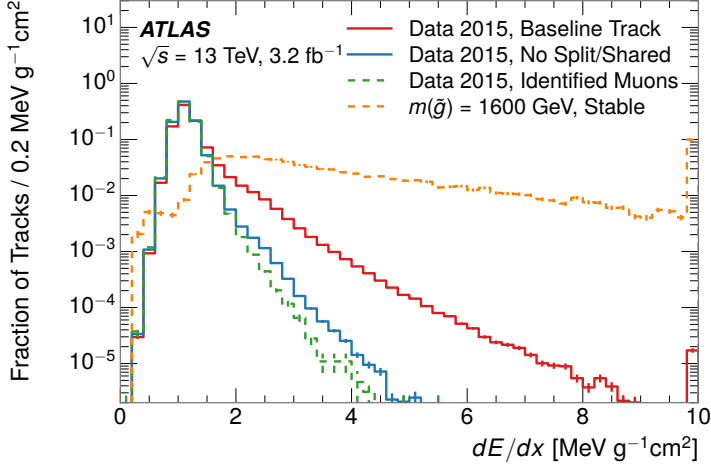


Figure 31: The distribution of  $dE/dx$  with various selections applied in data and simulated signal events.

1267 A few additional kinematic requirements are imposed to help reduce [SM](#) back-  
 1268 grounds. The momentum of the candidate track must be at least 150 GeV, and  
 1269 the uncertainty on that measurement must be less than 50%. The distribution of  
 1270 momentum is shown in Figure 32 for tracks in data and simulated signal events  
 1271 after the previously discussed requirements on clusters, transverse momentum,  
 1272 and isolation have been imposed. The signal particles are much harder on aver-

age than their backgrounds because of the high energy interactions required to produce them. The transverse mass,  $M_T$ , defined as

$$M_T = \sqrt{2p_T E_T^{\text{miss}}(1 - \cos(\Delta\phi(E_T^{\text{miss}}, \text{track})))} \quad (1)$$

estimates the mass of a decay of to a single charged particle and an undetected particle and is required to be greater than 130 GeV to reject contributions from the decay of W bosons. Figure 33 shows the distribution of  $M_T$  for data and simulated signal events. The signal is distributed over a wide range of  $M_T$ , with about 90% above the threshold value of 130 GeV. The data shows a dual-peaked structure, where the first peak comes from W boson decays and the second peak is a kinematic shaping from the requirements on  $E_T^{\text{miss}}$  and the track  $p_T$  in dijet events.

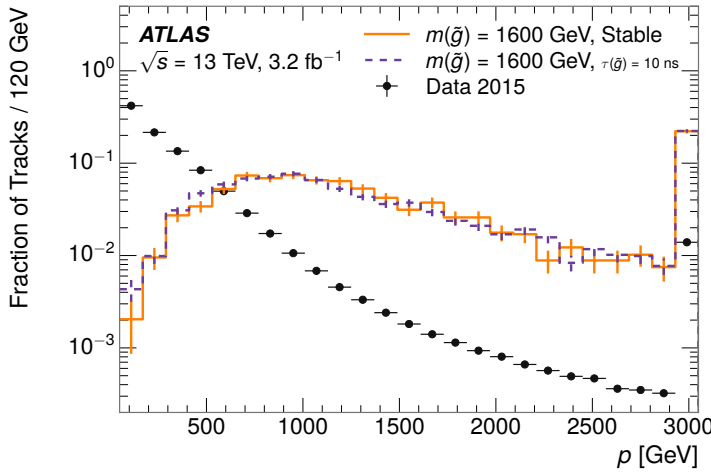


Figure 32: The distribution of track momentum for data and simulated signal events, after previous selection requirements have been applied.

### 11.3 PARTICLE SPECIES REJECTION

The amount of ionization deposited by particles with low mass and high momentum has a large positive tail [49], so backgrounds can be formed by a wide variety of SM processes when various charged particles have a few randomly large deposits of energy in the pixel detector. Those backgrounds can be additionally reduced by targeting other interactions with the detector where they are expected to have different behavior than R-Hadrons. The interactions with the detector depend on the types of particles produced rather than the processes which produce them, so this search forms a series of rejections to remove backgrounds from individual particle species. These rejections focus on using additional features of the event, other than the kinematics of the candidate track, as they can provide a powerful source of background rejection with very high signal efficiency. However, the lifetime of an R-Hadron can significantly change its

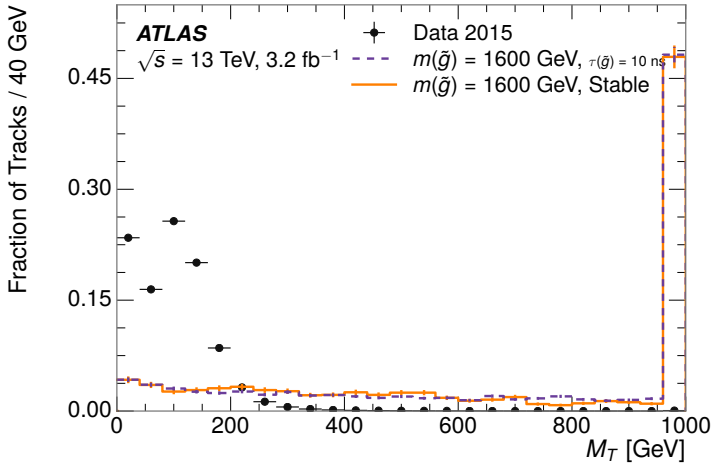


Figure 33: The distribution of  $M_T$  for data and simulated signal events, after previous selection requirements have been applied.

1296 detector characteristics, as discussed in Section 10.1.2. To accommodate these  
 1297 differences, the SM rejections defined in this section are split to form two signal  
 1298 regions, one for long-lifetimes particles, the stable region ( $50 \leq \tau[\text{ns}] < \infty$  ns),  
 1299 and one for intermediate lifetime particles, the metastable region ( $0.4 < \tau[\text{ns}] <$   
 1300 50).

1301 Jets can be very effectively rejected by considering the larger-scale isolation of  
 1302 the candidate track. In this case the isolation focuses on the production of nearby  
 1303 particles as a jet-veto, rather than the isolation from overlapping tracks based on  
 1304  $N_{\text{split}}$  that was used to reduce high-ionization backgrounds. As explained in Sec-  
 1305 tion 10.1, the fragmentation process which produces an R-Hadron is very hard  
 1306 and thus is not expected to produce additional particles with a summed momen-  
 1307 tum of more than 5 GeV. The jet-veto uses the summed momentum of tracks  
 1308 with a cone of  $\Delta R < 0.25$ , referred to as  $p_T^{\text{Cone}}$ , which is shown in Figure 34 for  
 1309 data and simulated signal events. In the data this value has a peak at zero from  
 1310 isolated tracks such as leptons, and a long tail from jets which contains as much  
 1311 as 80% of the background above 20 GeV at this stage of the selection. In signal  
 1312 events  $p_T^{\text{Cone}}$  is strongly peaked at zero and significantly less than 1% of signal  
 1313 events have  $p_T^{\text{Cone}}$  above 20 GeV. This makes a requirement of  $p_T^{\text{Cone}} < 20$  GeV  
 1314 a very effective method to reject background without losing signal efficiency.  
 1315 For the stable signal region, this cut is further tightened to  $p_T^{\text{Cone}} < 5$  GeV as  
 1316 it is the most effective variable remaining to extend the search reach for long  
 1317 lifetimes.

1318 Even for fully isolated particles, there are additional methods to reject each  
 1319 type of particle using information in the muon system and calorimeters. Muons  
 1320 can be identified very reliably using the tracks in the muon system, as described  
 1321 in Section 7.4. For intermediate lifetimes the LLPs do not survive long enough  
 1322 to reach the muon system, and so muons are vetoed by rejecting tracks that as-  
 1323 sociate to a muon with medium muon identification requirements (Section 7.4).  
 1324 For longer lifetimes, this rejection is not applied because LLPs which reach the

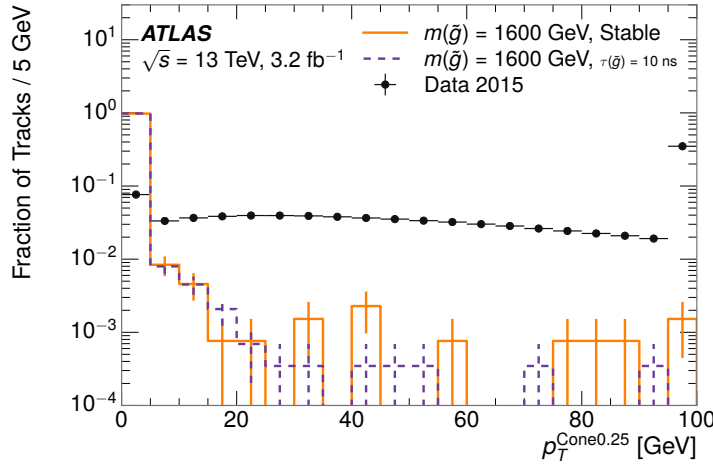


Figure 34: The distribution of summed tracked momentum within a cone of  $\Delta R < 0.25$  around the candidate track for data and simulated signal events, after previous selection requirements have been applied.

1325 muon system can be identified as muons as often as 30% of the time in simulated  
 1326 samples.

1327 Calorimeter-based particle rejection relies on the expected small deposits of  
 1328 energy from LLPs. When the lifetime is long enough to reach the calorimeter, a  
 1329 LLP deposits little of its energy as it traverses the material, as discussed in Sec-  
 1330 tion 10.1. Even when the particle does decay before the calorimeter, the major-  
 1331 ity of its energy is carried away by the LSP and not deposited in the calorimeter.  
 1332 In both cases the energy is expected to be distributed across the layers of the  
 1333 calorimeters and not peaked in just one layer. This can be quantified in terms  
 1334 of  $E/p$ , the ratio of calorimeter energy of a nearby jet to the track momentum,  
 1335 and  $f_{\text{EM}}$ , the fraction of energy in that jet within the electromagnetic calorime-  
 1336 ter. When no jets fall within a cone of 0.05 of the particle,  $E/p$  and  $f_{\text{EM}}$  are both  
 1337 defined as zero.  $E/p$  is expected to be above 1.0 for typical SM particles because  
 1338 of calibration and the contributions from other nearby particles, as discussed in  
 1339 Chapter ???. At these momenta there is no significant zero fraction due to inter-  
 1340 actions with the detector or insufficient energy deposits (see Section 8.2.2).  $f_{\text{EM}}$   
 1341 is peaked close to 1.0 for electrons, and distributed between 10% and 90% for  
 1342 hadrons.

1343 These trends can be seen in the two dimensional distribution for signal in  
 1344 Figure 35 for stable and metastable (10 ns) events. The majority of R-Hadrons  
 1345 in both samples fall into the bin for  $E/p = 0$  and  $f_{\text{EM}} = 0$  because the majority  
 1346 of the time there is no associated jet. In the stable sample, when there often is  
 1347 an associated jet,  $E/p$  is typically still below 0.1, and the  $f_{\text{EM}}$  is predominantly  
 1348 under 0.8. In the metastable sample, on the other hand,  $E/p$  is larger but still  
 1349 typically below 0.1 because of actual jets produced during the decay. The  $f_{\text{EM}}$  is  
 1350 much lower on average in this case, below 0.1, because the 10 ns lifetime particles  
 1351 rarely decay before passing through the electromagnetic calorimeter. Figure 35  
 1352 also includes simulated Z decays to electrons or tau leptons. From the decays

1353 to electrons it is clear that the majority of electrons have  $f_{\text{EM}}$  above 0.9. The  
 1354 tau decays include a variety of products. Muons can be seen in the bin where  
 1355  $E/p = 0$  and  $f_{\text{EM}} = 0$  because they do not have an associated jet. Electrons fall  
 1356 into the range where  $E/p > 1$  and  $f_{\text{EM}} > 0.9$ . Hadronic tau decays are the most  
 1357 common, and fall in the range of  $0.1 < f_{\text{EM}} < 0.9$  and  $E/p > 1.0$ .

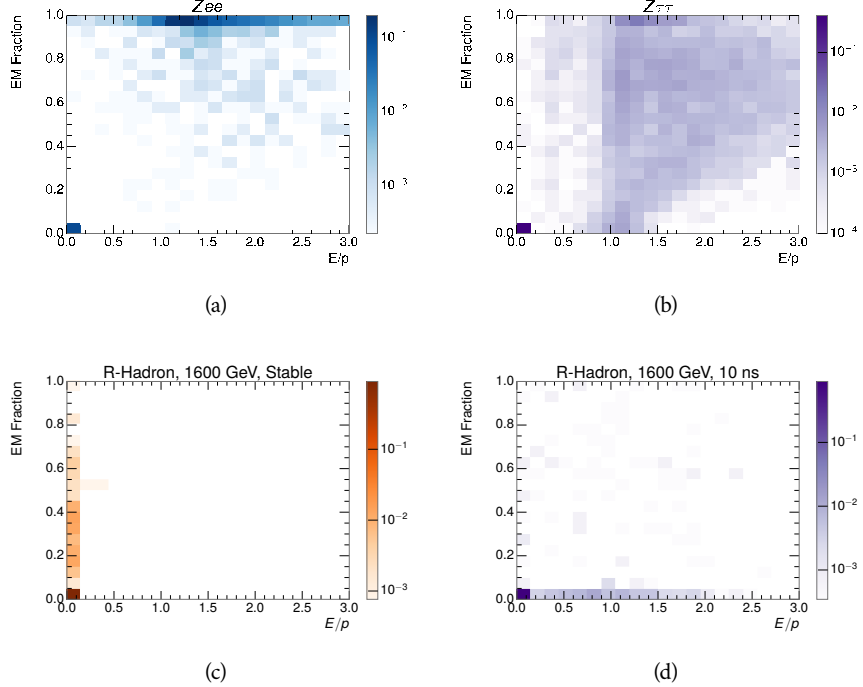


Figure 35: The normalized, two-dimensional distribution of  $E/p$  and  $f_{\text{EM}}$  for simulated  
 (a)  $Z \rightarrow ee$ , (b)  $Z \rightarrow \tau\tau$ , (c) 1200 GeV Stable R-Hadron events, and (d) 1200  
 GeV, 10 ns R-Hadron events.

1358 These differences motivate an electron rejection by requiring an  $f_{\text{EM}}$  below  
 1359 0.9. Similarly, isolated hadrons are rejected by requiring  $E/p < 1.0$ . These re-  
 1360 quirements combine to remove the majority of isolated electrons and hadrons  
 1361 but retain over 95% of the simulated signal across a range of masses and lifetimes.

## 1362 11.4 IONIZATION

1363 The final requirement on the candidate track is the primary discriminating vari-  
 1364 able, the ionization in the pixel detector. That ionization is measured in terms  
 1365 of  $dE/dx$ , which was shown for data and simulated signal events in Figure 31.  
 1366  $dE/dx$  is dramatically greater for the high mass signal particles than the back-  
 1367 grounds, which start to fall immediately after the minimally ionizing peak at 1.1  
 1368  $\text{MeV g}^{-1} \text{cm}^2$ . The  $dE/dx$  for candidate tracks must be greater than a pseudorapidity-  
 1369 dependent threshold, specifically  $1.80 - 0.11|\eta| + 0.17\eta^2 - 0.05\eta^3 \text{ MeV g}^{-1} \text{ cm}^{-2}$ ,  
 1370 in order to correct for an approximately 5% dependence of the MIP peak on  $\eta$ .  
 1371 The requirement was chosen as part of the signal region optimization, and man-

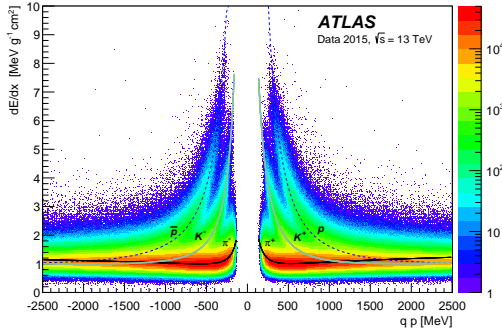


Figure 36: Two-dimensional distribution of  $dE/dx$  versus charge signed momentum ( $qp$ ) for minimum-bias tracks. The fitted distributions of the most probable values for pions, kaons and protons are superimposed.

ages to reduce the backgrounds by a factor of 100 while remaining 70-90% efficient for simulated signal events depending on the mass.

#### 11.4.1 MASS ESTIMATION

The mean value of ionization in silicon is governed by the Bethe equation and the most probable value follows a Landau-Vavilov distribution [49]. Those forms inspire a parametric description of  $dE/dx$  in terms of  $\beta\gamma$ ,

$$(dE/dx)_{MPV}(\beta\gamma) = \frac{p_1}{\beta^{p_3}} \ln(1 + [p_2 \beta\gamma]^{p_5}) - p_4 \quad (2)$$

which performs well in the range  $0.3 < \beta\gamma < 1.5$ . This range includes the expected range of  $\beta\gamma$  for the particles targeted for this search, with  $\beta\gamma \approx 2.0$  for lower mass particles ( $O(100 \text{ GeV})$ ) and up to  $\beta\gamma \approx 0.5$  for higher mass particles ( $O(1000 \text{ GeV})$ ). The parameters,  $p_i$ , are fit using a 2015 data sample of low-momentum pions, kaons, and protons as described in Ref. [70]. Figure 36 shows the two-dimensional distribution of  $dE/dx$  and momentum along with the above fitted values for  $(dE/dx)_{MPV}$ .

The above equation (2) is then numerically inverted to estimate  $\beta\gamma$  and the mass for each candidate track. In simulated signal events, the mean of this mass value reproduces the generated mass up to around 1800 GeV to within 3%, and 3% shift is applied to correct for this difference. The mass distributions prior to this correction are shown for a few stable mass points in Figure 37. The large widths of these distributions come from the high variability in energy deposits in the pixel detector as well as the uncertainty on momentum measurements at high momentum, but the means converge to the expected values.

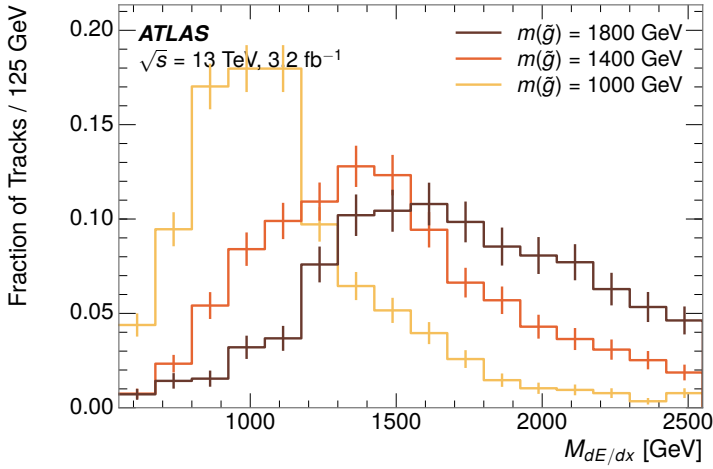


Figure 37: The distribution of mass estimated using  $dE/dx$  for simulated stable R-Hadrons with masses between 1000 and 1600 GeV.

1393 This analysis evaluates expected yields and the resulting cross sectional limits  
 1394 using windows in this mass variable. The windows are formed by fitting mass  
 1395 distributions in simulated signal events like those in Figure 37 to Gaussian distri-  
 1396 butions and taking all events that fall within  $\pm 1.4\sigma$  of the mean. As can be seen  
 1397 in Figure 37, typical values for this width are  $\sigma \approx 300 - 500$  GeV depending on  
 1398 the generated mass.

## 1399 11.5 EFFICIENCY

1400 The numbers of events passing each requirement through ionization are shown  
 1401 in Table 2 for the full 2015 dataset and a simulated 1600 GeV, 10 ns lifetime R-  
 1402 Hadron sample. The table highlights the overall acceptance  $\times$  efficiency for sig-  
 1403 nal events, which for this example is 19%. Between SM rejection and ionization,  
 1404 this signal region reduces the background of tracks which pass the kinematic  
 1405 requirements down by an additional factor of almost 2000.

1406 There is a strong dependence of this efficiency on lifetime and mass, with effi-  
 1407 ciencies dropping to under 1% at low lifetimes. Figure 38 shows the dependence  
 1408 on both mass and lifetime for all signal samples considered in this search. The  
 1409 dependence on mass is relatively slight and comes predominantly from the in-  
 1410 creasing fraction of R-Hadrons which pass the ionization cut with increasing  
 1411 mass. The trigger and  $E_T^{\text{miss}}$  requirements are most efficient for particles that  
 1412 decay before reaching the calorimeters. However, the chance of a particle to be  
 1413 reconstructed as a high-quality track decreases significantly at low lifetimes as  
 1414 the particle does not propagate sufficiently through the inner detector. These  
 1415 effects lead to a maximum in the selection efficiency for lifetimes around 10-30  
 1416 ns.

1417 The inefficiency of this signal region at short lifetimes comes almost exclu-  
 1418 sively from an acceptance effect, in that the particles do not reach the necessary

Selection	Exp. Signal Events	Observed Events in $3.2 \text{ fb}^{-1}$
Generated	$26.0 \pm 0.3$	
$E_T^{\text{miss}}$ Trigger	$24.8 \pm 0.3$ (95%)	
$E_T^{\text{miss}} > 130 \text{ GeV}$	$23.9 \pm 0.3$ (92%)	
Track Quality and $p_T > 50$	$10.7 \pm 0.2$ (41%)	368324
Isolation Requirement	$9.0 \pm 0.2$ (35%)	108079
Track $p > 150 \text{ GeV}$	$6.6 \pm 0.2$ (25%)	47463
$M_T > 130 \text{ GeV}$	$5.8 \pm 0.2$ (22%)	18746
Electron and Hadron Veto	$5.5 \pm 0.2$ (21%)	3612
Muon Veto	$5.5 \pm 0.2$ (21%)	1668
Ionization Requirement	$5.0 \pm 0.1$ (19%)	11

Table 2: The expected number of events at each level of the selection for metastable  $1600 \text{ GeV}, 10 \text{ ns}$  R-Hadrons, along with the number of events observed in data, for  $3.2 \text{ fb}^{-1}$ . The simulated yields are shown with statistical uncertainties only. The total efficiency  $\times$  acceptance is also shown for the signal.

1419 layers of the SCT. This can be seen more clearly by defining a fiducial region  
 1420 which includes events with at least one R-Hadron that is produced with non-  
 1421 zero charge,  $p_T > 50 \text{ GeV}$ ,  $p > 150 \text{ GeV}$ ,  $|\eta| < 2.5$ , and a decay distance greater  
 1422 than 37 cm in the transverse plane. At short (1 ns) lifetimes, the acceptance into  
 1423 this region is as low as 4%. Once this acceptance is accounted for, the selection  
 1424 efficiency ranges from 25% at lifetimes of 1 ns up to 45% at lifetimes of 10 ns.

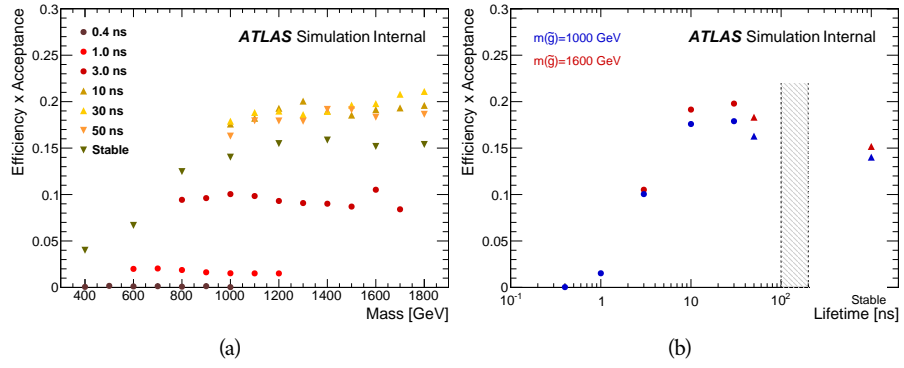


Figure 38: The acceptance  $\times$  efficiency as a function of R-Hadron (a) mass and (b) lifetime. (a) shows all of the combinations of mass and lifetime considered in this search, and (b) highlights the lifetime dependence for 1000 GeV and 1600 GeV R-Hadrons.

1425

1426 BACKGROUND ESTIMATION

---

1427 The event selection discussed in the previous section focuses on detector signa-  
 1428 tures, emphasizing a single high-momentum, highly-ionizing track. That track  
 1429 is then required to be in some way inconsistent with the expected properties  
 1430 of SM particles, with various requirements designed to reject jets, hadrons,  
 1431 electrons, and muons (Section 11.3). Therefore the background for this search comes  
 1432 entirely from reducible backgrounds that are outliers of various distributions in-  
 1433 cluding  $dE/dx$ ,  $f_{\text{EM}}$ , and  $p_T^{\text{Cone}}$ . The simulation can be tuned in various ways to  
 1434 do an excellent job of modeling the average properties of each particle type [71],  
 1435 but it is not necessarily expected to accurately reproduce outliers. For this rea-  
 1436 sons, the background estimation used for this search is estimated entirely using  
 1437 data.

## 1438 12.1 BACKGROUND SOURCES

1439 SM charged particles with lifetimes long enough to form tracks in the inner de-  
 1440 tector can be grouped into three major categories based on their detector inter-  
 1441 actions: hadrons, electrons, and muons. Every particle that enters into the back-  
 1442 ground for this search belongs to one of these types. Relatively pure samples of  
 1443 tracks from each of these types can be formed in data by inverting the various  
 1444 rejection techniques in Section 11.3. Specifically, muons are selected requiring  
 1445 medium muon identification, electrons requiring  $E/p > 1.0$  and  $f_{\text{EM}} > 0.95$ ,  
 1446 and hadrons requiring  $E/p > 1.0$  and  $f_{\text{EM}} < 0.95$ .

1447 Figure 39 shows the distributions of momentum and  $dE/dx$  for these cate-  
 1448 gories in data, after requiring the event level selection as well as the track re-  
 1449 quirements on  $p_T$ , hits, and  $N_{\text{split}}$ , as discussed in Section 11.2. Simulated signal  
 1450 events are included for reference. These distribution are only illustrative of the  
 1451 differences between types, as the rejection requirements could alter their shape.  
 1452 This is especially significant for momentum which enters directly into  $E/p$  and  
 1453 can indirectly affect muon identification. However the various types show clear  
 1454 differences in both distributions. The distributions of momentum are not nec-  
 1455 essarily expected to match between the various types because the production  
 1456 mechanisms for each type result in different kinematic distributions.  $dE/dx$  is  
 1457 also different between types because of incomplete isolation; although the re-  
 1458 quirement on  $N_{\text{split}}$  helps to reduce the contribution of nearby particles it does  
 1459 not completely remove the effect of overlaps. Muons are better isolated because  
 1460 they do not have the additional particle from hadronization present for hadrons  
 1461 and they are significantly less likely do interact with the detector and produce  
 1462 secondary particles compared to hadrons and electrons. Thus muons have the  
 1463 smallest fraction of  $dE/dx$  above the threshold of  $1.8 \text{ MeVg}^{-1}\text{cm}^2$ ; hadrons and  
 1464 electrons have a larger fraction above this threshold.

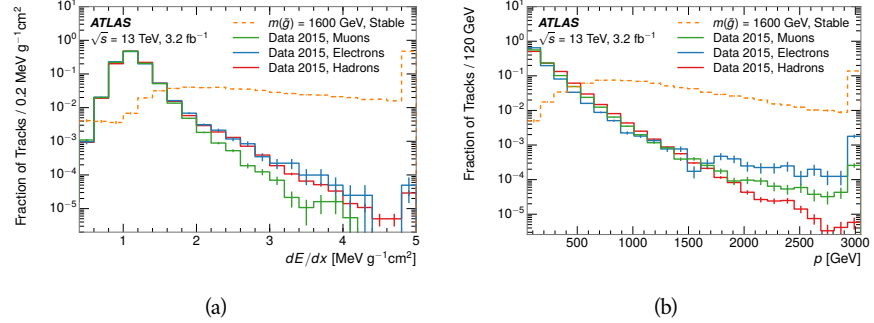


Figure 39: The distribution of (a)  $dE/dx$  and (b) momentum for tracks in data and simulated signal after requiring the event level selection and the track selection on  $p_T$ , hits, and  $N_{\text{split}}$ . Each sub-figure shows the normalized distributions for tracks classified as hadrons, electrons, and muons in data and R-Hadrons in the simulated signal.

1465 It is difficult to determine what fraction of each particle type enters into the fi-  
 1466 nal signal region. The background method will not have significant dependence  
 1467 on the relative contributions of each species, but it is useful to understand the  
 1468 differences between each when considering the various tests of the method.

## 1469 12.2 PREDICTION METHOD

1470 The data-driven background estimation relies on the independence between ion-  
 1471 ization and other kinematic variables in the event. For standard model particles  
 1472 with momenta above 50 GeV,  $dE/dx$  is not correlated with momentum; though  
 1473 there is a slight relativistic rise as momentum increases, the effect is small com-  
 1474 pared to the width of the distribution of ionization energy deposits.. So, the  
 1475 proposed method to estimate the mass distribution of the signal region is to use  
 1476 momentum from a track with low  $dE/dx$  (below the threshold value) and to com-  
 1477 bine it with a random  $dE/dx$  value from a  $dE/dx$  template. The resulting track is  
 1478 just as likely as the original, so a number of such random generations provide the  
 1479 expected distributions of momentum and ionization. These are then combined  
 1480 using the parametrization described in Section 11.4.1 to form a distribution of  
 1481 mass for the signal region.

1482 Algorithmically this method is implemented by forming two distinct Control  
 1483 Regions (**CRs**). The first **CR**, CR1, is formed by applying the entire event selec-  
 1484 tion from Chapter 11 up to the  $dE/dx$  and mass requirements. The  $dE/dx$  re-  
 1485 quirement is instead inverted for this region. Because of the independence of  
 1486  $dE/dx$ , the tracks in this control region have the same kinematic distribution  
 1487 as the tracks in the signal region, and are used to measure a two-dimensional  
 1488 template of  $p$  and  $\eta$ . The second **CR**, CR2, is formed from the event selection  
 1489 through the  $dE/dx$  requirement, but with an inverted  $E_T^{\text{miss}}$  requirement. The  
 1490 tracks in this control region are expected to have similar  $dE/dx$  distributions to  
 1491 the signal region before the ionization requirement, and so this region is used to  
 1492 measure a two-dimensional template of  $dE/dx$  and  $\eta$ .

1493     The contribution of any signal to the control regions is minimized by the in-  
 1494     verted selection requirements. Only less than 10% of simulated signal events  
 1495     have either  $dE/dx$  or  $E_T^{\text{miss}}$  below the threshold values in the original signal re-  
 1496     gion, while the backgrounds are significantly enhanced by inverting those re-  
 1497     quirements. The signal contamination is less than 1% in both control regions  
 1498     for all of the simulated masses and lifetimes considered in this analysis.

1499     With those measured templates, the shape of the mass estimation is generated  
 1500     by first selecting a random  $(p, \eta)$  combination from CR1. This momentum  
 1501     value is combined with a  $dE/dx$  value taken from the appropriate distribution  
 1502     of  $dE/dx$  for the selected  $\eta$  from CR2. The use of  $\eta$  in both random samplings  
 1503     controls for any correlation between  $p$ ,  $dE/dx$ , and  $\eta$ . Those values are then  
 1504     used to calculate a mass in the same way that is done for regular tracks in data,  
 1505     see Section 11.4.1. As this procedure includes all  $dE/dx$  values, the cut at 1.8  
 1506     MeVg $^{-1}$ cm $^2$  is then enforced to fully model the signal region. The generated  
 1507     mass distribution is then normalized by scaling the background estimate to the  
 1508     data in the region  $M < 160$  GeV, where signals of this type have already been  
 1509     excluded [55]. This normalization uses the distributions of mass generated with-  
 1510     out the ionization requirement.

1511     The statistical uncertainties on these background distributions are calculated  
 1512     by independently fluctuating each bin of the input templates according to their  
 1513     Poisson uncertainties. These fluctuations are repeated a large number of times,  
 1514     and the uncertainty on the resulting distribution is taken as the root mean square  
 1515     (RMS) deviation of the fluctuations from the average. As the procedure uses one  
 1516     million random combinations to generate the distributions, The statistical un-  
 1517     certainty from the actual random generations is negligible compared to the un-  
 1518     certainty from measuring the templates.

## 1519     12.3 VALIDATION

1520     The validity of the background estimation technique can be evaluated in both  
 1521     data and simulation. The underlying assumption that random combinations of  
 1522      $dE/dx$  and momentum can predict a mass distribution in an orthogonal region  
 1523     can be tested using simulated samples where concerns like multiple particle types  
 1524     can be controlled. Using the same technique in another set of signal-depleted  
 1525     regions in data then extends this confidence to the more complicated case where  
 1526     several particle species are inherently included.

### 1527     12.3.1 CLOSURE IN SIMULATION

1528     The first test of the procedure is done using a simulated sample of  $W \rightarrow \mu\nu$   
 1529     decays. These types of events provide the ingredients required to test the back-  
 1530     ground estimate,  $E_T^{\text{miss}}$  and isolated tracks, with high statistics. In this example  
 1531     there is no signal, so simulated events in the orthogonal CRs are used to estimate  
 1532     the shape of the mass distribution of the simulated events in the signal region. To  
 1533     reflect the different topology for W boson decays, the CRs use slightly modified  
 1534     definitions. In all CRs, the requirement of  $p > 150$  GeV and the SM rejection

1535 requirements are removed. Additionally, for the signal region the requirement  
 1536 on  $E_T^{\text{miss}}$  is relaxed to 30 GeV and the corresponding inverted requirement on  
 1537 CR2 is also set at 30 GeV.

1538 With these modified selections, the simulated and randomly generated distri-  
 1539 butions of  $M_{dE/dx}$  are shown in Figure 40. This figure includes the mass distri-  
 1540 butions before and after the requirement on  $dE/dx$ , which significantly shapes  
 1541 the distributions. In both cases the background estimation technique repro-  
 1542 duces the shape of  $M_{dE/dx}$  in the signal region. There is a small difference in the pos-  
 1543 itive tail of the mass distribution prior to the ionization cut, where the random  
 1544 events underestimate the fraction of tracks with mass above 150 GeV by about  
 1545 20%. After the ionization requirement, however, this discrepancy is not present  
 1546 and the two distributions agree to within statistical uncertainties.

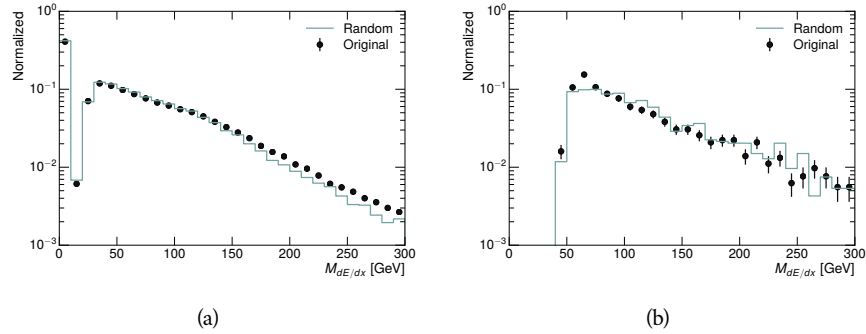


Figure 40: The distribution of  $M_{dE/dx}$  (a) before and (b) after the ionization requirement for tracks in simulated W boson decays and for the randomly generated back-  
 ground estimate.

1547 This ability to reproduce the shape of the mass distribution in simulated events  
 1548 shows that the technique works as expected. No significant biases are acquired  
 1549 in using low  $dE/dx$  events to select kinematic templates or in using low  $E_T^{\text{miss}}$   
 1550 events to select ionization templates, as either would result in a mismodeling of  
 1551 the shape of the mass distribution. The simulated events contain only one par-  
 1552 ticle type, however, so this test only establishes that the technique works well  
 1553 when the the CRs are populated by exactly the same species.

### 1554 12.3.2 VALIDATION REGION IN DATA

1555 The second test of the background estimate is performed using data in an or-  
 1556 thogonal validation region. The validation region, and the corresponding CRs,  
 1557 are formed using the same selection requirements as in the nominal method but  
 1558 with a modified requirement on momentum,  $50 < p[\text{GeV}] < 150$ . This allows  
 1559 the technique to be checked in a region with very similar properties but where  
 1560 the signal is depleted, as the majority of the signal has momentum above 150  
 1561 GeV while the backgrounds are enhanced below that threshold. Any biases on  
 1562 the particle composition of the CRs for the signal region will be reflected in the  
 1563 CRs used to estimate the mass distribution in the validation region.

1564      Figure 41 shows the measured and randomly generated mass distributions for  
 1565      data before and after the ionization requirement. The background estimate does  
 1566      an excellent job of modeling the actual background before the ionization require-  
 1567      ment, with good agreement to within the statistical uncertainties out to the limit  
 1568      of the mass distribution. There are very few events in the validation region after  
 1569      the ionization requirement, but the few observed events are consistent with the  
 1570      background prediction. The good agreement in this validation region provides  
 1571      a confirmation that the technique works even in the full-complexity case with  
 1572      multiple particle types entering the distributions. Any bias from changes in par-  
 1573      ticle composition between regions is small compared to statistical uncertainties.

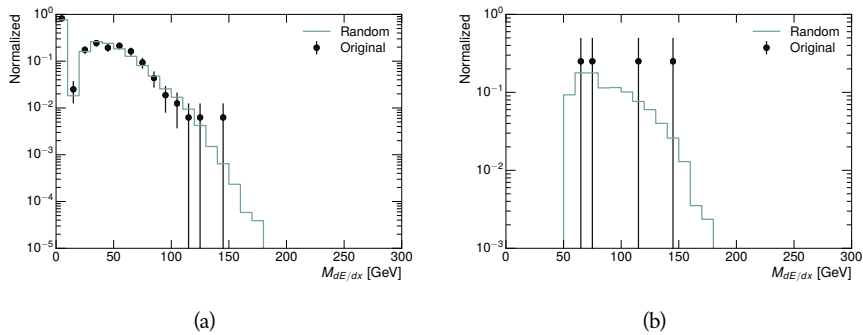


Figure 41: The distribution of  $M_{dE/dx}$  (a) before and (b) after the ionization require-  
 ment for tracks in the validation region and for the randomly generated back-  
 ground estimate.



1574

1575 SYSTEMATIC UNCERTAINTIES AND RESULTS

---

## 1576 13.1 SYSTEMATIC UNCERTAINTIES

1577 A number of systematic uncertainties affect the interpretation of the results of  
 1578 the search. These uncertainties can broken down into two major categories,  
 1579 those which affect the estimate of the background using data and those which  
 1580 affect the measurement of the signal yield estimated with simulated events. The  
 1581 total measured systematic uncertainties are 7% for the background estimation  
 1582 and approximately 32% for the signal yield depending on lifetime. These system-  
 1583 atic uncertainties are expected to be small compared to the statistical fluctuations  
 1584 of the measured yields so that measured cross-sectional limits will be dominated  
 1585 by statistical uncertainties. The following sections describe each source of sys-  
 1586 tematic uncertainty for each of the two types.

## 1587 13.1.1 BACKGROUND ESTIMATE

1588 The systematic uncertainties on the background estimate come primarily from  
 1589 considering alternative methods for generating the background distributions.  
 1590 These uncertainties are small compared to the statistical uncertainties on the  
 1591 background estimate which come from the limited statistics in measuring the  
 1592 template distributions, as described in Section 12.2. They are summarized in  
 1593 Table 3.

Source of Uncertainty:	Value [%]
Analytic Description of $dE/dx$	4.0
Muon Fraction (Stable Region only)	3.0
IBL Ionization Correction	3.8
Normalization	3.0
Total (Metastable Region):	6.3
Total (Stable Region):	7.0

Table 3: A summary of the sources of systematic uncertainty for the data-driven background in the signal region. If the uncertainty depends on the mass, the maximum values are reported.

1594 13.1.1.1 ANALYTIC DESCRIPTION OF  $DE/DX$ 

1595 The background estimate uses a binned template distribution to estimate the  
 1596  $dE/dx$  of tracks in the signal region, as described in Section 12.2. It is also possi-

ble to fit that measured distribution to a functional form to help smooth the distribution in the tails of  $dE/dx$  where the template is driven by a small number of tracks. Both Landau convolved with a Gaussian and Crystal Ball functions are considered as the functional form and used to re-estimate the background distribution. The deviations compared to the nominal method are found to be 4%, and this is taken as a systematic uncertainty to cover the inability carefully predict the contribution from the long tail of  $dE/dx$  where there are few measurements available in data.

#### 1605 13.11.2 MUON FRACTION

1606 The stable region of the analysis explicitly includes tracks identified as muons,  
 1607 which have a known difference in their  $dE/dx$  distribution from non-muon  
 1608 tracks (Section 12.1). To account for a difference in muon fraction between the  
 1609 background region and the signal region for this selection, the  $dE/dx$  templates  
 1610 for muons and non-muons are measured separately and then the relative frac-  
 1611 tion of each is varied in the random generation. The muon fraction is varied by  
 1612 its statistical uncertainty and the resulting difference of 3% in background yield  
 1613 is taken as the systematic uncertainty.

#### 1614 13.11.3 INSERTIBLE B-LAYER (IBL) CORRECTIONS

1615 The acIBL, described in Section 6.3.1, received a significant dose of radiation  
 1616 during the data collection in 2015. The irradiation effect the electronics and can  
 1617 alter the  $dE/dx$  measurement which includes the ToT from the IBL. These effects  
 1618 are corrected for in the nominal analysis by scaling the  $dE/dx$  measurements  
 1619 by a constant factor derived for each run to match the average  $dE/dx$  value to  
 1620 a reference run where the IBL was known to be stable to this effect. However,  
 1621 this corrective factor does not account for inter-run variations. To account for  
 1622 this potential drift of  $dE/dx$ , the correction procedure is repeated by varying  
 1623 the corrections up and down by the maximal run-to-run variation from the full  
 1624 data-taking period, which results in an uncertainty of 3.8%.

#### 1625 13.11.4 NORMALIZATION

1626 As described in Section 12.2, the generated distribution of masses is normalized  
 1627 in a shoulder region ( $M < 160$  GeV) where signals have been excluded by pre-  
 1628 vious analyses. That normalization factor is varied by its statistical uncertainty  
 1629 and the resulting fluctuation in the mass distribution of 3% is taken as a system-  
 1630 atic uncertainty on the background estimate.

#### 1631 13.1.2 SIGNAL YIELD

1632 The systematic uncertainties on the signal yield can be divided into three cate-  
 1633 gories; those on the simulation process, those on the modeling of the detector  
 1634 efficiency or calibration, and those affecting the overall signal yield. They are  
 1635 summarized in Table 3. The largest uncertainty comes from the uncertainty on

1636 the production cross section for gluinos, which is the dominant systematic un-  
 1637 certainty in this analysis.

Source of Uncertainty	-[%]	+[%]
ISR Modeling (Metastable Region)	1.5	1.5
ISR Modeling (Stable Region)	14	14
Pile-up Reweighting	1.1	1.1
Trigger Efficiency Reweighting	0.9	0.9
$E_T^{\text{miss}}$ Scale	1.1	2.2
Ionization Parametrization	7.1	0
Momentum Parametrization	0.3	0.0
Electron Rejection	0.0	0.0
Hadron Rejection	0.0	0.0
$\mu$ Identification	4.3	4.3
Luminosity	5	5
Signal size uncertainty	28	28
Total (Metastable Region)	30	29
Total (Stable Region)	33	32

Table 4: A summary of the sources of systematic uncertainty for the simulated signal yield. The uncertainty depends on the mass and lifetime, and the maximum negative and positive values are reported in the table.

### 1638 13.1.2.1 ISR MODELING

1639 As discussed in Section 10.2, MadGraph is expected to reproduce the distribution  
 1640 of ISR in signal events more accurately than the nominal Pythia samples. The  
 1641 analysis reweights the distribution of ISR in the simulated signal events to match  
 1642 the distribution found in generated MadGraph samples. This has an effect on the  
 1643 selection efficiency in the signal samples, where ISR contributes to the generation  
 1644 of  $E_T^{\text{miss}}$ . To account for the potential inaccuracy on the simulation of ISR at high  
 1645 energies, half of the difference between the signal efficiency with the reweighted  
 1646 distribution and the original distribution is taken as a systematic uncertainty.

### 1647 13.1.2.2 PILEUP REWEIGHTING

1648 The simulated events were generated prior to data collection with an estimate  
 1649 of the average number of interactions per bunch crossing. This estimate does  
 1650 not match the value of pileup during actual data collection, but a large fraction  
 1651 of the simulated events would be discarded in order to match the distribution in  
 1652 data. Therefore the simulated signal events are not reweighted for pileup by de-  
 1653 fault in the analysis. The effect of the pileup on signal efficiency is not expected  
 1654 to depend on the mass or lifetime of the generated signal events, which allows

1655 all of the generated signal events to be used together to assess the pileup dependence.  
 1656 To account for the potential effect of the difference between the number  
 1657 of interactions per bunch crossing between data and simulation, the difference  
 1658 in yield between the nominal signal events and the reweighted events averaged  
 1659 over all masses and lifetimes is taken as a systematic uncertainty on the yield for  
 1660 each mass and lifetime (1.1%).

### 1661 13.1.2.3 TRIGGER EFFICIENCY REWEIGHTING

1662 As described in Section 11.2, the selection for this analysis does not require a suf-  
 1663 ficiently large value of  $E_T^{\text{miss}}$  to be above the plateau of trigger efficiency. There-  
 1664 fore, some signal events which would otherwise pass the event selection can be  
 1665 excluded because of the trigger requirement. These effects can be difficult to es-  
 1666 timate in simulation, and thus are constrained by comparing data and simulated  
 1667 events in an alternative W boson region which uses decays to muons to find a rel-  
 1668 atively pure sample of events with missing energy. The trigger efficiency for data  
 1669 and simulated W events are shown in Figure 42. The comparison between data  
 1670 and MC in this region constrains the simulation of the trigger efficiency. The  
 1671 simulated signal events are reweighted by the ratio of data to simulation in the  
 1672 W boson decays, while the difference between the data and simulation in those  
 1673 decays is taken as a systematic uncertainty. This results in an uncertainty of only  
 1674 0.9% as the majority of events are well above the plateau and the disagreement  
 1675 between data and simulation is small even below that plateau.

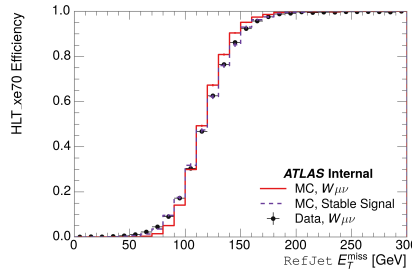


Figure 42: The trigger efficiency for the HLT\_xe70 trigger requirement as a function of Calorimeter  $E_T^{\text{miss}}$  for simulated data events with a W boson selection. Simulated signal events and simulated W boson events are also included.

### 1676 13.1.2.4 MISSING TRANSVERSE MOMENTUM SCALE

1677 The ATLAS Combined Performance (CP) group provides a default recommenda-  
 1678 tion for systematic variations of jets and missing energy (**note: I'm not quite**  
 1679 **sure what to cite for this - I don't see any papers from the jet/met group**  
 1680 **after this was implemented**). These variations enter into this analysis only in  
 1681 the requirement on  $E_T^{\text{miss}}$ . The effect of the measured scale of  $E_T^{\text{miss}}$  is evaluated  
 1682 by varying the  $E_T^{\text{miss}}$  scale according to the one sigma variations provided by all  
 1683 CP recommendations on objects affecting event kinematics in simulated signal  
 1684 events. The  $E_T^{\text{miss}}$  is reconstructed from fully reconstructed objects so any sys-  
 1685 tematic uncertainties affecting jets, muons, electrons, or the  $E_T^{\text{miss}}$  soft terms are

Table 5: Example of the contributing systematic variations to the total systematic for the  $E_T^{\text{miss}}$  Scale, as measured in a 1200 GeV, Stable R-Hadron signal sample.

Systematic Variation	-[%]	+[%]
JET_GroupedNP_1	-0.7	1.3
JET_GroupedNP_2	-0.7	1.2
JET_GroupedNP_3	-0.5	1.3

1686 included. The only non-negligible contributions found using this method are  
 1687 itemized in Table 5 for an example signal sample (1200 GeV, Stable R-Hadron),  
 1688 where the systematic is measured as the relative difference in the final signal  
 1689 efficiency after applying the associated variation through the CP tools. The only  
 1690 variations that are significant are the grouped jet systematic variations, which  
 1691 combine recommended jet systematic uncertainties into linearly independent  
 1692 variations.

1693 As the peak of the reconstructed  $E_T^{\text{miss}}$  distribution in the signal is significantly  
 1694 above the current threshold for events which pass the trigger requirement, the  
 1695 effect of scale variation is expected to be small, which is consistent with the mea-  
 1696 sured systematic of approximately 2%. Events which do not pass the trigger re-  
 1697 quirement usually fail because there are no ISR jets in the event to balance the  
 1698  $R$ -hadrons' transverse momentum, so the reconstructed  $E_T^{\text{miss}}$  is low and there-  
 1699 fore also expected to be not very sensitive to scale changes.

#### 1700 13.1.2.5 MOMENTUM PARAMETRIZATION

1701 The uncertainty on the signal efficiency from track momentum is calculated us-  
 1702 ing the CP group recommendations for tracks. In particular, only one recom-  
 1703 mended systematic variation affects track momentum, the sagitta bias for  $q/P$ .  
 1704 This uncertainty is propagated to the final selection efficiency by varying the  
 1705 track momentum by the recommended one sigma variation, and the associated  
 1706 uncertainty is found to be negligible (0.3%).

#### 1707 13.1.2.6 IONIZATION REQUIREMENT

1708 The  $dE/dx$  distributions in data and simulated events have different most prob-  
 1709 able values, which is due in part to radiation effects in the detector that are not  
 1710 fully accounted for in the simulation. The difference does not affect the mass  
 1711 measurement used in this analysis, as independent calibrations are done in sim-  
 1712 ulation and in data. However, it does affect the efficiency of the high  $dE/dx$   
 1713 selection requirement. To calculate the size of the effect on the signal efficiency,  
 1714 the  $dE/dx$  distribution in signal simulation is scaled by a scale factor obtained  
 1715 from comparing the  $dE/dx$  distribution of inclusive tracks in data and in sim-  
 1716 ulation. The difference in efficiency for this sample with a scaled  $dE/dx$  dis-  
 1717 tribution, relative to the nominal case, is taken as a systematic uncertainty on

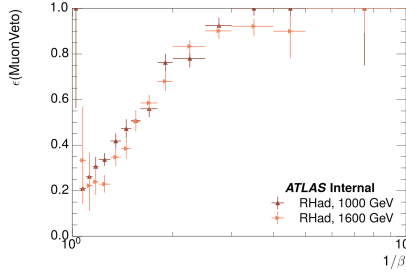


Figure 43: The efficiency of the muon veto for  $R$ -hadrons of two different masses, as a function of  $\frac{1}{\beta}$  for simulated  $R$ -Hadron tracks.

1718 signal efficiency. The uncertainty is as large as 7% for low masses and falls to a  
 1719 negligible effect for large masses.

#### 1720 13.1.2.7 ELECTRON AND JET REJECTION

1721 The systematic uncertainty on the electron rejection is measured by varying the  
 1722 EM fraction requirement significantly, from 0.95 to 0.9. This is found to have  
 1723 a less than 0.04% effect on signal acceptance, on average, and so is completely  
 1724 negligible. Similarly, the uncertainty on jet rejection is measured by tightening  
 1725 the  $E/p$  requirement from 0.5 to 0.4. This is found to have no effect on signal  
 1726 acceptance, so again the systematic is again negligible.

#### 1727 13.1.2.8 MUON VETO

1728  $R$ -Hadrons which traverse the spectrometer but which fail the muon medium  
 1729 identification do so because they fail on the requirement on the number of pre-  
 1730 cision hits required to pass the loose selection. The efficiency of the muon veto  
 1731 for the metastable signal region depends on the time of arrival of the particle  
 1732 at the muon spectrometer relative to prompt particles. This can be seen in Fig-  
 1733 ure 43, which shows the efficiency of the muon veto as a function of  $\frac{1}{\beta}$ , for two  
 1734 simulated stable  $R$ -Hadron samples.

1735 The efficiency of the muon veto depends on the timing resolution of the spec-  
 1736 trometer, so an uncertainty is applied to the signal efficiency to cover differences  
 1737 in timing resolution between data and simulation. This uncertainty is evaluated  
 1738 with the following procedure: first, a sample of  $Z \rightarrow \mu\mu$  events is selected in data  
 1739 in which at least one of the muons is reconstructed as a slow muon, and the re-  
 1740 constructed  $\beta$  distribution, calculated from the MDTs, is compared to the recon-  
 1741 structed  $\beta$  distribution of a  $Z$  sample in simulation. A gaussian fit is performed  
 1742 to the  $\beta$  distributions in both signal and data, and the magnitude of the data/MC  
 1743 difference is used to scale and shift the true  $\beta$  distribution of  $R$ -hadrons in sim-  
 1744 ulation. Signal events are then reweighted based on this varied  $\beta$  distribution,  
 1745 and the difference in the efficiency of the muon veto selection is compared with  
 1746 the nominal and reweighted true  $\beta$  distributions. The difference in muon veto  
 1747 efficiency is taken as a systematic uncertainty of the muon veto.

1748 The comparison of reconstructed  $\beta$  between data and simulation is performed  
 1749 separately in the barrel, transition, and endcap regions of the spectrometer, and

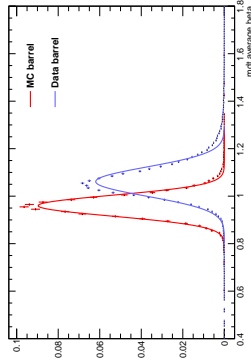


Figure 44: The average reconstructed MDT  $\beta$  distribution for  $Z \rightarrow \mu\mu$  events in which one of the muons is reconstructed as a slow muon, for both data and simulation. A gaussian fit is superimposed.

the reweighting of the true  $\beta$  distribution in signal is done per region. The comparisons of average reconstructed MDT  $\beta$  between data and simulation for each of the three detector regions in Figure 44 for  $Z \rightarrow \mu\mu$  events. The uncertainty is calculated independently for each lifetime; it is found to be negligible for R-hadrons with lifetimes less than 30 ns.

#### 13.1.2.9 LUMINOSITY

The luminosity uncertainty is provided by a luminosity measurement on ATLAS and was measured to be 5% at the time of the publication of this analysis..

#### 13.1.2.10 SIGNAL SIZE

As discussed in Section 10.2, the signal cross sections are calculated at NLO in the strong coupling constant with a resummation of soft-gluon emission at NLL. The uncertainties on those cross sections are between 14% to 28% for the R-Hadrons in the range of 400 to 1800 GeV [67, 68], where the uncertainty increases with the mass.

### 13.2 FINAL YIELDS

### 13.3 CROSS SECTIONAL LIMITS

### 13.4 MASS LIMITS

### 13.5 CONTEXT FOR LONG-LIVED SEARCHES



1768

## PART VI

1769

### CONCLUSIONS

1770

You can put some informational part preamble text here.



# 14

1771

## 1772 SUMMARY AND OUTLOOK

---

### 1773 14.1 SUMMARY

### 1774 14.2 OUTLOOK



1775

## PART VII

1776

## APPENDIX

1777



# A

1778

1779 INELASTIC CROSS SECTION

---



# B

1780

## 1781 APPENDIX TEST

---

1782 Examples: *Italics*, SMALL CAPS, ALL CAPS <sup>1</sup>. Acronym testing: **UML!** (**UML!**) –  
1783 **UML! – UML! (UML!) – UML!s**

This appendix is temporary and is here to be used to check the style of the document.

### 1784 B.1 APPENDIX SECTION TEST

1785 Random text that should take up a few lines. The purpose is to see how sections  
1786 and subsections flow with some actual context. Without some body copy be-  
1787 tween each heading it can be difficult to tell if the weight of the fonts, styles, and  
1788 sizes use work well together.

#### 1789 B.1.1 APPENDIX SUBECTION TEST

1790 Random text that should take up a few lines. The purpose is to see how sections  
1791 and subsections flow with some actual context. Without some body copy be-  
1792 tween each heading it can be difficult to tell if the weight of the fonts, styles, and  
1793 sizes use work well together.

### 1794 B.2 A TABLE AND LISTING

1795 Curabitur tellus magna, porttitor a, commodo a, commodo in, tortor. Donec in-  
1796 terdum. Praesent scelerisque. Maecenas posuere sodales odio. Vivamus metus  
1797 lacus, varius quis, imperdiet quis, rhoncus a, turpis. Etiam ligula arcu, elemen-  
1798 tum a, venenatis quis, sollicitudin sed, metus. Donec nunc pede, tincidunt in,  
1799 venenatis vitae, faucibus vel, nibh. Pellentesque wisi. Nullam malesuada. Morbi  
1800 ut tellus ut pede tincidunt porta. Lorem ipsum dolor sit amet, consectetur adip-  
1801 iscing elit. Etiam congue neque id dolor.

1802 There is also a Python listing below Listing 1.

---

1 Footnote example.

LABITUR BONORUM PRI NO	QUE VISTA	HUMAN
fastidii ea ius	germano	demonstratea
suscipit instructior	titulo	personas
quaestio philosophia	facto	demonstrated

Table 6: Autem usu id.

## 1803 B.3 SOME FORMULAS

Due to the statistical nature of ionisation energy loss, large fluctuations can occur in the amount of energy deposited by a particle traversing an absorber element<sup>2</sup>. Continuous processes such as multiple scattering and energy loss play a relevant role in the longitudinal and lateral development of electromagnetic and hadronic showers, and in the case of sampling calorimeters the measured resolution can be significantly affected by such fluctuations in their active layers. The description of ionisation fluctuations is characterised by the significance parameter  $\kappa$ , which is proportional to the ratio of mean energy loss to the maximum allowed energy transfer in a single collision with an atomic electron:

*You might get unexpected results using math in chapter or section heads. Consider the pdfspacing option.*

$$\kappa = \frac{\xi}{E_{\max}} \quad (3)$$

$E_{\max}$  is the maximum transferable energy in a single collision with an atomic electron.

$$E_{\max} = \frac{2m_e\beta^2\gamma^2}{1 + 2\gamma m_e/m_x + (m_e/m_x)^2},$$

1804 where  $\gamma = E/m_x$ ,  $E$  is energy and  $m_x$  the mass of the incident particle,  $\beta^2 = 1 - 1/\gamma^2$  and  $m_e$  is the electron mass.  $\xi$  comes from the Rutherford scattering cross section and is defined as:

$$\xi = \frac{2\pi z^2 e^4 N_{Av} Z \rho \delta x}{m_e \beta^2 c^2 A} = 153.4 \frac{z^2}{\beta^2} \frac{Z}{A} \rho \delta x \text{ keV},$$

1807 where

- z charge of the incident particle
- $N_{Av}$  Avogadro's number
- Z atomic number of the material
- A atomic weight of the material
- $\rho$  density
- $\delta x$  thickness of the material
- 1809  $\kappa$  measures the contribution of the collisions with energy transfer close to  
1810  $E_{\max}$ . For a given absorber,  $\kappa$  tends towards large values if  $\delta x$  is large and/or if  
1811  $\beta$  is small. Likewise,  $\kappa$  tends towards zero if  $\delta x$  is small and/or if  $\beta$  approaches  
1812 1.

2 Examples taken from Walter Schmidt's great gallery:  
<http://home.vrweb.de/~was/mathfonts.html>

Listing 1: A floating example (listings manual)

---

```
1 for i in xrange(10):
    print i, i*i, i*i*i
print "done"
```

---

1813      The value of  $\kappa$  distinguishes two regimes which occur in the description of  
1814      ionisation fluctuations:

- 1815      1. A large number of collisions involving the loss of all or most of the incident  
1816      particle energy during the traversal of an absorber.

1817      As the total energy transfer is composed of a multitude of small energy  
1818      losses, we can apply the central limit theorem and describe the fluctua-  
1819      tions by a Gaussian distribution. This case is applicable to non-relativistic  
1820      particles and is described by the inequality  $\kappa > 10$  (i. e., when the mean en-  
1821      ergy loss in the absorber is greater than the maximum energy transfer in  
1822      a single collision).

- 1823      2. Particles traversing thin counters and incident electrons under any condi-  
1824      tions.

1825      The relevant inequalities and distributions are  $0.01 < \kappa < 10$ , Vavilov  
1826      distribution, and  $\kappa < 0.01$ , Landau distribution.



- 1828 [1] S. Agostinelli et al. “GEANT4: A simulation toolkit”. In: *Nucl. Instrum. Meth.*  
1829 A 506 (2003), pp. 250–303. doi: [10.1016/S0168-9002\(03\)01368-8](https://doi.org/10.1016/S0168-9002(03)01368-8).
- 1830 [2] ATLAS Collaboration. “A study of the material in the ATLAS inner de-  
1831 tector using secondary hadronic interactions”. In: *JINST* 7 (2012), P01013.  
1832 doi: [10.1088/1748-0221/7/01/P01013](https://doi.org/10.1088/1748-0221/7/01/P01013). arXiv: [1110.6191 \[hep-ex\]](https://arxiv.org/abs/1110.6191).  
1833 PERF-2011-08.
- 1834 [3] ATLAS Collaboration. “Electron and photon energy calibration with the  
1835 ATLAS detector using LHC Run 1 data”. In: *Eur. Phys. J. C* 74 (2014), p. 3071.  
1836 doi: [10.1140/epjc/s10052-014-3071-4](https://doi.org/10.1140/epjc/s10052-014-3071-4). arXiv: [1407.5063](https://arxiv.org/abs/1407.5063)  
1837 [hep-ex]. PERF-2013-05.
- 1838 [4] ATLAS Collaboration. “A measurement of the calorimeter response to sin-  
1839 ggle hadrons and determination of the jet energy scale uncertainty using  
1840 LHC Run-1  $p\bar{p}$ -collision data with the ATLAS detector”. In: (2016). arXiv:  
1841 [1607.08842 \[hep-ex\]](https://arxiv.org/abs/1607.08842). PERF-2015-05.
- 1842 [5] ATLAS Collaboration. “Single hadron response measurement and calorime-  
1843 ter jet energy scale uncertainty with the ATLAS detector at the LHC”. In:  
1844 *Eur. Phys. J. C* 73 (2013), p. 2305. doi: [10.1140/epjc/s10052-013-2305-1](https://doi.org/10.1140/epjc/s10052-013-2305-1). arXiv: [1203.1302 \[hep-ex\]](https://arxiv.org/abs/1203.1302). PERF-2011-05.
- 1846 [6] ATLAS Collaboration. “The ATLAS Simulation Infrastructure”. In: *Eur.*  
1847 *Phys. J. C* 70 (2010), p. 823. doi: [10.1140/epjc/s10052-010-1429-9](https://doi.org/10.1140/epjc/s10052-010-1429-9).  
1848 arXiv: [1005.4568 \[hep-ex\]](https://arxiv.org/abs/1005.4568). SOFT-2010-01.
- 1849 [7] T. Sjöstrand, S. Mrenna, and P. Skands. “A Brief Introduction to PYTHIA  
1850 8.1”. In: *Comput. Phys. Commun.* 178 (2008), pp. 852–867. doi: [10.1016/j.cpc.2008.01.036](https://doi.org/10.1016/j.cpc.2008.01.036). arXiv: [0710.3820](https://arxiv.org/abs/0710.3820).
- 1852 [8] ATLAS Collaboration. *Summary of ATLAS Pythia 8 tunes*. ATL-PHYS-PUB-  
1853 2012-003. 2012. URL: <http://cds.cern.ch/record/1474107>.
- 1854 [9] A.D. Martin, W.J. Stirling, R.S. Thorne, and G. Watt. “Parton distributions  
1855 for the LHC”. In: *Eur. Phys. J. C* 63 (2009). Figures from the [MSTW Website](#),  
1856 pp. 189–285. doi: [10.1140/epjc/s10052-009-1072-5](https://doi.org/10.1140/epjc/s10052-009-1072-5). arXiv: [0901.0002](https://arxiv.org/abs/0901.0002).
- 1858 [10] A. Sherstnev and R.S. Thorne. “Parton Distributions for LO Generators”.  
1859 In: *Eur. Phys. J. C* 55 (2008), pp. 553–575. doi: [10.1140/epjc/s10052-008-0610-x](https://doi.org/10.1140/epjc/s10052-008-0610-x). arXiv: [0711.2473](https://arxiv.org/abs/0711.2473).
- 1861 [11] A. Ribon et al. *Status of Geant4 hadronic physics for the simulation of LHC*  
1862 *experiments at the start of LHC physics program*. CERN-LCGAPP-2010-02.  
1863 2010. URL: <http://lcgapp.cern.ch/project/docs/noteStatusHadronic2010.pdf>.

- 1865 [12] M. P. Guthrie, R. G. Alsmiller, and H. W. Bertini. "Calculation of the cap-  
 1866 ture of negative pions in light elements and comparison with experiments  
 1867 pertaining to cancer radiotherapy". In: *Nucl. Instrum. Meth.* 66 (1968), pp. 29–  
 1868 36. doi: [10.1016/0029-554X\(68\)90054-2](https://doi.org/10.1016/0029-554X(68)90054-2).
- 1869 [13] H. W. Bertini and P. Guthrie. "News item results from medium-energy  
 1870 intranuclear-cascade calculation". In: *Nucl. Instr. and Meth. A* 169 (1971),  
 1871 p. 670. doi: [10.1016/0375-9474\(71\)90710-X](https://doi.org/10.1016/0375-9474(71)90710-X).
- 1872 [14] V.A. Karmanov. "Light Front Wave Function of Relativistic Composite  
 1873 System in Explicitly Solvable Model". In: *Nucl. Phys. B* 166 (1980), p. 378.  
 1874 doi: [10.1016/0550-3213\(80\)90204-7](https://doi.org/10.1016/0550-3213(80)90204-7).
- 1875 [15] H. S. Fesefeldt. *GHEISHA program*. Pitha-85-02, Aachen. 1985.
- 1876 [16] G. Folger and J.P. Wellisch. "String parton models in Geant4". In: (2003).  
 1877 arXiv: [nucl-th/0306007](https://arxiv.org/abs/nucl-th/0306007).
- 1878 [17] N. S. Amelin et al. "Transverse flow and collectivity in ultrarelativistic  
 1879 heavy-ion collisions". In: *Phys. Rev. Lett.* 67 (1991), p. 1523. doi: [10.1103/PhysRevLett.67.1523](https://doi.org/10.1103/PhysRevLett.67.1523).
- 1880 [18] N. S. Amelin et al. "Collectivity in ultrarelativistic heavy ion collisions". In:  
 1881 *Nucl. Phys. A* 544 (1992), p. 463. doi: [10.1016/0375-9474\(92\)90598-E](https://doi.org/10.1016/0375-9474(92)90598-E).
- 1882 [19] L. V. Bravina et al. "Fluid dynamics and Quark Gluon string model - What  
 1883 we can expect for Au+Au collisions at 11.6 AGeV/c". In: *Nucl. Phys. A* 566  
 1884 (1994), p. 461. doi: [10.1016/0375-9474\(94\)90669-6](https://doi.org/10.1016/0375-9474(94)90669-6).
- 1885 [20] L. V. Bravin et al. "Scaling violation of transverse flow in heavy ion colli-  
 1886 sions at AGS energies". In: *Phys. Lett. B* 344 (1995), p. 49. doi: [10.1016/0370-2693\(94\)01560-Y](https://doi.org/10.1016/0370-2693(94)01560-Y).
- 1887 [21] B. Andersson et al. "A model for low-pT hadronic reactions with general-  
 1888 izations to hadron-nucleus and nucleus-nucleus collisions". In: *Nucl. Phys.*  
 1889 *B* 281 (1987), p. 289. doi: [10.1016/0550-3213\(87\)90257-4](https://doi.org/10.1016/0550-3213(87)90257-4).
- 1890 [22] B. Andersson, A. Tai, and B.-H. Sa. "Final state interactions in the (nuclear)  
 1891 FRITIOF string interaction scenario". In: *Z. Phys. C* 70 (1996), pp. 499–  
 1892 506. doi: [10.1007/s002880050127](https://doi.org/10.1007/s002880050127).
- 1893 [23] B. Nilsson-Almqvist and E. Stenlund. "Interactions Between Hadrons and  
 1894 Nuclei: The Lund Monte Carlo, Fritiof Version 1.6". In: *Comput. Phys. Com-*  
 1895 *mun.* 43 (1987), p. 387. doi: [10.1016/0010-4655\(87\)90056-7](https://doi.org/10.1016/0010-4655(87)90056-7).
- 1896 [24] B. Ganhuyag and V. Uzhinsky. "Modified FRITIOF code: Negative charged  
 1897 particle production in high energy nucleus nucleus interactions". In: *Czech.*  
 1898 *J. Phys.* 47 (1997), pp. 913–918. doi: [10.1023/A:1021296114786](https://doi.org/10.1023/A:1021296114786).
- 1899 [25] ATLAS Collaboration. "Topological cell clustering in the ATLAS calorime-  
 1900 ters and its performance in LHC Run 1". In: (2016). arXiv: [1603.02934](https://arxiv.org/abs/1603.02934)  
 1901 [[hep-ex](#)].
- 1902 [26] Peter Speckmayer. "Energy Measurement of Hadrons with the CERN AT-  
 1903 LAS Calorimeter". Presented on 18 Jun 2008. PhD thesis. Vienna: Vienna,  
 1904 Tech. U., 2008. URL: <http://cds.cern.ch/record/1112036>.

- 1908 [27] CMS Collaboration. “The CMS barrel calorimeter response to particle  
1909 beams from 2 to 350 GeV/c”. In: *Eur. Phys. J. C* 60.3 (2009). doi: [10.1140/epjc/s10052-009-0959-5](https://doi.org/10.1140/epjc/s10052-009-0959-5).
- 1911 [28] J. Beringer et al. (Particle Data Group). “Review of Particle Physics”. In:  
1912 *Chin. Phys. C* 38 (2014), p. 090001. URL: <http://pdg.lbl.gov>.
- 1913 [29] P. Adragna et al. “Measurement of Pion and Proton Response and Lon-  
1914 gitudinal Shower Profiles up to 20 Nuclear Interaction Lengths with the  
1915 ATLAS Tile Calorimeter”. In: *Nucl. Instrum. Meth. A* 615 (2010), pp. 158–  
1916 181. doi: [10.1016/j.nima.2010.01.037](https://doi.org/10.1016/j.nima.2010.01.037).
- 1917 [30] ATLAS Collaboration. “Jet energy measurement and its systematic uncer-  
1918 tainty in proton–proton collisions at  $\sqrt{s} = 7$  TeV with the ATLAS detec-  
1919 tor”. In: *Eur. Phys. J. C* 75 (2015), p. 17. doi: [10.1140/epjc/s10052-014-3190-y](https://doi.org/10.1140/epjc/s10052-014-3190-y). arXiv: [1406.0076 \[hep-ex\]](https://arxiv.org/abs/1406.0076). PERF-2012-01.
- 1921 [31] Hung-Liang Lai, Marco Guzzi, Joey Huston, Zhao Li, Pavel M. Nadolsky,  
1922 et al. “New parton distributions for collider physics”. In: *Phys. Rev. D* 82  
1923 (2010), p. 074024. doi: [10.1103/PhysRevD.82.074024](https://doi.org/10.1103/PhysRevD.82.074024). arXiv: [1007.2241 \[hep-ph\]](https://arxiv.org/abs/1007.2241).
- 1925 [32] E. Abat et al. “Study of energy response and resolution of the ATLAS barrel  
1926 calorimeter to hadrons of energies from 20 to 350 GeV”. In: *Nucl. Instrum.*  
1927 *Meth. A* 621.1-3 (2010), pp. 134 – 150. doi: <http://dx.doi.org/10.1016/j.nima.2010.04.054>.
- 1929 [33] ATLAS Collaboration. “Jet energy measurement with the ATLAS detector  
1930 in proton–proton collisions at  $\sqrt{s} = 7$  TeV”. In: *Eur. Phys. J. C* 73 (2013),  
1931 p. 2304. doi: [10.1140/epjc/s10052-013-2304-2](https://doi.org/10.1140/epjc/s10052-013-2304-2). arXiv: [1112.6426 \[hep-ex\]](https://arxiv.org/abs/1112.6426). PERF-2011-03.
- 1933 [34] Nausheen R. Shah and Carlos E. M. Wagner. “Gravitons and dark matter in  
1934 universal extra dimensions”. In: *Phys. Rev. D* 74 (2006), p. 104008. doi: [10.1103/PhysRevD.74.104008](https://doi.org/10.1103/PhysRevD.74.104008). arXiv: [hep-ph/0608140 \[hep-ph\]](https://arxiv.org/abs/hep-ph/0608140).
- 1936 [35] Jonathan L. Feng, Arvind Rajaraman, and Fumihiro Takayama. “Graviton  
1937 cosmology in universal extra dimensions”. In: *Phys. Rev. D* 68 (2003), p. 085018.  
1938 doi: [10.1103/PhysRevD.68.085018](https://doi.org/10.1103/PhysRevD.68.085018). arXiv: [hep-ph/0307375 \[hep-ph\]](https://arxiv.org/abs/hep-ph/0307375).
- 1940 [36] Paul H. Frampton and Pham Quang Hung. “Long-lived quarks?” In: *Phys.*  
1941 *Rev. D* 58 (5 1998), p. 057704. doi: [10.1103/PhysRevD.58.057704](https://doi.org/10.1103/PhysRevD.58.057704).  
1942 URL: <http://link.aps.org/doi/10.1103/PhysRevD.58.057704>.
- 1944 [37] C. Friberg, E. Norrbin, and T. Sjostrand. “QCD aspects of leptoquark pro-  
1945 duction at HERA”. In: *Phys. Lett. B* 403 (1997), pp. 329–334. doi: [10.1016/S0370-2693\(97\)00543-1](https://doi.org/10.1016/S0370-2693(97)00543-1). arXiv: [hep-ph/9704214 \[hep-ph\]](https://arxiv.org/abs/hep-ph/9704214).
- 1947 [38] Herbert K. Dreiner. “An introduction to explicit R-parity violation”. In:  
1948 (1997). arXiv: [hep-ph/9707435](https://arxiv.org/abs/hep-ph/9707435).

- 1949 [39] Edmond L. Berger and Zack Sullivan. “Lower limits on R-parity-violating  
1950 couplings in supersymmetry”. In: *Phys. Rev. Lett.* 92 (2004), p. 201801. doi:  
1951 [10.1103/PhysRevLett.92.201801](https://doi.org/10.1103/PhysRevLett.92.201801). arXiv: [hep-ph/0310001](https://arxiv.org/abs/hep-ph/0310001).
- 1952 [40] R. Barbieri, C. Berat, M. Besancon, M. Chemtob, A. Deandrea, et al. “R-  
1953 parity violating supersymmetry”. In: *Phys. Rept.* 420 (2005), p. 1. doi: [10.1016/j.physrep.2005.08.006](https://doi.org/10.1016/j.physrep.2005.08.006). arXiv: [hep-ph/0406039](https://arxiv.org/abs/hep-ph/0406039).
- 1955 [41] M. Fairbairn et al. “Stable massive particles at colliders”. In: *Phys. Rept.* 438  
1956 (2007), p. 1. doi: [10.1016/j.physrep.2006.10.002](https://doi.org/10.1016/j.physrep.2006.10.002). arXiv: [hep-ph/0611040](https://arxiv.org/abs/hep-ph/0611040).
- 1958 [42] Christopher F. Kolda. “Gauge-mediated supersymmetry breaking: Intro-  
1959 duction, review and update”. In: *Nucl. Phys. Proc. Suppl.* 62 (1998), p. 266.  
1960 doi: [10.1016/S0920-5632\(97\)00667-1](https://doi.org/10.1016/S0920-5632(97)00667-1). arXiv: [hep-ph/9707450](https://arxiv.org/abs/hep-ph/9707450).
- 1961 [43] Howard Baer, Kingman Cheung, and John F. Gunion. “A Heavy gluino as  
1962 the lightest supersymmetric particle”. In: *Phys. Rev. D* 59 (1999), p. 075002.  
1963 doi: [10.1103/PhysRevD.59.075002](https://doi.org/10.1103/PhysRevD.59.075002). arXiv: [hep-ph/9806361](https://arxiv.org/abs/hep-ph/9806361).
- 1964 [44] S. James Gates Jr. and Oleg Lebedev. “Searching for supersymmetry in  
1965 hadrons”. In: *Phys. Lett. B* 477 (2000), p. 216. doi: [10.1016/S0370-2693\(00\)00172-6](https://doi.org/10.1016/S0370-2693(00)00172-6). arXiv: [hep-ph/9912362](https://arxiv.org/abs/hep-ph/9912362).
- 1967 [45] G. F. Giudice and A. Romanino. “Split supersymmetry”. In: *Nucl. Phys. B*  
1968 699 (2004), p. 65. doi: [10.1016/j.nuclphysb.2004.11.048](https://doi.org/10.1016/j.nuclphysb.2004.11.048). arXiv:  
1969 [hep-ph/0406088](https://arxiv.org/abs/hep-ph/0406088).
- 1970 [46] N. Arkani-Hamed, S. Dimopoulos, G. F. Giudice, and A. Romanino. “As-  
1971 pects of split supersymmetry”. In: *Nucl. Phys. B* 709 (2005), p. 3. doi: [10.1016/j.nuclphysb.2004.12.026](https://doi.org/10.1016/j.nuclphysb.2004.12.026). arXiv: [hep-ph/0409232](https://arxiv.org/abs/hep-ph/0409232).
- 1973 [47] Glennys R. Farrar and Pierre Fayet. “Phenomenology of the Production,  
1974 Decay, and Detection of New Hadronic States Associated with Supersym-  
1975 metry”. In: *Phys. Lett.* B76 (1978), pp. 575–579. doi: [10.1016/0370-2693\(78\)90858-4](https://doi.org/10.1016/0370-2693(78)90858-4).
- 1977 [48] A. C. Kraan, J. B. Hansen, and P. Nevski. “Discovery potential of R-hadrons  
1978 with the ATLAS detector”. In: *Eur. Phys. J.* C49 (2007), pp. 623–640. doi:  
1979 [10.1140/epjc/s10052-006-0162-x](https://doi.org/10.1140/epjc/s10052-006-0162-x). arXiv: [hep-ex/0511014](https://arxiv.org/abs/hep-ex/0511014)  
1980 [[hep-ex](https://arxiv.org/abs/hep-ex)].
- 1981 [49] K. A. Olive et al. “Review of Particle Physics”. In: *Chin. Phys.* C38 (2014),  
1982 p. 090001. doi: [10.1088/1674-1137/38/9/090001](https://doi.org/10.1088/1674-1137/38/9/090001).
- 1983 [50] Rasmus Mackeprang and David Milstead. “An Updated Description of  
1984 Heavy-Hadron Interactions in GEANT-4”. In: *Eur. Phys. J.* C66 (2010), pp. 493–  
1985 501. doi: [10.1140/epjc/s10052-010-1262-1](https://doi.org/10.1140/epjc/s10052-010-1262-1). arXiv: [0908.1868](https://arxiv.org/abs/0908.1868)  
1986 [[hep-ph](https://arxiv.org/abs/hep-ph)].
- 1987 [51] ATLAS Collaboration. “Search for massive, long-lived particles using mul-  
1988 titrack displaced vertices or displaced lepton pairs in  $pp$  collisions at  $\sqrt{s} =$   
1989 8 TeV with the ATLAS detector”. In: *Phys. Rev. D* 92 (2015), p. 072004.  
1990 doi: [10.1103/PhysRevD.92.072004](https://doi.org/10.1103/PhysRevD.92.072004). arXiv: [1504.05162](https://arxiv.org/abs/1504.05162) [[hep-ex](https://arxiv.org/abs/hep-ex)].  
1991 SUSY-2014-02.

- 1992 [52] ATLAS Collaboration. “Search for charginos nearly mass degenerate with  
 1993 the lightest neutralino based on a disappearing-track signature in  $pp$  col-  
 1994 lisions at  $\sqrt{s} = 8$  TeV with the ATLAS detector”. In: *Phys. Rev. D* 88 (2013),  
 1995 p. 112006. doi: [10.1103/PhysRevD.88.112006](https://doi.org/10.1103/PhysRevD.88.112006). arXiv: [1310.3675](https://arxiv.org/abs/1310.3675)  
 1996 [[hep-ex](#)]. SUSY-2013-01.
- 1997 [53] ATLAS Collaboration. “Searches for heavy long-lived sleptons and R-Hadrons  
 1998 with the ATLAS detector in  $pp$  collisions at  $\sqrt{s} = 7$  TeV”. In: *Phys. Lett. B*  
 1999 720 (2013), p. 277. doi: [10.1016/j.physletb.2013.02.015](https://doi.org/10.1016/j.physletb.2013.02.015). arXiv:  
 2000 [1211.1597](https://arxiv.org/abs/1211.1597) [[hep-ex](#)]. SUSY-2012-01.
- 2001 [54] ATLAS Collaboration. “Searches for heavy long-lived charged particles  
 2002 with the ATLAS detector in proton–proton collisions at  $\sqrt{s} = 8$  TeV”. In: *JHEP* 01 (2015), p. 068. doi: [10.1007/JHEP01\(2015\)068](https://doi.org/10.1007/JHEP01(2015)068). arXiv:  
 2003 [1411.6795](https://arxiv.org/abs/1411.6795) [[hep-ex](#)]. SUSY-2013-22.
- 2005 [55] ATLAS Collaboration. “Search for metastable heavy charged particles with  
 2006 large ionisation energy loss in  $pp$  collisions at  $\sqrt{s} = 8$  TeV using the AT-  
 2007 LAS experiment”. In: *Eur. Phys. J. C* 75 (2015), p. 407. doi: [10.1140/epjc/s10052-015-3609-0](https://doi.org/10.1140/epjc/s10052-015-3609-0). arXiv: [1506.05332](https://arxiv.org/abs/1506.05332) [[hep-ex](#)]. SUSY-  
 2008 2014-09.
- 2010 [56] ATLAS Collaboration. “Search for heavy long-lived charged  $R$ -hadrons  
 2011 with the ATLAS detector in  $3.2 \text{ fb}^{-1}$  of proton–proton collision data at  
 2012  $\sqrt{s} = 13$  TeV”. In: *Phys. Lett. B* 760 (2016), pp. 647–665. doi: [10.1016/j.physletb.2016.07.042](https://doi.org/10.1016/j.physletb.2016.07.042). arXiv: [1606.05129](https://arxiv.org/abs/1606.05129) [[hep-ex](#)].
- 2014 [57] Torbjorn Sjöstrand, Stephen Mrenna, and Peter Skands. “PYTHIA 6.4 Physics  
 2015 and Manual”. In: *JHEP* 0605 (2006), p. 026. doi: [10.1088/1126-6708/2006/05/026](https://doi.org/10.1088/1126-6708/2006/05/026). arXiv: [hep-ph/0603175](https://arxiv.org/abs/hep-ph/0603175).
- 2017 [58] *Further ATLAS tunes of PYTHIA6 and Pythia 8*. Tech. rep. ATL-PHYS-PUB-  
 2018 2011-014. Geneva: CERN, 2011. URL: <https://cds.cern.ch/record/1400677>.
- 2020 [59] Aafke Christine Kraan. “Interactions of heavy stable hadronizing parti-  
 2021 cles”. In: *Eur. Phys. J. C* 37 (2004), pp. 91–104. doi: [10.1140/epjc/s2004-01946-6](https://doi.org/10.1140/epjc/s2004-01946-6). arXiv: [hep-ex/0404001](https://arxiv.org/abs/hep-ex/0404001) [[hep-ex](#)].
- 2023 [60] M. Fairbairn et al. “Stable massive particles at colliders”. In: *Phys. Rept.* 438  
 2024 (2007), p. 1. doi: [10.1016/j.physrep.2006.10.002](https://doi.org/10.1016/j.physrep.2006.10.002). arXiv: [hep-ph/0611040](https://arxiv.org/abs/hep-ph/0611040).
- 2026 [61] W. Beenakker, R. Hopker, M. Spira, and P. M. Zerwas. “Squark and gluino  
 2027 production at hadron colliders”. In: *Nucl. Phys. B* 492 (1997), p. 51. doi:  
 2028 [10.1016/S0550-3213\(97\)00084-9](https://doi.org/10.1016/S0550-3213(97)00084-9). arXiv: [hep-ph/9610490](https://arxiv.org/abs/hep-ph/9610490).
- 2029 [62] A. Kulesza and L. Motyka. “Threshold resummation for squark-antisquark  
 2030 and gluino-pair production at the LHC”. In: *Phys. Rev. Lett.* 102 (2009),  
 2031 p. 111802. doi: [10.1103/PhysRevLett.102.111802](https://doi.org/10.1103/PhysRevLett.102.111802). arXiv: [0807.2405](https://arxiv.org/abs/0807.2405) [[hep-ph](#)].

- 2033 [63] A. Kulesza and L. Motyka. “Soft gluon resummation for the production  
 2034 of gluino-gluino and squark-antisquark pairs at the LHC”. In: *Phys. Rev.*  
 2035 *D* 80 (2009), p. 095004. doi: [10.1103/PhysRevD.80.095004](https://doi.org/10.1103/PhysRevD.80.095004). arXiv:  
 2036 [0905.4749 \[hep-ph\]](https://arxiv.org/abs/0905.4749).
- 2037 [64] Wim Beenakker, Silja Brensing, Michael Kramer, Anna Kulesza, Eric Lae-  
 2038 nen, et al. “Soft-gluon resummation for squark and gluino hadroproduc-  
 2039 tion”. In: *JHEP* 0912 (2009), p. 041. doi: [10.1088/1126-6708/2009/12/041](https://doi.org/10.1088/1126-6708/2009/12/041). arXiv: [0909.4418 \[hep-ph\]](https://arxiv.org/abs/0909.4418).
- 2041 [65] W. Beenakker, S. Brensing, M.n Kramer, A. Kulesza, E. Laenen, et al. “Squark  
 2042 and Gluino Hadroproduction”. In: *Int. J. Mod. Phys. A* 26 (2011), p. 2637.  
 2043 doi: [10.1142/S0217751X11053560](https://doi.org/10.1142/S0217751X11053560). arXiv: [1105.1110 \[hep-ph\]](https://arxiv.org/abs/1105.1110).
- 2044 [66] Michael Krämer et al. *Supersymmetry production cross sections in pp collisions*  
 2045 at  $\sqrt{s} = 7 \text{ TeV}$ . 2012. arXiv: [1206.2892 \[hep-ph\]](https://arxiv.org/abs/1206.2892).
- 2046 [67] Rasmus Mackeprang and Andrea Rizzi. “Interactions of Coloured Heavy  
 2047 Stable Particles in Matter”. In: *Eur. Phys. J. C*50 (2007), pp. 353–362. doi:  
 2048 [10.1140/epjc/s10052-007-0252-4](https://doi.org/10.1140/epjc/s10052-007-0252-4). arXiv: [hep-ph/0612161](https://arxiv.org/abs/hep-ph/0612161)  
 2049 [hep-ph].
- 2050 [68] Rasmus Mackeprang and David Milstead. “An Updated Description of  
 2051 Heavy-Hadron Interactions in GEANT-4”. In: *Eur. Phys. J. C*66 (2010), pp. 493–  
 2052 501. doi: [10.1140/epjc/s10052-010-1262-1](https://doi.org/10.1140/epjc/s10052-010-1262-1). arXiv: [0908.1868](https://arxiv.org/abs/0908.1868)  
 2053 [hep-ph].
- 2054 [69] J. Alwall, R. Frederix, S. Frixione, V. Hirschi, F. Maltoni, O. Mattelaer, H. S.  
 2055 Shao, T. Stelzer, P. Torrielli, and M. Zaro. “The automated computation of  
 2056 tree-level and next-to-leading order differential cross sections, and their  
 2057 matching to parton shower simulations”. In: *JHEP* 07 (2014), p. 079. doi:  
 2058 [10.1007/JHEP07\(2014\)079](https://doi.org/10.1007/JHEP07(2014)079). arXiv: [1405.0301 \[hep-ph\]](https://arxiv.org/abs/1405.0301).
- 2059 [70] “dE/dx measurement in the ATLAS Pixel Detector and its use for particle  
 2060 identification”. In: (2011).
- 2061 [71] ATLAS Collaboration. “The ATLAS Simulation Infrastructure”. In: *Eur.*  
 2062 *Phys. J. C*70 (2010), pp. 823–874. doi: [10.1140/epjc/s10052-010-1429-9](https://doi.org/10.1140/epjc/s10052-010-1429-9). arXiv: [1005.4568 \[physics.ins-det\]](https://arxiv.org/abs/1005.4568).

2064 DECLARATION

---

2065 Put your declaration here.

2066 *Berkeley, CA, September 2016*

2067

---

Bradley Axen



2068

2069 COLOPHON

2070

Not sure that this is necessary.